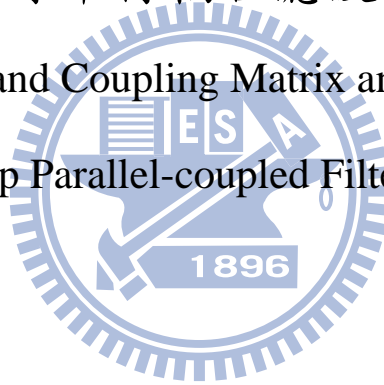# 國 立 交 通 大 學

電信工程研究所

博 士 論 文

多頻濾波器耦合矩陣之合成及其

實現於微帶線平行耦合濾波器結構之研究

Synthesis of Multi-band Coupling Matrix and Its Implementation of

Microstrip Parallel-coupled Filter Structures

研 究 生：郭益廷　　　(Yi-Ting Kuo)

指導教授：張志揚　教授 (Chi-Yang Chang)

中 華 民 國 一 百 年 十 月

多頻濾波器耦合矩陣之合成及其實現於微帶線平行耦合濾波器

結構之研究

Synthesis of Multi-band Coupling Matrix and Its Implementation of

Microstrip Parallel Coupled Filter Structures

研 究 生：郭益廷　　　　　Student：Yi-Ting Kuo

指導教授：張志揚　　　　　Advisor：Chi-Yang Chang

國 立 交 通 大 學

電信工程研究所

博 士 論 文

A Dissertation Submitted to

Department of Communication Engineering

College of Electrical Engineering and Computer Engineering

National Chiao Tung University

In partial Fulfillment of the Requirements

For the Degree of Doctor of Philosophy

in

Communication Engineering

October 2011

Hsinchu, Taiwan, Republic of China

中 華 民 國 一 百 年 十 月

多頻濾波器耦合矩陣之合成及其實現於微帶線平行耦合濾波器結構之研究

研究生: 郭益廷　　　　　　　　　　　指導教授: 張志揚 博士

國立交通大學電信工程研究所

摘　　　要

　　本論文研究主題為一個完整設計雙頻與多頻濾波器的流程，並實現於微帶線平行耦合濾波器架構上。首先提出一種新的全解析式的多頻濾波器耦合矩陣合成技術，透過簡單的操作，將廣為人知的單頻濾波器耦合矩陣合成技術推廣至多頻應用。此提出的技術可以保證其產生之響應遵守廣義柴比雪夫特性，亦即在多頻濾波器各通帶保持等漣波特性。接著，將此合成技術所生成之耦合矩陣轉換到可實現的耦合架構上。本文提出單路徑式與雙路徑式耦合架構，並且對於其在雙頻濾波器應用上進行比較與分析。透過對應其耦合矩陣之耦合係數與平行耦合濾波器的設計參數，可以分別設計出每個路徑所對應的平行耦合濾波器。對於雙路徑式架構，需要兩個同向雙工器將兩路徑連接以完成雙頻濾波器設計。接著，為了進一步縮小雙頻濾波器的面積，本文使用山型雙模諧振腔的雙模特性來設計縮小化的雙頻濾波器。透過山型諧振腔的奇、偶模分析可以找出其適當的濾波器耦合架構即為雙路徑式耦合架構，並且可以透過分析將耦合矩陣對應至濾波器設計參數上。此對應方法為一全解析式的流程，可以提供設計者有效率的雙模雙頻濾波器設計。同樣的，在三頻與四頻濾波器設計中，三路徑式與四路徑式的架構可以用來設計其所需要的耦合矩陣。接著透過將兩相鄰頻帶當作一個群組，變成雙頻濾波器加單頻濾波器(針對三頻濾波器)或者雙頻濾波器加雙頻濾波器(針對四頻濾波器)的群組。其中雙頻濾波器或單頻濾波器均可由其耦合矩陣對應之耦合係數和山形諧振腔的設計參數進行合成。最後再將所產生的兩個濾波器透過兩個同向雙工器相接，形成所需要的三頻或四頻濾波器。

Synthesis of Multi-band Coupling Matrix and Its Implementation of Microstrip Parallel-coupled Filter Structures

Student: Yi-Ting Kuo   **Advisor: Dr. Chi-Yang Chang**

Institute of Communication Engineering

National Chiao Tung University

Abstract

The research topic in this dissertation is a complete design flow for dual-band and multi-band filter synthesis, and these synthesized filters are implemented using microstrip parallel-coupled lines structures. First of all, a novel fully analytical multi-band coupling matrix synthesis technique is provided. By simple operations, the well-known single-band coupling matrix synthesis technique is then extended for the multi-band filter design. The proposed technique guarantees the original single-band equal-ripple property within each passbands following each single-band generalized Chebyshev characteristic. Furthermore, the requested coupling matrix should be transferred into the realistic coupling schemes for the practical implementation. In this dissertation, single-path and dual-path coupling schemes are provided, and the properties of each coupling scheme will be discussed. Moreover, the design parameters of the parallel-coupled filter are related with the components of the coupling matrix, the practical parallel-coupled filter for each path will be synthesized. For the dual-path topology, the synthesized dual-band filter needs double-diplexing configuration to connect two filters of two paths. In order to further reduce the size of dual-band filters, the E-shaped resonator is proposed for its two-mode property and is useful for the

development of miniaturized dual-band filters. By even- and odd-mode analysis of the E-shaped resonator, the dual-path coupling scheme is chosen for the dual-band filter design, and the practical design parameters of the dual-band filter will be extracted based on the corresponding coupling matrix. And such synthesis procedure is fully analytical and it provides an efficient design flow for the designer. Similarly, for the tri-band and quad-band filter design, the tri-path and quad-path coupling schemes are used for the coupling matrix synthesis. After grouping two adjacent passbands, the tri-band response will be separated into one dual-band response and one single-band response; and the quad-band response will be separated into two dual-band responses. In each grouped dual-band and single-band response, the corresponding E-shaped filter can be synthesized based on the corresponding coupling matrices. Finally, the double-diplexing configuration is used to connect two filters and then the tri-band or quad-band filter synthesis will be completed.
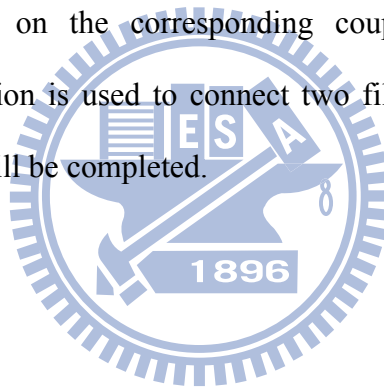
誌 謝

首先我要感謝我的指導教授張志揚博士，若不是張教授願意收留我並且給予我很多學術上的協助與生活上的言教與身教，這個學位我不會有機會拿到。此外，我要特別感謝來參與我口試並且給我意見使本論文更加完美的口試委員，分別是郭仁財教授、鍾世忠教授、黃瑞彬教授、紀佩綾教授、王暉教授、邱煥凱教授、林祐生教授、湯敬文教授。謝謝老師們給與寶貴的意見、指教以及鼓勵。在這裡再一次的表達我對老師們的感謝。

對於博士生來說，博士學位象徵著是一種研究方法學習的認可，而更多的，是一種對於學術、對於人與人之間的關係和對於未來人生規劃上的一種磨練與學習。在這一路上，有很多的不確定感和挫折，從想放棄到最後終於到達目的地，實在是有太多的人需要感謝了。首先我要感謝趙學永博士，趙博士是我在交通大學的第一任指導教授，從我碩一開始，不斷的鼓勵我也教導我很多做學問的堅持以及方向。趙博士從不嫌煩的總是對我有問必答，也刺激我在思考學術問題上面有更嚴謹的態度。此外，若是說我後來做研究有足夠的程式背景做為開發工具，一定是來自於趙博士對我在程式上的訓練以及教誨。然而趙博士在我求學過程中往國外業界發展，而我當時不夠成熟，所以婉拒了趙博士繼續指導的美意。若說我在博士生涯有何遺憾，此必定為最。

再經歷過另一位教授的指導，但因在學術理念上的不合以及心態上的不適應，我選擇中途休息。感謝電信所的陳伯寧教授以及鍾世忠教授在擔任電信所所長期間對於我的更換指導教授的事情上面多所幫忙，也感謝趙學永博士不計前嫌的書信往返的協助，讓我能順利的更換到張志揚教授的研究群。而我更要感謝張志揚教授的提攜與其在學術上的引導，張教授開朗而自由的風格以及在研究上的正直與堅持，讓我重新對於人生有不同的體悟以及看法。張教授的言行合一的態度以及他對生活的喜愛和對學術的熱誠，讓我受益良多，而能在這樣充滿愛以及信任的研究室裡做研究，也才真的能夠有時間思考新的創意以及有新的想法。

鵬達、義傑、梓淳還有老是被我欺負的學妹們宛蓉、懿萱、士鈺和祥蓉，有你們在真的是讓實驗室生色不少。尤其是宛蓉，真是辛苦妳在我的帶領下做了很多辛苦事和腦包事。至於新進來的大學姐弘偉、皓宇、若宜、郁叡，實驗室的美好正等著妳們探索。

這裡也要特別感謝 Camy，最後這一段時間謝謝妳不時的鼓勵與分享，讓我能專心也安心的在研究上面努力。

最後，我最要感謝得是我的家人，我也想將這篇論文獻給，我的父親郭榮樹、我的母親翁毓嬪，謝謝你們的辛苦栽培，讓我在博士的生涯上無後顧之憂，也謝謝哥哥郭奕良、郭奕成，能成全我到三十歲還能繼續求學。我也要趁這個機會感謝從小照顧我長大的奶奶郭黃水河、爺爺郭蟬，以及在小學到大學時期不時關心我生活的外公翁耀清，外婆翁楊岡市，沒有你們的愛與關懷，不會有現在的我。

郭益廷 於新竹交大

2011 年 11 月 14 號

Contents

List of Tables

List of Figures

Chapter 1

Introduction

Microwave filter is an essential component in the wireless communication system. In single-band filter design, the mechanisms in bandwidth variation, transmission zero generation and adjustment, and the return loss determination, have been widely discussed and studied.

As the wireless communication systems grow, the standards of each communication system have been provided. The requirements of dual-band and multi-band applications become popular. Connecting two single-band filters is a simple way to generate the dual-band characteristic. The main drawback, however, is the huge size of such dual-band filter. To overcome the problem, SIR filter is proposed for its behavior of adjusting the resonance of the 2nd harmonic, and the property is then used to design the dual-band and tri-band filters. It is very useful for those filters with two wide-separated passbands. For the filters with closely-adjacent passbands, a two-mode resonator becomes a good candidate for its small size. There are many researcher give design curves and analytical analysis for proposed configuration. In this dissertation, the analytical approach for determining the design parameters of dual-band filters based on the coupling matrix is proposed. Moreover, for the two-mode dual-band filter design, we propose a fully analytical synthesis procedure based on the corresponding coupling matrix.

1.1 Research Motivation

Microwave dual-band and multi-band systems, such as GPS, GSM and WIMAX, are

very popular and there are many applications in microwave components and systems. For the aspect of the filter design, many researchers have proposed design procedures and proper configuration. And many analytical approaches and design curves have been provided.

In order to capture the filter characteristic precisely based on the filter specifications, coupling matrix synthesis technique provides useful information in coupling coefficient determination between resonators. Moreover, the coupling matrix shows its advantage in hardware implementation. Extending the ability of coupling matrix into dual-band and multi-band applications, there are no analytical synthesis methods.

To relate the design parameters for the dual-band and multi-band filter design with the corresponding coupling coefficients, the coupling matrix should be established firstly. Hence the first step in this dissertation is to develop the dual-band and multi-band coupling matrix synthesis technique. Once the corresponding coupling coefficients between resonators are determined, the next step is to find the relationship to extract the design parameters analytically.

In this dissertation, the application is based on the microstrip implementation. The relationship between coupling coefficients and design parameters, hence, are based on parallel-coupled line configuration. In this step, the parameters of the parallel-coupled line configuration can be extracted analytically.

For the aspect of the application, the dual-band and multi-band filters with closely adjacent passbands are used. For the communication standards, the closely adjacent passbands are necessary. For example, the receiver for GPS has to decode the signal at two frequencies, and they are L1 (1575.42 MHz) and L2 (1227.60 MHz). Here a dual-band filter is necessary in such kind of receiver to filter the signal within two closely adjacent passbands.

In this dissertation, the whole design flow is developed. The dual-band and

multi-band coupling matrix synthesis technique has been developed. Moreover the filter with parallel-coupled line has been synthesized. The two-mode E-shaped resonator then is analyzed and provided for the size reduction. Finally, tri-band and quad-band filter are realized by the proposed semi-analytical design procedure.

1.2 Literature Survey

For the recent developments in dual-band filter design, there are three major techniques. The first one is to connect two individual filters with common input/output feeding networks. However, this technique will face the large size and large insertion loss due to the usage of the large number of resonators. Moreover, directly connection of two single-band filter will degrade the filter response and rough tuning is required. The second technology is to cascade a wideband filter with a bandstop filter. Such kind of dual-band filters has very narrow separation between two adjacent passbands, and it also occupies large area of the wireless communication system. The third technology is to use the multi-mode resonators to design the dual-band filters. Due to the multi-mode property, the small size and low insertion loss can be achieved. Stepped-impedance resonator (SIR), stub-loaded resonator, and those resonators with degenerate modes belong to the third category. For this category, the drawbacks of the dual-band filters composites with the dual-mode resonators are individually controlling of each passband and introducing finite transmission zeros. To overcome these problems, many researcher keeps in studying and providing novel schematics. Here a brief survey of recent three years (2009-2011) is introduced.

To obtain both dual-band characteristic and the size reduction, many novel dual-band schematics are proposed. Dual-mode ring resonators [1]-[2], stub-loaded resonators [3]-[9], SIR [10]-[22], signal-interference structures [23]-[25] and composite right\left handed (CRLH) resonators [26]-[29] are used to develop the dual-band filter based on their

3

intrinsic dual-band characteristics. Within these designs, to separately control each passband, stub-loaded can used to change response of one passband and keep the response within another passband unchanged [3]-[9]. To obtain the miniaturized dual-band filters, SIR is the suitable candidate in those dual-mode resonators. But the intrinsic SIR has the limitation in controllability in each passband and lacks an efficient way to introducing the finite transmission zeros. In [10]-[13], [18], [22], they provide efficient way to control the passband separately. To introduce the finite transmission zeros, source-load coupling is used in [10], [16], [18]. Moreover, for the wide-bandwidth application, the modifications have been developed in [17], [19]. And the further size reduction techniques have been be extended in [16], [17]. The techniques in [23]-[25] provide the transversal topology to create the dual-band characteristic. And the closed form is provided in [24]. CRLH in [26]-[29] are provide to those applications which require both the highly suppressed response of higher harmonic and the miniaturize size.

Besides, many novel configuration for dual-band filters are proposed [30]-[51]. In these designs, quarter-wavelength resonators [31], [39] are proposed for size reduction. and some analytical analysis [42], [49], [50] are applied to some interesting configurations. Resonators with slot are used to separate two degenerate modes [30], [37], and high Q resonators are considered for the low insertion loss in filter designs [36], [46]. For some specific responses, the suitable coupling schemes are considered [31], [35], [40], [41], [43], [44], [45], [51].

Some dual-band filters need specific purpose, such as controllable dual-band characteristic [29], [52]-[58], balun filter [59], balanced filter [60]-[65], ultra-wideband (UWB) application [7], [66]-[68], and low insertion loss (i.e., high Q) applications [69]-[72]. Pin diodes [52], [53] or varactor-diode capacitors [54], [57], [58] are used to control if the filter operates at single-band or dual-band operation. Moreover, the bias voltage can be used to achieve the wide stopband [57]. For balanced filter, the common

mode suppression is a major problem and is eliminated using the proposed techniques in [62]-[65]. To cover a wide-passband bandwidth, the techniques in [7], [66]-[68] have provided some solutions. For the low insertion loss applications, substrate integrated waveguide (SIW) resonator has a high quality factor [69]-[72]. To design such kind of dual-band filter efficiently, the analytical synthesis is provide [71] and the corresponding coupling matrix is used in helping the design [72].

In order to further reduce the circuit size, the multi-layer structure using low-temperature co-fired ceramic substrate (LTCC) [7], [29],[66], [72]-[76] and single ring structure are proposed [77]-[81].

To relate the requested dual-band characteristic to the real-world design, coupling matrix has the advantage in the hardware implementation. The real-world designs based on corresponding coupling matrix are more easily to be developed under the specific coupling configuration [82]-[89]. Moreover, due to the exact synthesis for the transversal coupling matrix based on the specifications, the transversal topology has been studied in the real-world dual-band filter design [87], [89].

After the brief review, the most efficient way to design the dual-band filter is to obtain the corresponding coupling matrix first, and then relate the coupling coefficient with the practical design parameters under the required coupling scheme. Hence the efficient dual-band coupling matrix synthesis is required. Recent developments in coupling matrix synthesis for single-band filter design are very attractive. Analytical methods for the single-band filter synthesis [90]-[93] are proposed to generate a transversal coupling matrix. For other specific coupling schemes, the coupling matrices are obtained using matrix rotation or optimization [94], [95]. To design dual-band or multi-band filters, many methods were proposed. Frequency transformation [96]-[98] was proposed to generate the response function analytically for dual-band filters. It was developed with governing equations of single-band filters. It was unrealizable, however, for multi-band filters.

Another method was based on parallel-coupled line model [99]; this was used to generate the dual-band performances. This method was limited for dual-band filters, though, and could not be used for multiband filters.

To obtain the multi-band performance, an equivalent lumped-element network [100]-[102] was introduced. This network simplified the design procedure for dual-band or multi-band filters via the iterative procedure. The problems, however, such as the need for optimization for roots finding [100], [102] or inability to achieve equal-ripple [101], [102], occurred while applying those equivalent networks.

In filter design, the coupling matrix technique is well-known with the advantage of the hardware implementation. To take advantage of coupling matrices for dual-band or multi-band filters, optimization methods [103], [104] were proposed to generate the coupling matrix numerically, via proper cost functions. Fully analytical coupling matrix synthesis for dual-band or multi-band filters, however, has not been proposed yet. In this dissertation, the novel multi-band coupling matrix synthesis will be proposed in Chapter 2.

For the aspect of the dual-band filter design, the corresponding polynomials of the reflection and transfer functions are firstly modified into the dual-band characteristics, and the dual-band coupling matrix is then synthesized based on those modified polynomials [97], [105]. Considering the implementation of the dual-band filter, some coupling schemes, for examples, cul-de-sac [98], inline topology [97], and extended box topology [100], are generated via a series of similarity transformations [98], [106]. Some of those topologies, however, are difficult to be realized in microstrip circuit form. Considering the dual-band microstrip filter, dual-mode [107] and frequency-separated coupling scheme [108] are proposed to realize the dual-band characteristics. The phenomenon in placing transmission zeros related to corresponding coupling topologies, however, is not clear yet such that the mechanism in transmission zeros generation of the dual-band filter is still unobservable under proper coupling schemes. In the Chapter 3 of this dissertation, the

dual-path coupling scheme will be discussed for its ability in microstrip implementation.

For the purpose of size reduction, the two-mode dual-band filters have been an attractive solution for dual-band applications. Moreover, two-mode resonators also have the advantage of intrinsic dual-band characteristic and separated design parameters of each passband [109]-[121]. To develop a two-mode dual-band resonator, different approaches are provided. A resonator with perturbations is widely used to excite the two-mode property of the resonator, and the dual-band filter is designed by carefully combining two such two-mode resonators. For examples, a waveguide filter [109] and dual-band filters using ring resonators [110]-[114] are constructed by two resonators operated at two frequencies. To achieve specifications of each passband, the perturbations are added and tuned. An alternative two-mode resonator is the stub-loaded open-loop resonator [115]-[117]. The stub is used to excite another mode of the resonator. Recently, two-mode dual-band filters constructed by a single resonator are provided for further size reduction [77], [118]-[121]. These two-mode dual-band filters have small size, and they have tuning stubs or patches for tuning performances of each passband and transmission zeros. However, there is still lack of analytical approach in two-mode dual-band filter design yet.

E-shaped resonator is validated in two-mode single-band filter design [122]-[124] and it is a good candidate in dual-band filter design [125]. The even- and odd-mode analysis of the E-shaped resonator is proposed in [122] and corresponding coupling scheme is proposed in [124]. The analytical approach for two-mode dual-band filter synthesis using E-shaped resonators is proposed in Chapter 4 for the closely adjacent passbands.

For the aspect of tri-band and quad-band filter design, the compact size is still a key issue in microwave application. Lots of dual-mode resonators have been proposed for multi-band filter design [126]-[131]. Those filter designs, however, have no analytical procedure and the designer needs more efforts to obtain the multi-band performance. In this dissertation, the semi-analytical procedure is proposed in Chapter 5.

1.3 Contribution

In this dissertation, we propose a novel fully analytical method for the synthesis of multi-band transversal coupling matrix. The response function of the multi-band filter is generated via the proper combination of single-band filtering functions, which can be obtained using the technique in [90]. Based on our proposed method, the fully analytical fractional expressions for two-port scattering parameters are generated. Moreover, under proper combination the prescribed transmission zeros are available in multi-band filters, while the different bandwidth of each passband is also allowed. Once the fractional forms for the scattering parameters of the dual-band or multi-band filtering function are obtained, they are converted into the transversal coupling matrix using the method in [92]. Then, using the technique in [94], the transversal coupling matrix can be transferred into a requested coupling scheme.

Considering the practical implementation of the response of each passband, the dual-path coupling scheme is proposed for its property in illustrating the dual-band characteristics via the frequency-separated paths. The mechanism of transmission zeros and the separation between two adjacent passbands can be studied by coupling matrix.

For compact size in dual-band filter design with closely adjacent passbands, the analytical approach for two-mode dual-band filter synthesis using E-shaped resonators is proposed. Based on the proposed dual-band coupling matrix synthesis, the odd-mode of the E-shaped resonator is firstly analyzed to determine the dimensions corresponding to match the odd-mode filter parameters. Then the central open-stub of the E-shaped resonator can be used to adjust the slop parameter of the even-mode to satisfy the requirements of the even-mode filter. In addition, the out-of-phase property of two edges of an E-shaped

resonator is also discussed and used to improve the separation of two adjacent passbands. By properly arranging the filter layout, the filter order can be increased and the requested transmission zeros are available.

For the tri-band and quad-band filter design, a semi-analytical procedure is proposed. Based on the specific coupling matrix, the corresponding design parameters are then extracted analytically. Moreover, by grouping two adjacent passbands, the tri-band and quad-band performances are then divided into two groups in each design. In each group, the filter with dual-band performance can be synthesized analytically using E-shaped resonator. Finally, to combine these two synthesized filters, double-diplexing configuration [132] is used with some fine tunes, and then the tri-band and quad-band filter can be obtained.

In this dissertation, the circuit simulation is completed using ADS [133] and the full-wave simulator SONNET [134] provides reliable simulations for all proposed filters.
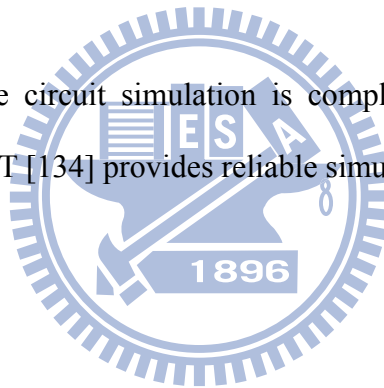
1.4 Organization

This dissertation is organized as follows. Chapter 1 describes the relative researches and difficulty in the microwave dual-band and multi-band filter design. In Chapter 2, the proposed analytical coupling matrix synthesis is described in detail. The different order, different return loss, arbitrary transmission zeros, and multi-band characteristic are available in this synthesis technique. Moreover, the behavior of generating the intrinsic isolation between two adjacent passbands is also discussed. The synthesized polynomials and coupling matrices are listed to give the reader more information in checking the proposed technique.

Chapter 3 describes the single-path and dual-path topologies for the dual-band filter

design. The frequency-separation property can be observed in the dual-path topology, and it is useful in frequency planning and filter implementation. Moreover, the mechanism of introducing transmission zeros is similar to that in the single-band filter design, and it is also discussed the in dual-band filter design. The dual-band filter with parallel-coupled lines is then synthesized based on the user-specific coupling matrix in order to extract the filter in each path. After connecting those two filters using double-diplexing configuration, the dual-band filter with dual-path configuration is then generated.

In Chapter 4, the analytical synthesis procedure in designing two-mode dual-band filter is proposed. E-shaped resonator is used to analyze for its even- and odd-mode properties. The two-mode dual-band filter with E-shaped resonators is then synthesized analytically based on the user-specific coupling matrix with dual-path coupling scheme. The guide line in using the back-to-back E-shaped topology is also provided for the pre-defined coupling coefficient. Chapter 5 describes the tri-band and quad-band filter design using the E-shaped resonator proposed in Chapter 4. The tri-path and quad-path topologies are used to generate the corresponding coupling matrix. To generate the tri-band and quad-band filter, the two dual-band filters are connected using double-diplexing configuration.

In Chapter 6, we conclude the dissertation and draw suggestions for future works.

Chapter 2

Fully-Analytical Multi-band Coupling Matrix Synthesis

2.1 Introduction

In this chapter, the procedure of multi-band coupling matrix synthesis is discussed in detail. For single-band filter design, the coupling matrix synthesis is proposed in [90], and it has the advantage in hardware implementation. For the multi-band filter design, the most popular procedure is the analytical iterative method [102]. The iterative method, however, may not only have the convergence problem under specific requirement, but also generate some unwanted performances in multi-band filter design. The phenomenon will also be discussed latter.
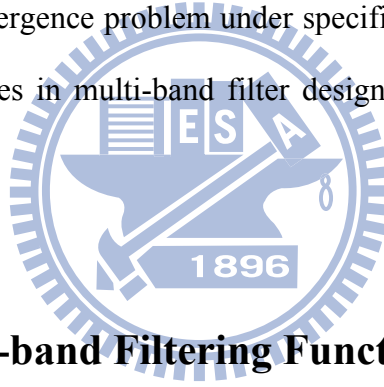
2.2 Analytical Multi-band Filtering Function Synthesis
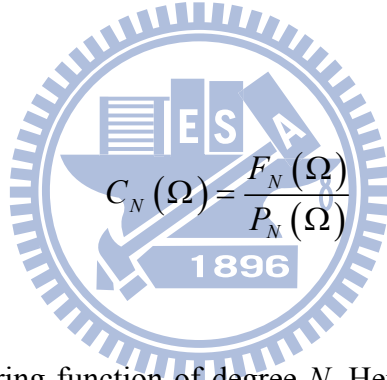
To develop a novel and fully analytical multi-band coupling matrix synthesis technique, here a modification is applied to the well-known single-band coupling matrix synthesis and generalized this procedure into the multi-band filter design. The single-band coupling matrix synthesis procedure is shown in Figure 2-1 and is described briefly in the following. For a two-port lossless filter network with N inter-coupled resonators, the transfer and reflection function can be expressed as a ratio of two N-th degree polynomials

$$S_{11}(\Omega) = \frac{F_N(\Omega)}{E_N(\Omega)}, \quad S_{21}(\Omega) = \frac{P_N(\Omega)}{\varepsilon E_N(\Omega)} \qquad \text{(2-1)}$$

where Ω is the real frequency variable, the related complex frequency variable $s = j\Omega$, and ε is a normalization constant related to the prescribed return loss level; all polynomials have been normalized so that their highest degree coefficients are unity. $S_{11}(\Omega)$ and $S_{21}(\Omega)$ have a common denominator $E_N(\Omega)$, and the transmission zeros of the transfer function are contained in the polynomial $P_N(\Omega)$. Using (2-1) and the energy conservation for a lossless network, $S_{11}(\Omega)^2 + S_{21}(\Omega)^2 = 1$, $S_{21}(\Omega)$ can be represented as

$$S_{21}\left(\Omega\right)^{2} = \frac{1}{1+\varepsilon^{2}C_{N}^{2}\left(\Omega\right)} \tag{2-2}$$

where

$$C_{N}\left(\Omega\right) = \frac{F_{N}\left(\Omega\right)}{P_{N}\left(\Omega\right)} \tag{2-3}$$

$C_N(\Omega)$ is known as the filtering function of degree N. Here, the proposed filters have the form of the generalized Chebyshev characteristic.

In the procedure in Figure 2-1, the filtering function $C_N(\Omega)$ governs the filter performance. To extend the single-band performance to multi-band one, the property of filtering function is described first. The filtering function satisfies the following conditions:

$$C_{N}\left(\Omega\right)\begin{cases} =1, & |\Omega|=1 \\ <1, & |\Omega|<1 \\ >1, & |\Omega|>1 \end{cases} \tag{2-4}$$

Here a 3rd order filtering function is used as an example. Figure 2-2 shows the

performance of the filtering function with and without a pair of transmission zeros. It can be noted that the magnitude of the filtering function is less than 1 within the passband. The magnitude of the filtering function increases, as the normalized frequency moves away from the passband. Furthermore, if the transmission zeros appear, the magnitude of filtering function grows dramatically.

INPUT: (1) Filter order(2) Return loss
(3) Prescribed transmission zeros

From the recursive technique，the fractional forms of S_{11} and S_{21} are:

$S_{11}(\Omega) = F(\Omega)/E(\Omega)$, $S_{21}(\Omega) = P(\Omega)/(\varepsilon E(\Omega))$,

The filtering function is defined as

$C_N(\Omega) = F(\Omega)/ P(\Omega)$

Transfer S-parameters into Y-parameters

$S_{11}(\Omega) = F(\Omega)/E(\Omega)$, $S_{21}(\Omega) = P(\Omega)/(\varepsilon E(\Omega))$,

$Y_{11}(\Omega) = m(\Omega)/n(\Omega)$, $Y_{21}(\Omega) = P(\Omega)/ n(\Omega)$,

Y-parameters derived from the transversal coupling matrix are $Y_{11}{}^M$ and $Y_{21}{}^M$. Let

$Y_{11} = Y_{11}{}^M$，$Y_{21} = Y_{21}{}^M$

OUTPUT
Single-Band Transversal Coupling Matrix

Figure 2-1. The procedure of the single-band coupling matrix synthesis [90].
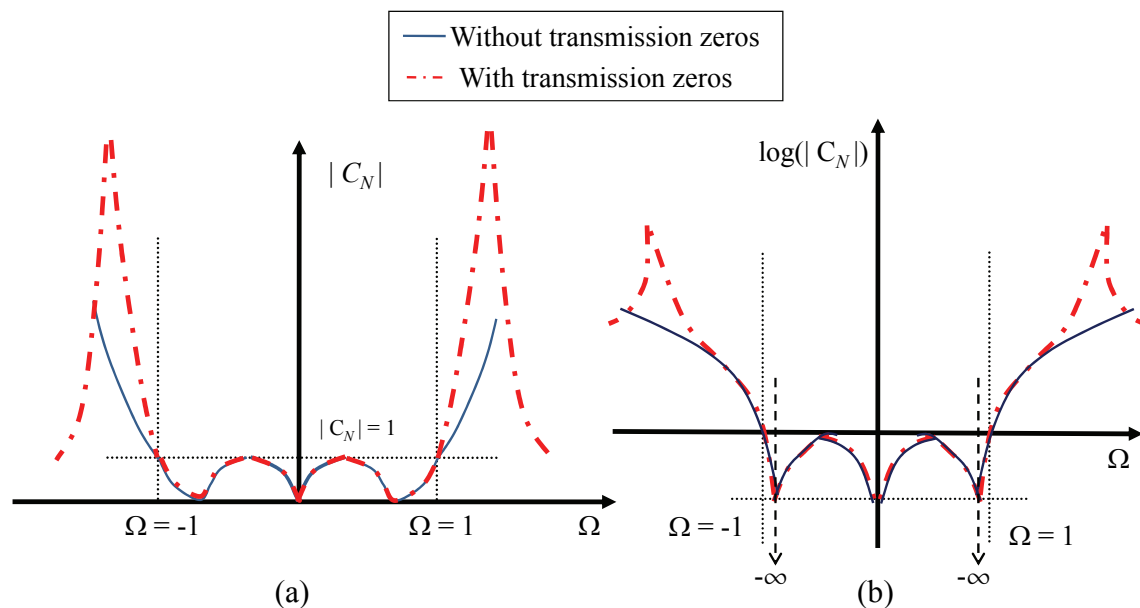
Figure 2-2. The response of the 3rd order filtering function. (a) The linear scale. (b) The log scale.

To combine two filtering functions into a composite filtering function and the resulting composite filtering function has to satisfy (2-4), the parallel addition of two filtering functions is applied. The parallel addition of two filtering functions is defined as the reciprocal of the composite filtering function equals to the sum of the reciprocal of two filtering functions just like the total resistance of two parallel connected resistors. After the operation, the filtering function with small value dominants the performance of the composite filtering function. For the filtering function, it has small values within the passband, and very large values while $|\Omega| > 1$, which follows the property of Chebyshev characteristic. Based on above property, while applying parallel addition of two filtering functions with different central frequencies, the dual-band filtering function can be obtained. In Figure 2-3, the solid line represents a dual-band filtering function, which comes from summing up the reciprocal of two 2nd order filtering functions with different central frequencies. In this figure, it is clear to show that the small value of two filtering functions will dominate the value of the composite filtering function. Hence the operation

of summing up the reciprocal of each filtering function is useful in the dual-band filtering

function synthesis.
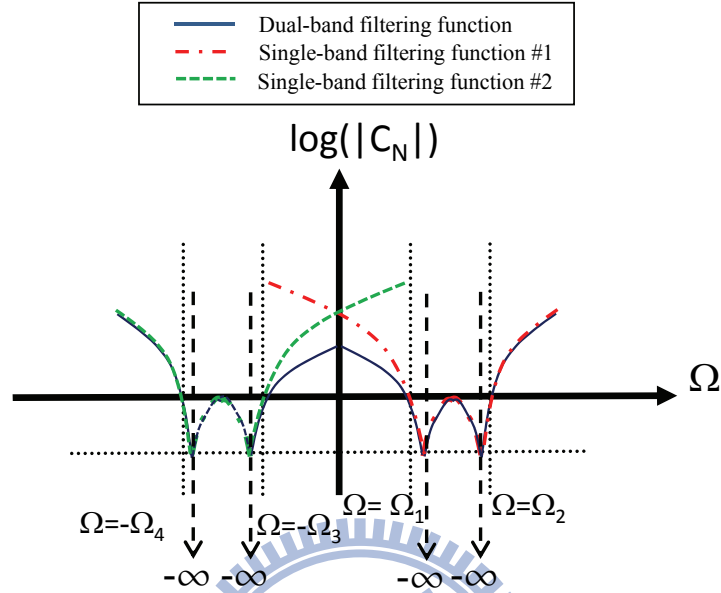
Figure 2-3. The performance of the 4th order dual-band filtering function.
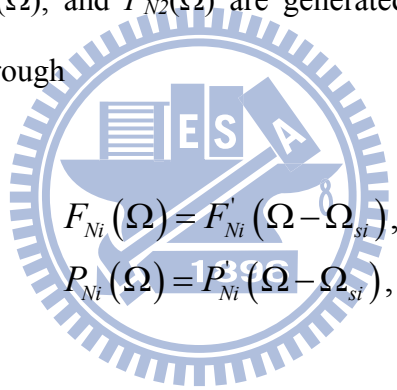
Based on above description, the composite filtering function can be obtained as

follows:

$$\varepsilon C_N\left(\Omega\right) = \cfrac{1}{\cfrac{1}{\varepsilon_1 C_{N1}\left(\Omega\right)} + \cfrac{1}{\varepsilon_2 C_{N2}\left(\Omega\right)}} = \frac{\varepsilon_1 \varepsilon_2 C_{N1}\left(\Omega\right) C_{N2}\left(\Omega\right)}{\varepsilon_1 C_{N1}\left(\Omega\right) + \varepsilon_2 C_{N2}\left(\Omega\right)}, \qquad (2\text{-}5)$$

where $C_{N1}(\Omega)$ and $C_{N2}(\Omega)$ are single-band filtering functions with shifted central

frequencies. The principal advantage of this technique is that the individual filtering

function $C_{N1}(\Omega)$ and $C_{N2}(\Omega)$ can be obtained analytically by the efficient recursive

technique and frequency shift. Hence the polynomial of the composite filtering function

can be derived as

15

$$
\begin{aligned}
\varepsilon C_N(\Omega) &= \cfrac{1}{\cfrac{1}{\varepsilon_1 C_{N1}(\Omega)} + \cfrac{1}{\varepsilon_2 C_{N2}(\Omega)}} \\[2ex]
&= \cfrac{1}{\cfrac{P_{N1}(\Omega)}{\varepsilon_1 F_{N1}(\Omega)} + \cfrac{P_{N2}(\Omega)}{\varepsilon_2 F_{N2}(\Omega)}} \\[2ex]
&= \varepsilon_1 \varepsilon_2 \cfrac{F_{N1}(\Omega) F_{N2}(\Omega)}{\varepsilon_2 P_{N1}(\Omega) F_{N2}(\Omega) + \varepsilon_1 P_{N2}(\Omega) F_{N1}(\Omega)} \\[2ex]
&= \varepsilon \frac{F_N(\Omega)}{P_N(\Omega)},
\end{aligned}
\tag{2-6}
$$

where $F_{N1}(\Omega)$, $F_{N2}(\Omega)$, $P_{N1}(\Omega)$, and $P_{N2}(\Omega)$ are generated by frequency shifting of the original filtering function through

$$
\begin{aligned}
F_{Ni}(\Omega) &= F'_{Ni}(\Omega - \Omega_{si}), \\
P_{Ni}(\Omega) &= P'_{Ni}(\Omega - \Omega_{si}),
\end{aligned}
\tag{2-7}
$$

where $i = 1$ and 2, ω_{si} is the central frequency for the i-th passband, and $F'_{Ni}(\Omega)$ and $P'_{Ni}(\Omega)$ are all generated by recursive technology analytically [93]. In addition, the transmission zeros can be generated using those $C_{N1}(\Omega)$ and $C_{N2}(\Omega)$ corresponding to their central frequency at each passband via (2-6).

In case of two passband with different bandwidth, these polynomials should be modified. For the i-th filtering function with frequency shift Ω_{si} and the multi-band lowpass domain bandwidth δ_i, the polynomial can be represented as

$$F_{Ni}(\Omega) = \prod_{j=1}^{NF_i} \left(\frac{2}{\delta_i} \cdot (\Omega - \Omega_{si}) - f_{i,j} \right),$$

$$P_{Ni}(\Omega) = \prod_{j=1}^{NF_i} \left(\frac{2}{\delta_i} \cdot (\Omega - \Omega_{si}) - p_{i,j} \right), \qquad (2\text{-}8)$$

where $i = 1$ and 2, and $P_{Ni}(\Omega)$ is the denominator and $F_{Ni}(\Omega)$ is the numerator of $C_{Ni}(\Omega)$, $p_{i,j}$ is the jth roots of $P_{Ni}(\Omega)$ and $f_{i,j}$ is the jth roots of $F_{Ni}(\Omega)$, and NP_i and NF_i are the number of roots of $P_{Ni}(\Omega)$ and $F_{Ni}(\Omega)$. The multi-band lowpass domain bandwidths δ_1 and δ_2 in (2-8) will be explained in the next section.

The case can be extended to multi-band situation that suppose there are m passbands for a multi-band filter and corresponding filtering function for each passband is C_{N1}, C_{N2}, …, and C_{Nm} so that the composite filtering function can be obtained as

$$
\begin{aligned}
\varepsilon C_N(\Omega) &= \frac{1}{\dfrac{1}{\varepsilon_1 C_{N1}(\Omega)} + \dfrac{1}{\varepsilon_2 C_{N2}(\Omega)} + \cdots + \dfrac{1}{\varepsilon_m C_{Nm}(\Omega)}} \\[2mm]
&= \left(\prod_{j=1}^{m} \varepsilon_j \right) \frac{F_{N1}(\Omega) F_{N2}(\Omega) \cdots F_{Nm}(\Omega)}{\displaystyle\sum_{i=1}^{m} \left(P_{Ni}(\Omega) \left(\prod_{\substack{j=1 \\ j \neq i}}^{m} \varepsilon_j F_{Nj}(\Omega) \right) \right)} \\[2mm]
&= \varepsilon \frac{F_N(\Omega)}{P_N(\Omega)},
\end{aligned}
\qquad (2\text{-}9)
$$

where P_{Ni} is the numerator and F_{Ni} is the denominator of C_{Ni}. Here, each passband has individual filter order and the number of transmission zeros. By carefully placing the transmission zeros, the requested frequency response can be obtained under desired specifications.

To update the numerators $F_N(\Omega)$, $P_N(\Omega)$, and ε and evaluate the denominator $E_N(\Omega)$ of

S_{11} and S_{21} in (2-1), the following equation is used:

$$
\begin{aligned}
\varepsilon &\leftarrow \varepsilon \times \frac{F_N Coef}{P_N Coef}, \\
F_N(\Omega) &\leftarrow F_N(\Omega)/F_N Coef, \\
P_N(\Omega) &\leftarrow P_N(\Omega)/P_N Coef, \\
E_N(\Omega) &= j\frac{P_N(\Omega)}{\varepsilon} + F_N(\Omega),
\end{aligned}
\tag{2-10}
$$

where $F_N Coef$ and $P_N Coef$ are the leading coefficients of $F_N(\Omega)$ and $P_N(\Omega)$.

In (2-10), the passivity of the rational function representations of the S-parameters is not guaranteed. To enforce the passivity, those roots of $E_N(\Omega)$ with positive real part in the s domain ($s = j\,\Omega$) are modified by changing the sign of the real parts, as shown in Figure 2-4. Finally, the transversal coupling matrix based on the generated polynomials is obtained using the method in [93].
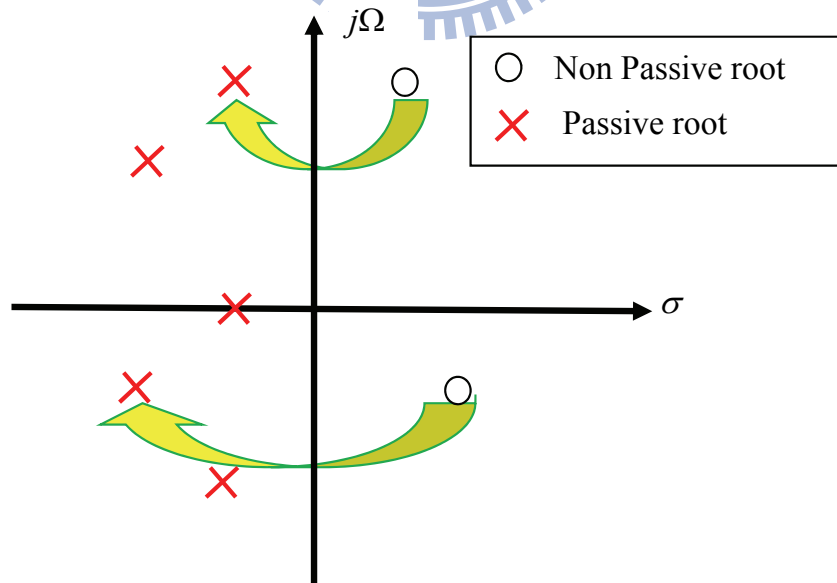
Figure 2-4. The passivity enforcement for polynomial $E_N(\Omega)$.

To transfer the response to the bandpass domain, the following equation is used:

$$\Omega = \frac{f_C}{f_H - f_L}\left(\frac{f}{f_C} - \frac{f_C}{f}\right)$$

$$= \frac{1}{\Delta}\left(\frac{f}{f_C} - \frac{f_C}{f}\right),$$

(2-11)

where Ω is the frequency in the multi-band low-pass domain, f is the frequency in the bandpass domain, f_C, f_H, and f_L are the central frequency, the upper edge of the highest passband, and the lower edge of the lowest passband in the bandpass domain, respectively, and Δ is the fractional bandwidth.

2.3 Frequency Transformation
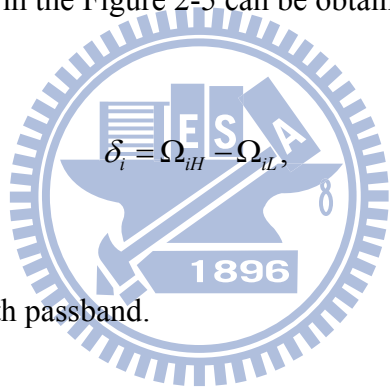
The previous procedure to synthesize the multi-band filtering function begins with the filter information in the lowpass domain. The practical specifications, however, are almost described in the bandpass domain. To relate with the information between two domains, here the frequency transformation is provided. Figure 2-5 shows the variables in the bandpass domain and the lowpass domain. In this figure, the relations between variables of the i-th passband in the bandpass domain are shown below:

$$\Delta_i = \frac{f_{iH} - f_{iL}}{f_i},$$

$$f_i = \sqrt{f_{iH}f_{iL}}.$$

(2-12)

Based on (2-11) and (2-12), the following relations can be derived:

$$f_{iH} = \frac{\Delta_i f_i + \sqrt{(\Delta_i f_i)^2 + 4f_i^2}}{2},$$

$$f_{iL} = \frac{-\Delta_i f_i + \sqrt{(\Delta_i f_i)^2 + 4f_i^2}}{2},$$

$$f_C = \sqrt{f_{1L} f_{2H}}, \tag{2-12}$$

$$\Delta = \frac{f_{2H} - f_{1L}}{f_C},$$

$$\Omega = \frac{1}{\Delta}\left(\frac{f}{f_C} - \frac{f_C}{f}\right).$$

The requested specifications are return loss (RL), the central frequencies and fractional bandwidths of both passbands in the bandpass domain. The so-called multi-band lowpass domain bandwidth δ_1 and δ_2 in the Figure 2-5 can be obtained as

$$\delta_i = \Omega_{iH} - \Omega_{iL}, \tag{2-13}$$

where i is the index of the i-th passband.
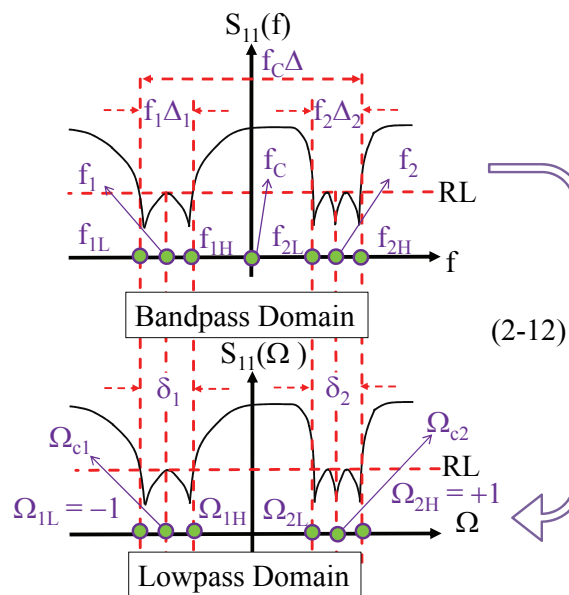
Figure 2-5. The requested design variables in the bandpass domain and the lowpass domain. RL is the prescribed return loss.

The corresponding transmission zeros in lowpass domain can also be obtained using (2-12). When inserting the transmission zeros in the single-band coupling matrix synthesis procedure [90], the transmission zeros in the single-band lowpass domain should be modified as

$$P_{TZ,i,j} = \frac{2}{\delta_i} \left(\Omega_{TZ,i,j} - \Omega_{ci} \right) \qquad (2\text{-}14)$$

where δ_i is the multi-band lowpass domain bandwidth of the i-th passband, $\Omega_{TZ,i,j}$ is the j-th transmission zero of the i-th passband in the lowpass domain, and $P_{TZ,i,j}$ is the j-th transmission zero of the i-th passband for inserting into the synthesis procedure in [90].

2.4 Computational Examples
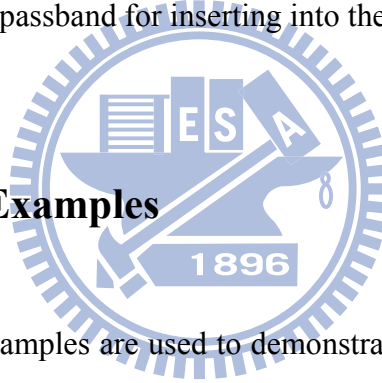
In this section, three examples are used to demonstrate the validation of the proposed synthesis procedure in dual-band filter design. Moreover, prescribed transmission zeros are discussed to be properly described in single-band filtering function.

2.4.1 Example 1: Symmetric Dual-band Bandpass Filter

In this example, the specifications of symmetrical dual-band bandpass filter are provided. Two passbands both are with the filter has filter order 3 and return loss 20 dB. The first passband has a central frequency at 2.32 GHz and 5% fractional bandwidth. The second passband has a central frequency at 2.695 GHz and 5% fractional bandwidth. The transmission zeros are 2.151 GHz, 2.5 GHz, and 2.905 GHz.

To apply (2-5) to design the dual-band filter, these specifications of frequency are firstly transferred into the lowpass domain using (2-11), (2-12) and (2-13), and then the corresponding polynomials are shifted and shrank using (2-8). The requested variables in the synthesis procedure are listed in Table 2.1.

Table 2.1 shows the variables in the lowpass domain used in the proposed synthesis procedure. The passband #1 has the central frequency at -0.75 rad/s and the transmission zero at -1.5 rad/s, while the passband #2 has the central frequency at 0.75 rad/s and the transmission zero at 1.5 rad/s. Applying the synthesis procedure in [93], all central frequencies in each passband need to be shifted to 0 rad/s. Hence the frequency domain in passband #1 needs to be shifted by +0.75 rad/s, that is, the central frequency is 0 rad/s (-0.75 + 0.75) with transmission zero at –0.75 rad/s (-1.5 + 0.75), and the Ω_{si} is +0.75 rad/s in (2-7). For the frequency domain in passband #2, it needs to be shifted by -0.75 rad/s, so that the central frequency is 0 rad/s (0.75 – 0.75) with transmission zero at 0.75 rad/s (1.5 – 0.75), and the Ω_{si} is 0.75 rad/s in (2-7). The transmission zero Ω_{TZ2} listed in Table 2.1 is the intrinsic transmission zero from the proposed synthesis procedure, which will be discussed latter. The settings in the synthesis procedure are listed in Table 2.2 and the resulting coupling matrix is listed in Table 2.3.

Table 2.1 The Requested Frequency Variables in Example 1.

Specifications		Bandpass Domain		Lowpass Domain	
f_1	2.32 GHz	f_C	2.5 GHz	Ω_1 (2-12)	-0.5 rad/s
f_2	2.695 GHz	f_{1L}	2.26 GHz	Ω_2 (2-12)	0.5 rad/s
Δ_1	5 %	f_{1H}	2.38 GHz	Ω_{C1} (2-12)	-0.75 rad/s
Δ_2	5 %	f_{2L}	2.63 GHz	Ω_{C2} (2-12)	0.75 rad/s
TZ_1	2.151 GHz	f_{2H}	2.76 GHz	Ω_{TZ1} (2-12)	-1.5 rad/s
TZ_2	2.5 GHz	Δ	25 %	Ω_{TZ2} (2-12)	0 rad/s

TZ₃	2.905 GHz	f_C	2.5 GHz	Ω_{TZ3} (2-12)	1.5 rad/s

Table 2.2 The Requested Setting Variables in Synthesis Procedure in Example 1.

Bassband	RL	Filter Order	Ω_C	Ω_{TZ}	δ (2–13)	P_{TZ} (2-14)
#1	20	3	-0.75 rad/s	-1.5 rad/s	0.5 rad/s	-3 rad/s
#2	20	3	0.75 rad/s	1.5 rad/s	0.5 rad/s	3 rad/s

After applying the procedure in [90], the corresponding $F'_{N1}(\Omega)$, $P'_{N1}(\Omega)$, $F'_{N2}(\Omega)$, and $P'_{N2}(\Omega)$ are obtained in Table 2.4. Applying (2-8), the synthesized polynomials are then shifted and shank, and then $P_N(\Omega)$ and $F_N(\Omega)$ of the dual-band filter are obtained. Finally, applying (2-10) to update $P_N(\Omega)$ and $F_N(\Omega)$ and obtain the $E_N(\Omega)$ and ε. Finally, the representation of dual-band filter in (2-1) can be completed. Table 2.4 shows the calculated polynomials. To check the passivity, the synthesized $E_N(\Omega)$ has roots as shown in Table 2.5. To enforce the passivity, the negative imaginary parts of those roots need to be changed as positive.

The magnitude and phase of the composite filtering function and the S-parameters are shown in Figure 2-6. The transmission zeros of the composite filtering function are slightly shifted (2.121 GHz and 2.945 GHz in Figure 2-6(b)), and this can be noted in Figure 2-6(a). The frequency shift comes from the combination of two filtering functions and can be eliminated by careful designing these two filtering functions. Figure 2-6(b) shows the corresponding S-parameters. In this figure an additional transmission zero 0 rad/s is introduced. This is because the phase of C_{N1} and C_{N2} is 180 degree out-of-phase around 0 rad/s. Furthermore, the transversal coupling matrix is obtained based on the derived polynomials and is shown in Table 2.3.

Table 2.3 Transversal Coupling Matrix for the Example 1.

	S	1	2	3	4	5	6	L
S	0.0	0.2432	-0.3811	0.2933	0.2933	-0.3811	0.2432	0.0
1	0.2432	1.1169	0.0	0.0	0.0	0.0	0.0	0.2432
2	-0.3811	0.0	0.8712	0.0	0.0	0.0	0.0	0.3811
3	0.2933	0.0	0.0	0.4212	0.0	0.0	0.0	0.2933
4	0.2933	0.0	0.0	0.0	-0.4212	0.0	0.0	0.2933
5	-0.3811	0.0	0.0	0.0	0.0	-0.8712	0.0	0.3811
6	0.2432	0.0	0.0	0.0	0.0	0.0	-1.1169	0.2432
L	0.0	0.2432	0.3811	0.2933	0.2933	0.3811	0.2432	0.0

Table 2.4 The Polynomials in (2-8) in the Example 1.

Passband #1		$\varepsilon_1 = 18.7449$
Before Freq. Shift	$F'_{N1}(\Omega)$	$\Omega^3 + 0.0429\,\Omega^2 - 0.0464\,\Omega - 0.0013$
	$P'_{N1}(\Omega)$	$\Omega + 0.75$
After Freq. Shift	$F_{N1}(\Omega)$	$\Omega^3 + 2.2929\omega^2 + 1.7054\,\Omega + 0.4098$
	$P_{N1}(\Omega)$	$\Omega + 1.5$
Passband #2		$\varepsilon_2 = -18.7449$
Before Freq. Shift	$F'_{N2}(\Omega)$	$\Omega^3 - 0.0429\,\Omega^2 - 0.0464\,\Omega + 0.0013$
	$P'_{N2}(\Omega)$	$\Omega - 0.75$
After Freq. Shift	$F_{N2}(\Omega)$	$\Omega^3 - 2.2929\omega^2 + 1.7054\,\Omega - 0.4098$
	$P_{N2}(\Omega)$	$\Omega - 1.5$
Dual-band (2-8) & (2-10)		
After (2-8)	$F_N(\Omega)$	$F_N(\Omega)= F_{N1}(\Omega)\, F_{N2}(\Omega)$
		$\Omega^6 - 1.8465\Omega^4 + 1.0290\,\Omega^2 - 0.1680$
	$P_N(\Omega)$	$P_N(\Omega)= P_{N1}(\Omega)\, \varepsilon_2\, F_{N2}(\Omega)$
		$+ P_{N2}(\Omega)\, \varepsilon_1\, F_{N1}(\Omega)$
		$29.7255\,\Omega^3 - 80.5389\Omega$

	$\varepsilon =\varepsilon_1\varepsilon_2$	-351.372
After (2-10)	$F_N(\Omega)$	$\Omega^6 - 1.8465\Omega^4 + 1.0290\,\Omega^2 - 0.1680$
	$P_N(\Omega)$	$\Omega^3 - 2.7094\,\Omega$
	ε	-11.8206
	$E_N(\Omega)$ (non-passive)	$\Omega^6 - 1.8465\,\Omega^4 - j0.0846\,\Omega^3 + 1.029\,\Omega^2 + j0.2292\,\Omega - 0.168$
	$E_N(\Omega)$ (passive)	$\Omega^6 - j1.1616\,\Omega^5 - 2.52121\,\Omega^4 + j1.7398\,\Omega^3 + 1.57656\,\Omega^2 - j0.4863\,\Omega - 0.168$

Table 2.5 Roots of Non-passive and Passive $E_N(\Omega)$.

Roots of $E_N(\Omega)$ (non-passive)	Roots of $E_N(\Omega)$ (passive)
1.0702 - j0.1037	1.0702 + j0.1037
-1.0702 - j0.1037	-1.0702 + j0.1037
0.8214 + j0.2904	0.8214 + j0.2904
-0.8214 + j0.2904	-0.8214 + j0.2904
0.3957 - j0.1867	0.3957 + j0.1867
-0.3957 - j0.1867	-0.3957 + j0.1867
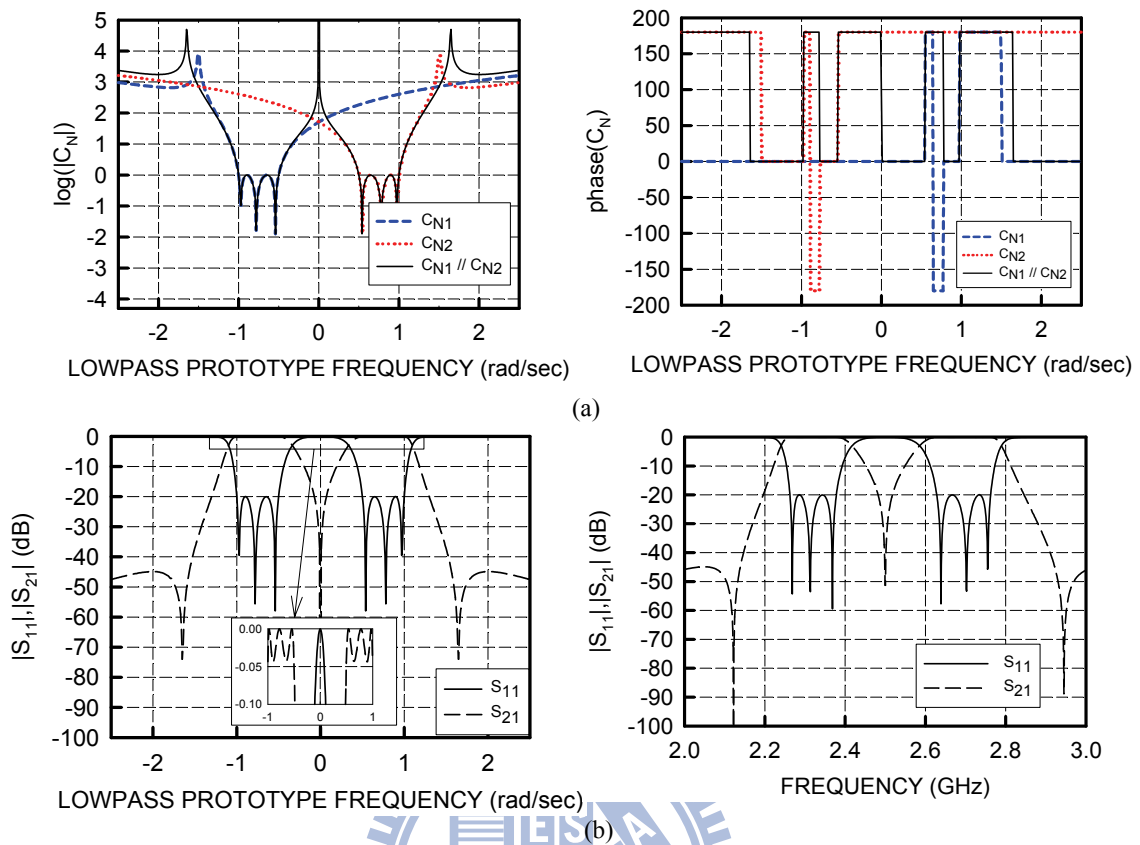
Figure 2-6. (a) Filtering functions for two single-band filters of same order 3 (C_{N1} has the transmission zeros at -1.5 and central frequency -0.75 rad/s and C_{N2} has the transmission zeros at 1.5 and central frequency 0.75 rad/s), and the composite dual-band filtering function ($CN_1 // CN_2$). The in-band return loss level is 20 dB in each case. (b) Corresponding S_{11} and S_{21} for the symmetric dual-band filter in lowpass and bandpass domains.

To modify the transmission zeros in each bassband to achieve the specifications, that is, transmission zeros are 2.151 GHz, 2.5 GHz, and 2.905 GHz.

2.4.2 Example 2: Asymmetric Dual-band Bandpass Filters

For an asymmetrical dual-band bandpass filter, the frequency response is not symmetric about the central frequency. Two filtering functions used to illustrate the dual-band characteristic have following specifications. Passband #1 is the third-order

function, which has central frequency at 1.8 GHz with transmission zeros at 1.613 GHz and 2 GHz, and the fractional bandwidth is 9.1%. Passband #2 is the fifth-order function, and it has the central frequency at 2.24 GHz with transmission zeros at 2 GHz and 2.495 GHz, and the fractional bandwidth is 7.28%. Return loss is 20 dB for both passbands. The requested frequency variables can be obtained using the proposed procedure and are listed in Table 2.6. Table 2.7 shows the requested setting variables, and the synthesized polynomials are listed in Table 2.8. The corresponding responses are shown in Figure 2-7 and the transversal coupling matrix is listed in Table 2.9.

(a)   (b)
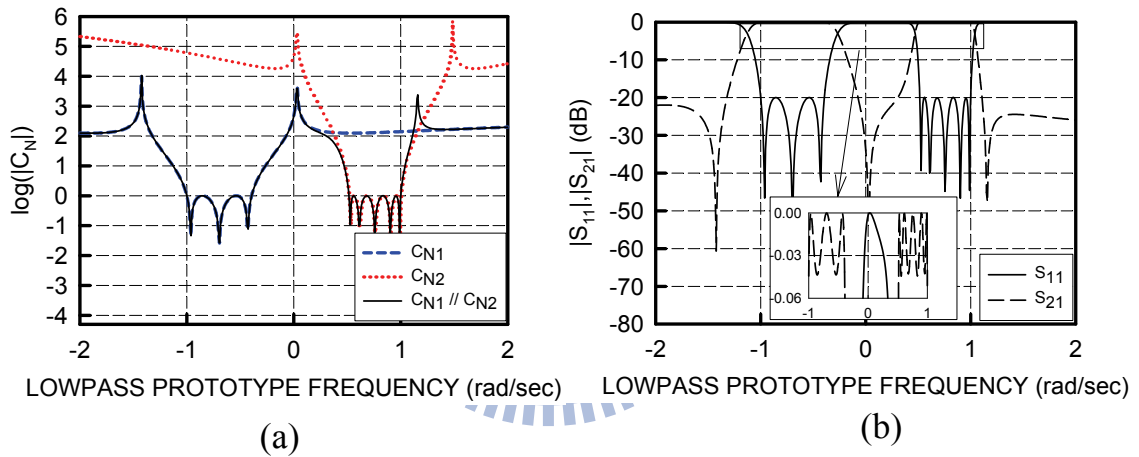
Figure 2-7. (a) Filtering functions for two single-band filters of different order 3 (C_{N1} has the transmission zeros at -1.433 rad/s and 0.004 rad/s and central frequency -0.696 rad/s, and its multi-band lowpass domain bandwidth δ_1 is 0.607 rad/s.) and order 5 (C_{N2} has the transmission zeros at 0.004 rad/s and 1.482 rad/s and central frequency 0.756 rad/s, and its multi-band lowpass domain bandwidth δ_2 is 0.486 rad/s), and the composite dual-band filtering function (CN_1 // CN_2). The in-band return loss level is 20 dB in each case. (b) Corresponding S_{11} and S_{21} for the symmetric dual-band filter in lowpass domains.

Table 2.6 The Requested Frequency Variables in Example 2.

Specifications		Bandpass Domain		Lowpass Domain	
f_1	1.8 GHz	f_C	2 GHz	Ω_1 (2-12)	-0.393 rad/s
f_2	2.24 GHz	f_{1L}	1.72 GHz	Ω_2 (2-12)	0.514 rad/s

Δ_1	9.1 %	f_{1H}	1.88 GHz	Ω_{C1} (2-12)	-0.696 rad/s
Δ_2	7.28 %	f_{2L}	2.16 GHz	Ω_{C2} (2-12)	0.756 rad/s
TZ_1	1.613 GHz	f_{2H}	2.32 GHz	Ω_{TZ1} (2-12)	-1.433 rad/s
TZ_2	2 GHz	Δ	30.2 %	Ω_{TZ2} (2-12)	0.004 rad/s
TZ_3	2.495 GHz	f_C	2 GHz	Ω_{TZ3} (2-12)	1.482 rad/s

Table 2.7 The Requested Setting Variables in Synthesis Procedure in Example 2.

Bassband	RL	Filter Order	Ω_C	Ω_{TZ}	δ (2–13)	P_{TZ} (2-14)
#1	20	3	-0.696 rad/s	-1.433 rad/s	0.607 rad/s	-2.43 rad/s
				0.004 rad/s		2.31 rad/s
#2	20	5	0.756 rad/s	0.004 rad/s	0.486 rad/s	-3.09 rad/s
				1.482 rad/s		2.99 rad/s

Table 2.8 The Polynomials in (2-8) in the Example 2.

Passband #1		ε_1 = -2.1098
Before Freq. Shift	$F'_{N1}(\Omega)$	$\Omega^3 - 0.0038\Omega^2 - 0.0712\Omega + 0.0002$
	$P'_{N1}(\Omega)$	$\Omega^2 + 0.0371\Omega - 0.5155$
After Freq. Shift	$F_{N1}(\Omega)$	$\Omega^3 + 2.0842\Omega^2 + 1.3767\Omega + 0.2859$
	$P_{N1}(\Omega)$	$\Omega^2 + 1.4291\Omega - 0.0053$
Passband #2		ε_2 = -982.038
Before Freq. Shift	$F'_{N2}(\Omega)$	$\Omega^5 - 0.0016\Omega^4 - 0.0746\Omega^3 + 0.0011\Omega$
	$P'_{N2}(\Omega)$	$\Omega^2 + 0.0278\Omega - 0.5460$
After Freq. Shift	$F_{N2}(\Omega)$	$\Omega^5 - 3.7848\Omega^4 + 5.6553\Omega^3 - 4.1679\Omega^2 + 1.5144\Omega - 0.2170$

	$P_{N2}(\Omega)$	$\Omega^2 - 1.4855\Omega + 0.0055$
	Dual-band (2-8) & (2-10)	
After (2-8)	$F_N(\Omega)$	$F_N(\Omega) = F_{N1}(\Omega)\, F_{N2}(\Omega)$
		$\Omega^8 - 1.7006\Omega^7 - 0.8561\Omega^6 + 2.6940\Omega^5$ $- 0.4685\Omega^4 - 1.1816\Omega^3 + 0.4409\Omega^2$ $+ 0.1343\Omega - 0.0620$
	$P_N(\Omega)$	$P_N(\Omega) = P_{N1}(\Omega)\,\varepsilon_2\,F_{N2}(\Omega) + P_{N2}(\Omega)\,\varepsilon_1\,F_{N1}(\Omega)$
		$-982.038\Omega^7 + 2313.4\Omega^6 - 243.587\Omega^5$ $- 3867.55\Omega^4 + 4403.23\Omega^3 - 1922.36\Omega^2$ $+ 315.313\Omega - 1.1484$
	$\varepsilon = \varepsilon_1\varepsilon_2$	6628.44
After (2-10)	$F_N(\Omega)$	$\Omega^8 - 1.7006\Omega^7 - 0.8561\Omega^6 + 2.6940\Omega^5$ $- 0.4685\Omega^4 - 1.1816\Omega^3 + 0.4409\Omega^2$ $+ 0.1343\Omega - 0.0620$
	$P_N(\Omega)$	$\Omega^7 - 2.3557\Omega^6 + 0.2480\Omega^5 + 3.9383\Omega^4$ $- 4.4837\Omega^3 + 1.9575\Omega^2 - 0.3211\Omega$ $+ 0.0017$
	ε	-6.74968
	$E_N(\Omega)$	$\Omega^8 + (-1.7006 - j1.1821)\Omega^7$ $+ (-1.5438 + j2.1130)\Omega^6$ $+ (3.9706 + j0.4535)\Omega^5$ $+ (-0.7528 - j2.6417)\Omega^4$ $+ (-1.8490 + j1.1961)\Omega^3$ $+ (0.8828 + j0.2649)\Omega^2$ $+ (0.0496 - j0.2259)\Omega$ $+ (-0.0570 + j0.02439)$

Table 2.9 Transversal Coupling Matrix for the Example 2 without Transmission Zeros Adjustment.

	S	1	2	3	4	5	6	7	8	L
S	0.0	-0.2686	0.4522	-0.2492	-0.1545	0.2322	-0.2586	0.2723	-0.1829	0.0
1	-0.2686	1.1440	0.0	0.0	0.0	0.0	0.0	0.0	0.0	0.2686
2	0.4522	0.0	0.7590	0.0	0.0	0.0	0.0	0.0	0.0	0.4522
3	-0.2492	0.0	0.0	0.3003	0.0	0.0	0.0	0.0	0.0	0.2492
4	-0.1545	0.0	0.0	0.0	-0.4700	0.0	0.0	0.0	0.0	0.1545
5	0.2322	0.0	0.0	0.0	0.0	-0.5761	0.0	0.0	0.0	0.2322
6	-0.2586	0.0	0.0	0.0	0.0	0.0	-0.7902	0.0	0.0	0.2586
7	0.2723	0.0	0.0	0.0	0.0	0.0	0.0	-1.0004	0.0	0.2723
8	-0.1829	0.0	0.0	0.0	0.0	0.0	0.0	0.0	-1.0672	0.1829
L	0.0	0.2686	0.4522	0.2492	0.1545	0.2322	0.2586	0.2723	0.1829	0.0

It is noted, however, that the transmission zero on the upper stopband of the composite filtering function is seriously influenced by the filtering function C_{N1}. Because the filtering function C_{N1} has a lower order, the function value at the out-of-band is smaller than that of C_{N2}. To compute the composite filtering function using (2-9), the filtering function with smaller value will dominate the response of the composite filtering function. Hence, the transmission zeros on the upper stopband of the composite filtering function shifts inward with respect to the transmission zeros of C_{N2}. This can be overcome by pre-adjusting the zero of C_{N2} to a higher frequency or by the method described in the following paragraph.

The alternative method to overcome the zero-shifting problem is to take advantage of the generalized Chebyshev characteristic, that is, for an *N-th* order filtering function, the number of transmission zeros can be smaller than or equal to *N*. It implies no infinite transmission zeros. Figure 2-8 shows an example, where TZs in the figure denotes the abbreviation of transmission zeros.

In this case, these two filtering functions with same order 4 have transmission zeros at (-6 and 0) rad/s and (-6, 0, and 6) rad/s, and have the central frequency at -3 rad/s,

respectively. The filtering function with three transmission zeros has no infinite transmission zeros, so the stopband rejection is worse due to no infinite transmission zeros. The stopband rejection, however, can still be kept under an acceptable level. As shown in Figure 2-8, the filtering function with three transmission zeros has the logarithm value close to 2.5 even the frequency up to 60 rad/s, which is -30 dB in S_{21}.
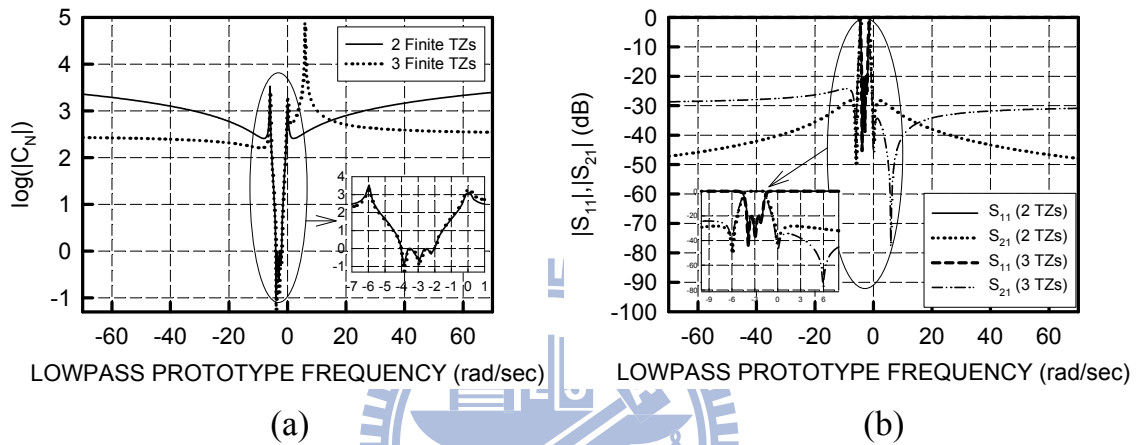
Figure 2-8. (a) Two third-order filtering functions. Solid line: filtering function has two finite transmission zeros at -6 and 0 rad/s, and the central frequency is -3 rad/s on the normalized lowpass domain. Dashed line: filtering function with 3 finite transmission zeros at -6, 0 and 6 rad/s, and the central frequency is -3 rad/s on the original lowpass domain. The in-band return loss is 20 dB in each case. (b) The corresponding S_{11} and S_{21}.

Use the above property, the example for asymmetric dual-band filter is modified. One third-order filtering function C_{N1} has transmission zeros at -1.433, 0.0037, and 1.4134 rad/s, and it has the central frequency at -0.696 rad/s with the milti-band lowpass domain bandwidth δ_1 of 0.6066 rad/s. The other one is the fifth-order filtering function C_{N2}, and it has the central frequency at 0.7566 rad/s and the transmission zeros at 0.0037 and 1.4818 rad/s with the milti-band lowpass domain bandwidth δ_2 of 0.4857 rad/s. In this case, the transmission zeros at 1.4134 rad/s of C_{N1} precisely locates the transmission zero on the upper stopband for the composite filtering function. Table 2.10 shows the corresponding

coupling matrix and the performances are shown in Figure 2-9. Compared with the results in Figure 2-7, the upper stopband transmission zeros can be precisely located.

The S-parameters of the synthesized dual-band filter on the bandpass domain are shown in Figure 2-10. The transmission zeros are 1.613 GHz, 2 GHz, and 2.46 GHz, which are slightly shifted from the specifications (1.613 GHz, 2 GHz, and 2.495GHz).

Table 2.10 Transversal Coupling Matrix for the Example 2 with Transmission Zeros Adjustment.

	S	1	2	3	4	5	6	7	8	L
S	0.0	-0.2790	0.4538	-0.2370	-0.1524	0.2341	-0.2598	0.2686	-0.1918	0.0353
1	-0.2790	1.1509	0.0	0.0	0.0	0.0	0.0	0.0	0.0	0.2774
2	0.4538	0.0	0.7218	0.0	0.0	0.0	0.0	0.0	0.0	0.4527
3	-0.2370	0.0	0.0	0.3036	0.0	0.0	0.0	0.0	0.0	0.2361
4	-0.1524	0.0	0.0	0.0	-0.4704	0.0	0.0	0.0	0.0	0.1516
5	0.2341	0.0	0.0	0.0	0.0	-0.5758	0.0	0.0	0.0	0.2335
6	-0.2598	0.0	0.0	0.0	0.0	0.0	-0.7896	0.0	0.0	0.2592
7	0.2686	0.0	0.0	0.0	0.0	0.0	0.0	-0.9988	0.0	0.2679
8	-0.1918	0.0	0.0	0.0	0.0	0.0	0.0	0.0	-1.0693	0.1885
L	0.0353	0.2774	0.4527	0.2361	0.1516	0.2335	0.2592	0.2679	0.1885	0.0

(a)　　　　　　　　　　　　　(b)
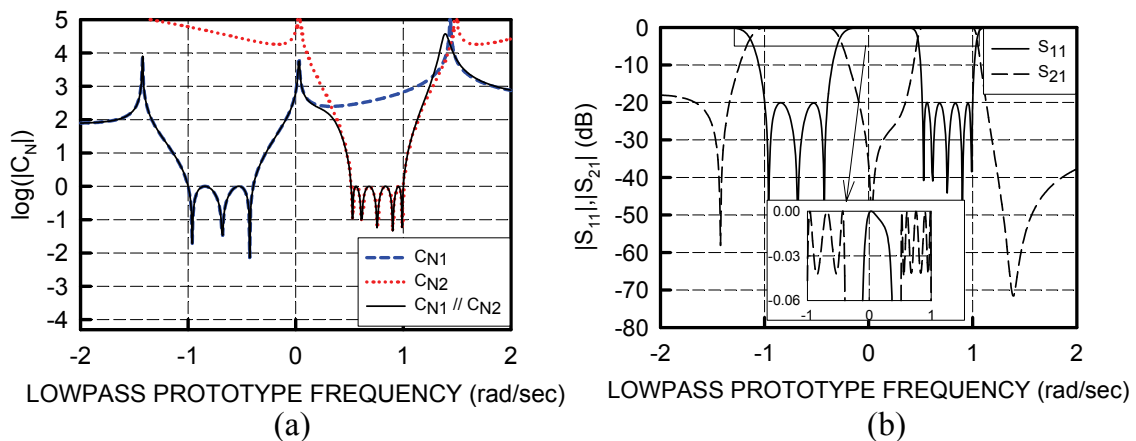
Figure 2-9 Filtering functions for two single-band filters of different order 3 (C_{N1} has the transmission zeros at -1.433, 0.0037, and 1.4134 rad/s and central frequency -0.696 rad/s and its milti-band lowpass domain bandwidth δ_1 is 0.6066 rad/s.) and order 5 (C_{N2} has the transmission zeros at 0.0037 rad/s and 1.4818 rad/s and central frequency 0.7566 rad/s with its multi-band lowpass domain bandwidth δ_2 is 0.4857 rad/s), and the composite dual-band

filtering function (CN_1 // CN_2). The in-band return loss is 20 dB in each case. (b) Corresponding S_{11} and S_{21} for the symmetric dual-band filter in lowpass domains.
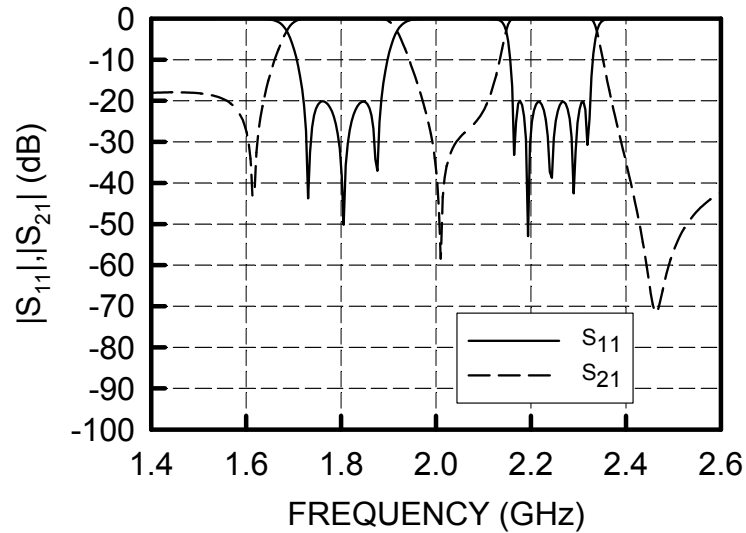
Figure 2-10 The S-parameters for the synthesized dual-band filter in Example 2.

2.4.3 Example 3: Multiband Bandpass Filters

In this example, a four-band filter is provided. There are four filtering functions in the example: 1) third-order filtering function C_{N1} with transmission zeros at -1.2 and -0.6 rad/s and the central frequency at -0.9 rad/s; 2) fourth-order C_{N2} with transmission zeros at -1.3, -0.65, and 0.01 rad/s and the central frequency at -0.3 rad/s; 3) fifth-order C_{N3} with transmission zeros at -1.3, -0.6, -0.01, 0.63, and 1.3 rad/s and the central frequency at 0.3 rad/s. and 4) third-order C_{N4} with transmission zeros at 1.35 and 0.6 rad/s and the central frequency at 0.9 rad/s. In every passbands, the multi-band lowpass domain bandwidth δ are all 0.2 rad/s. Figure 2-11 shows the frequency response and the corresponding polynomials are listed in Table 2.11.
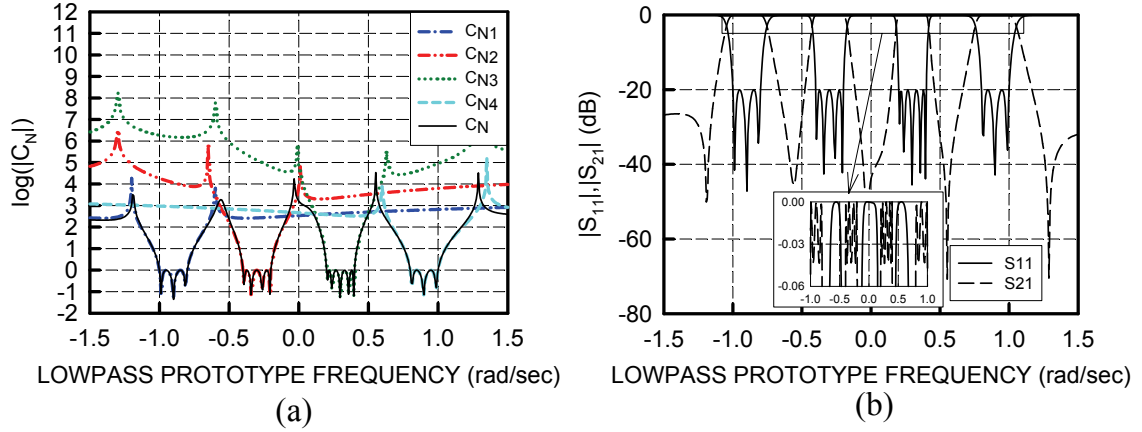
Figure 2-11 (a) Filtering functions for four single-band filters of degree 3 (C_{N1} has transmissions zeros at -1.2 and -0.6 rad/s and the central frequency at -0.9 rad/s), degree 4 (C_{N2} has transmissions zeros at -1.3, -0.65, and 0.01 rad/s and the central frequency at -0.3 rad/s), degree 5 (C_{N3} has transmissions zeros at -1.3, -0.6, -0.01, 0.63 and 1.3 rad/s and the central frequency at 0.3 rad/s), and degree 3 (C_{N4} has transmissions zeros at 1.35 and 0.9 rad/s and the central frequency at 0.6 rad/s), and the composite quad-band filter (C_{N1} // C_{N2} // C_{N3} // C_{N4}). The in-band return loss is 20 dB in each case. (b) The corresponding S_{11} and S_{21} for the quad-band filter.

Table 2.11 The Polynomials in (2-8) in the Example 3.

Passband #1		$\varepsilon_1 = -34.1407$
Before Freq. Shift	$F'_{N1}(\Omega)$	$\Omega^3 - 0.000181986\Omega^2 - 0.00764502\omega$
	$P'_{N1}(\Omega)$	$\Omega^2 + 0.03\Omega - 0.0899978$
After Freq. Shift	$F_{N1}(\Omega)$	$\Omega^3 + 2.6998\Omega^2 + 2.42203\Omega + 0.721973$
	$P_{N1}(\Omega)$	$\Omega^2 + 1.803\Omega + 0.722702$
Passband #2		$\varepsilon_2 = -829.275$
Before Freq. Shift	$F'_{N2}(\Omega)$	$\Omega^4 + 0.00303038\Omega^3 - 0.0101236\Omega^2$ $- 0.0000232139\Omega + 0.0000131248$
	$P'_{N2}(\Omega)$	$\Omega^3 + 1.04\Omega^2 - 0.0685\Omega - 0.1085$
After Freq. Shift	$F_{N2}(\Omega)$	$\Omega^4 + 1.20303\Omega^3 + 0.532604\Omega^2 + 0.102721\Omega$ $+ 0.00727686$
	$P_{N2}(\Omega)$	$\Omega^3 + 1.94\Omega^2 + 0.8255\Omega - 0.00845$

Passband #3		22365.6
Before Freq. Shift	$F'_{N3}(\Omega)$	$\Omega^5 + 0.00474399\Omega^4 - 0.0126341\Omega^3$ $- 0.0000480372\Omega^2 + 0.0000322607\Omega$ $+ 0.0000000623302$
	$P'_{N3}(\Omega)$	$\Omega^5 + 14.8\Omega^4 - 1.1923\Omega^3 - 1.57225\Omega^2$ $+ 0.137238\Omega + 0.147312$
After Freq. Shift	$F_{N3}(\Omega)$	$\Omega^5 - 1.49526\Omega^4 + 0.881673\Omega^3 - 0.256116\Omega^2$ $+ 0.0366375\Omega - 0.00206439$
	$P_{N3}(\Omega)$	$\Omega^5 - 0.02\Omega^4 - 2.0683\Omega^3 + 0.03002\Omega^2$ $+ 0.639327\Omega + 0.0063882$
Passband #4		−52.061
Before Freq. Shift	$F'_{N4}(\Omega)$	$\Omega^3 + 0.00590551\Omega^2 - 0.00758687\Omega$ $- 0.0000300976$
	$P'_{N4}(\Omega)$	$\Omega^2 - 0.15\Omega - 0.135$
After Freq. Shift	$F_{N4}(\Omega)$	$\Omega^3 - 2.69409\Omega^2 + 2.41178\Omega - 0.717418$
	$P_{N4}(\Omega)$	$\Omega^2 - 1.95\Omega + 0.81$
Quad-band (2-9) & (2-10)		
Before Normalization	$F_N(\Omega)$	$F_N(\Omega) = F_{N1}(\Omega)\, F_{N2}(\Omega)\, F_{N3}(\Omega)\, F_{N4}(\Omega)$
		$\Omega^{15} - 0.286502\Omega^{14} - 2.82599\Omega^{13} + 0.812423\Omega^{12}$ $+ 2.9528\Omega^{11} - 0.850408\Omega^{10} - 1.40287\Omega^9$ $+ 0.403472\Omega^8 + 0.308245\Omega^7 - 0.0880221\Omega^6$ $- 0.0326276\Omega^5 + 0.00921339\Omega^4 + 0.00159276\Omega^3$ $- 0.000443715\Omega^2 - 2.83092\Omega + 7.7809e{-}006$
	$P_N(\Omega)$	$P_N(\Omega) = P_{N1}(\Omega)\, \varepsilon_2 F_{N2}(\Omega)\, \varepsilon_3 F_{N3}(\Omega)\, \varepsilon_4 F_{N4}(\Omega)$ $+ P_{N2}(\Omega)\, \varepsilon_1 F_{N1}(\Omega)\, \varepsilon_3 F_{N3}(\Omega)\, \varepsilon_4 F_{N4}(\Omega)$ $+ P_{N3}(\Omega)\, \varepsilon_1 F_{N1}(\Omega)\, \varepsilon_2 F_{N2}(\Omega)\, \varepsilon_4 F_{N4}(\Omega)$ $+ P_{N4}(\Omega)\, \varepsilon_1 F_{N1}(\Omega)\, \varepsilon_2 F_{N2}(\Omega)\, \varepsilon_3 F_{N3}(\Omega)$
		$-1.47395e{+}006\Omega^{15} + 1.63681e{+}009\Omega^{14}$ $- 8.29053e{+}008\Omega^{13} - 3.58948e{+}009\Omega^{12}$ $+ 1.62202e{+}009\Omega^{11} + 2.012e{+}009\Omega^{10}$ $- 9.01956e{+}008\Omega^9 - 4.92454e{+}008\Omega^8$ $+ 2.30427e{+}008\Omega^7 + 6.79075e{+}007\Omega^6$ $- 3.91472e{+}007\Omega^5 - 3.44255e{+}006\Omega^4$ $+ 4.24542e{+}006\Omega^3 - 5.99681\Omega^2 + 26618.6\Omega$

		+ 1.634.24
	$\varepsilon =$ $\varepsilon_1\varepsilon_2\varepsilon_3\varepsilon_4$	-3.29659e+010
After Normalization (2-10) & (2-11)	$F_N(\Omega)$	Ω^{15} - $0.28602\Omega^{14}$ - $2.82599\Omega^{13}$ + $0.812423\Omega^{12}$ + $2.9528\Omega^{11}$ - $0.850408\Omega^{10}$ - $1.40287\Omega^{9}$ + $0.403472\Omega^{8}$ + $0.308245\Omega^{7}$ - $0.0880221\Omega^{6}$ - $0.0326276\Omega^{5}$ + $0.00921339\Omega^{4}$ + $0.00159276\Omega^{3}$ - $0.000443715\Omega^{2}$ - $2.83092e{-}005\Omega$ + $7.7809e{-}006$
	$P_N(\Omega)$	Ω^{15} - $1110.49\Omega^{14}$ + $562.47\Omega^{13}$ + $2435.27\Omega^{12}$ - $1100.45\Omega^{11}$ - $1365.04\Omega^{10}$ + $611.931\Omega^{9}$ + $334.104\Omega^{8}$ – $156.333\Omega^{7}$ - $46.0717\Omega^{6}$ + $26.5593\Omega^{5}$ + $2.33559\Omega^{4}$ - $2.88029\Omega^{3}$ + $0.406852\Omega^{2}$ - 0.0180593Ω - 0.00110875
	ε	22365.6
	$E_N(\Omega)$	Ω^{15} + $(-0.286504 - j0.875341)\Omega^{14}$ + $(-3.20787 + j0.250893)\Omega^{13}$ + $(0.92138 + j2.17138)\Omega^{12}$ + $(3.69605 - j0.627009)\Omega^{11}$ + $(-1.06614 - j1.89376)\Omega^{10}$ + $(-1.89737 + j0.550201)\Omega^{9}$ + $(0.548417 + j0.714914)\Omega^{8}$ + $(0.446072 - j0.208215)\Omega^{7}$ + $(-0.128607 - j0.117792)\Omega^{6}$ + $(-0.0476098 + j0.034215)\Omega^{5}$ + $(0.0136772 + j0.00789931)\Omega^{4}$ + $(0.00206581 - j0.00228744)\Omega^{3}$ + $(-0.000587022 - j0.000157547)\Omega^{2}$ + $(-2.68674e{-}005 + j4.72142e{-}005)\Omega$ + $(7.77739e{-}006 - j2.38745e{-}007)$

In this case, the lower order filtering functions (i.e., C_{N1} and C_{N4}) are used to adjust the transmission zeros to specific locations, while the other filtering functions are used to be slightly tuned for the specific locations of transmission zeros. Table 2.12 shows the corresponding coupling matrix. The matrix elements not listed in Table 2.12 are all zero.

Table 2.12 Transversal Coupling Matrix for the Example 3

$M_{S,1}$	-0.1695	$M_{S,2}$	0.2604	$M_{S,3}$	-0.1560	$M_{S,4}$	0.1212
$M_{S,5}$	-0.1876	$M_{S,6}$	0.1874	$M_{S,7}$	-0.1195	$M_{S,8}$	-0.0983
$M_{S,9}$	0.1501	$M_{S,10}$	-0.1632	$M_{S,11}$	0.1591	$M_{S,12}$	-0.1085
$M_{S,13}$	-0.1508	$M_{S,14}$	0.2565	$M_{S,15}$	-0.1818	$M_{1,L}$	0.1695
$M_{2,L}$	0.2604	$M_{3,L}$	0.1560	$M_{4,L}$	0.1212	$M_{5,L}$	0.1876
$M_{6,L}$	0.1874	$M_{7,L}$	0.1195	$M_{8,L}$	0.0983	$M_{9,L}$	0.1501
$M_{10,L}$	0.1632	$M_{11,L}$	0.1591	$M_{12,L}$	0.1085	$M_{13,L}$	0.1508
$M_{14,L}$	0.2565	$M_{15,L}$	0.1818	$M_{1,1}$	1.0576	$M_{2,2}$	0.9416
$M_{3,3}$	0.7761	$M_{4,4}$	0.4298	$M_{5,5}$	0.3688	$M_{6,6}$	0.2458
$M_{7,7}$	0.1736	$M_{8,8}$	-0.1802	$M_{9,9}$	-0.2174	$M_{10,10}$	-0.3014
$M_{11,11}$	-0.3875	$M_{12,12}$	-0.4242	$M_{13,13}$	-0.7758	$M_{14,14}$	-0.9307
$M_{15,15}$	-1.0624						

2.5 Comparison with Other Method

In the coupling matrix synthesis of the dual-band or multi-band filter, the most popular and efficient analytical method is the analytical iterative method [102]. This method has features of user-defined number of passbands, number of transmission zeros, return loss level, range of each passband and stopband, and prescribed imaginary or complex transmission zeros. By efficient iterative procedure, the transmission zeros are extracted, and some fine tunes are needed if prescribed real transmission zeros are requested. The equal-ripple levels in different passbands are not necessarily identical but can be achieved by run-and-try process. The difference of return loss levels in different passbands, however, becomes large with consideration of different filter orders in different passbands.

Comparing the proposed method to the analytical iterative method, the above features of the iterative method are also the features of the proposed method. Moreover, the equal-ripple levels in different passbands are preserved. Here an example is given to show

the different passbands between these two methods. The specifications are listed in Table 2.13, and the requested return loss is 20 dB in both passbands for this example. The frequency responses obtained by these two methods are shown in Figure 2-12.

Table 2.13 The Specifications for the Method Comparison

Passband	# of poles	Stopband	# of zeros	Prescribed zeros
-1.0 to -0.6661	3	-∞ to -1.3	1	
		-0.45 to 0.37	2	none
0.6661 to 1.0	4	1.4 to ∞	1	
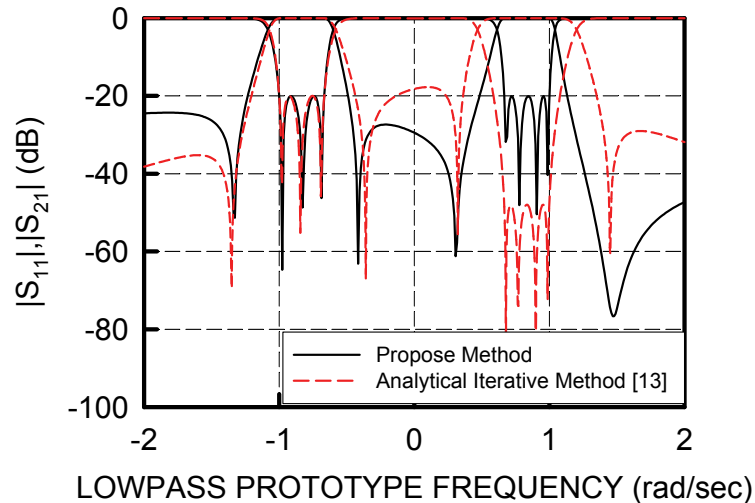
Figure 2-12 Frequency responses of the dual-band filter composed of the third- and fifth-order filtering functions. Solid line: the proposed method. Dashed line: the analytical iterative method.

In Figure 2-12, the settings in the proposed method are 1) a third order filter with normalized central frequency at -0.8333 rad/s with normalized transmission zeros at -1.333, -0.4167, and 1.4833 rad/s, and 2) a fifth order filter with normalized central frequency at 0.8333 rad/s with normalized transmission zeros at 1.5 rad/s. The responses of the passband with third-order are similar from two methods. For the passband with fourth order, due to the equal-ripple preservation in the proposed method, the return loss is kept to

be 20 dB, while the return loss is 50 dB from the iterative method. Hence, the second passband form the iterative method has wider bandwidth than that form the proposed method if the 20 dB return loss is used. Hence, for the filter composed of filtering functions with different orders, the proposed method holds the equal-ripple property.

To check the transmission zeros form two methods, due to the parallel addition in the proposed method, the number of transmission zeros will increase. The transmission zeros are -1.3528, -0.3528, 0.3232, and 1.4496 rad/s in the iterative method, while they are -1.333, -0.4151, 0.3099, 0.7936 $\pm$ j0.5468, and 1.4694 $\pm$ j0.047 rad/s in the proposed method. Although the additional complex prescribed transmission zeros 0.7936 $\pm$ j0.5468 rad/s can be added in the iterative method to pull back the return loss form 50 dB to 30 dB, but it is difficult to know the prescribed zeros in order to pull back the return loss.

For the filter composed of filtering functions with same filter order, the iterative method has the advantage in the specification assignment. The only thing the designer needs to do is to assign the ranges of each passband and each stopband, number of poles and zeros and the return loss level, so that the corresponding polynomials are generated. For the proposed method, the designer needs to assign the locations of transmission zeros first in order to design the characteristic of the multi-band filter. These two methods, however, both can analytically generate the coupling matrix for the multi-band filter. For the filter composed of filtering functions with different filter orders, the proposed method provides an alternative way to synthesis the multi-band filter with the equal-ripple property.

2.6 Other Properties in the Proposed Method

The synthesis of the dual-band and multi-band filters is shown to be valid by using the

proposed method. In the end of this chapter, three other properties are discussed.

2.6.1 Passbands with Different Return Loss

In the proposed method, the different return loss is available in each passband. For example, the settings for a dual-band filter are as follows: 1) a third-order filter with normalized central frequency at -0.7143 rad/s with transmission zeros at -1.5714 and 2.1429 rad/s. Its multi-band lowpass domain bandwidth δ_l is 0.5724 rad/s, and its return loss is 20 dB. 2) A fifth-order filter with the normalized central frequency at 0.7143 rad/s with transmission zeros at 2.1429 rad/s. Its multi-band lowpass domain bandwidth δ_2 is 0.5718 rad/s, and its return loss is 40 dB. The corresponding polynomials are listed in Table 2.15 and the transversal coupling matrix is shown in Table 2.14. The performances are shown in Figure 2-13. This example demonstrates the validity of synthesizing the dual-band filter with different return loss level in each passband. It is also valid in multi-band filter synthesis.

Table 2.14 The Transversal Coupling Matrix for the dual-band filter in Figure 2-13

	S	1	2	3	4	5	6	7	8	L
S	0	-0.2815	0.4250	-0.3085	-0.2301	0.3541	-0.3524	0.3969	-0.3159	0
1	-0.2815	1.1610	0	0	0	0	0	0	0	0.2815
2	0.4250	0	0.9028	0	0	0	0	0	0	0.4250
3	-0.3085	0	0	0.3962	0	0	0	0	0	0.3085
4	-0.2301	0	0	0	-0.2225	0	0	0	0	0.23013
5	0.3541	0	0	0	0	-0.4125	0	0	0	0.3541
6	-0.3524	0	0	0	0	0	-0.8048	0	0	0.3524
7	0.3969	0	0	0	0	0	0	-1.1795	0	0.3969
8	-0.3159	0	0	0	0	0	0	0	-1.2634	0.3159
L	0	0.2815	0.4250	0.3085	0.2301	0.3541	0.3524	0.3969	0.3159	0

(a)

(b)
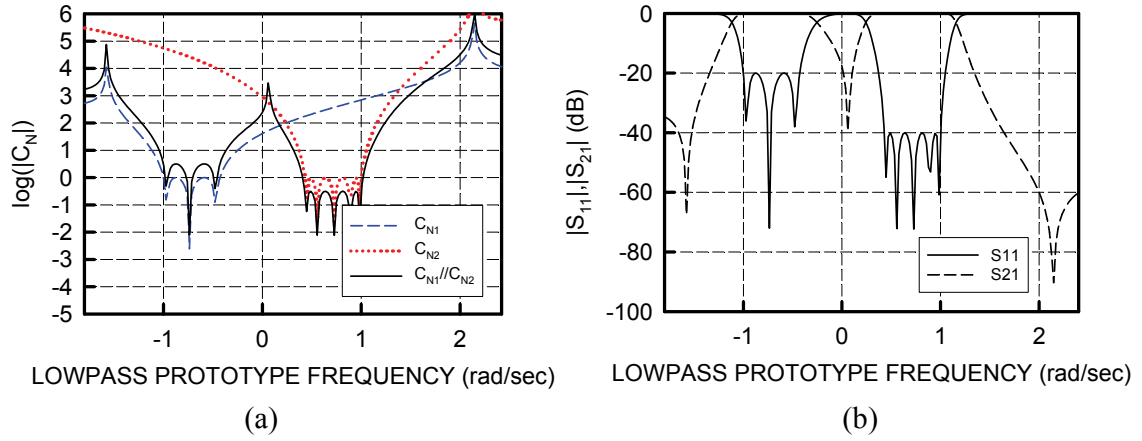
Figure 2-13 Filtering functions for two single-band filters of order 3 with return loss 20 dB (C_{N1} has the transmission zeros at -1.5714 and 2.1429 rad/s and the central frequency -0.7143 rad/s with the multi-band lowpass domain bandwidth δ_1 of 0.5724 rad/s) and order 5 with return loss 40 dB (C_{N2} has the transmission zero at 2.1429 rad/s the and the central frequency 0.7143 rad/s with the multi-band lowpass domain bandwidth δ_2 of 0.5718 rad/s), and the composite dual-band filtering function (CN_1 // CN_2). (b) Corresponding S_{11} and S_{21} for the symmetric dual-band filter in lowpass domains.

Table 2.15 The Polynomials for the Dual-band Filter in Figure 2-13.

Passband #1		ε_1= -40.688
Before Freq. Shift	$F'_{N1}(\Omega)$	$\Omega^3 + 0.0348251\Omega^2 - 0.0614816\Omega - 0.00143858$
	$P'_{N1}(\Omega)$	$\Omega^2 - 2.0001\Omega - 2.44891$
After Freq. Shift	$F_{N1}(\Omega)$	$\Omega^3 + 2.17773\Omega^2 + 1.51894\Omega + 0.336867$
	$P_{N1}(\Omega)$	$\Omega^2 - 0.5715\Omega - 3.36735$
Passband #2		ε_2= -118.459
Before Freq. Shift	$F'_{N2}(\Omega)$	$\Omega^5 - 0.028903\Omega^4 - 0.101965\Omega^3 + 0.00236228\Omega^2 + 0.00207508\Omega - 2.41362e\text{-}005$
	$P'_{N2}(\omega)$	$\Omega - 1.4286$
After Freq. Shift	$F_{N2}(\omega)$	$\Omega^5 - 3.6004\Omega^4 + 5.08285\Omega^3 - 3.51215\Omega^2 + 1.1864\Omega - 0.156616$
	$P_{N2}(\omega)$	$\Omega - 2.1429$

Dual-band (2-8) & (2-10)		
After (2-8)	$F_N(\Omega)$	$F_N(\Omega)= F_{N1}(\Omega)\, F_{N2}(\Omega)$
		$\Omega^8 - 1.42268\Omega^7 - 1.23889\Omega^6$ $+ 2.42498\Omega^5 - 0.045625\Omega^4 - 1.19546\Omega^3$ $+ 0.277884\Omega^2 + 0.161769\Omega - 0.0527589$
	$P_N(\Omega)$	$P_N(\Omega)= P_{N1}(\Omega)\, \varepsilon_2\, F_{N2}(\Omega) + P_{N2}(\Omega)\, \varepsilon_1\, F_{N1}(\Omega)$
		$-118.450\Omega^7 + 494.197\Omega^6 - 446.959\Omega^5$ $- 716.71\Omega^4 + 1647.78\Omega^3 - 1174.02\Omega^2$ $+ 581.374\Omega - 33.1014$
	$\varepsilon = \varepsilon_1\varepsilon_2$	4819.84
After (2-10)	$F_N(\Omega)$	$\Omega^8 - 1.42268\Omega^7 - 1.23889\Omega^6$ $+ 2.42498\Omega^5 + 0.0456254\Omega^4$ $- 1.19546\Omega^3 + 0.277884\Omega^2$ $+ 0.161769\Omega - 0.0527589$
	$P_N(\Omega)$	$\Omega^7 - 4.1719\Omega^6 + 3.77313\Omega^5$ $+ 6.0503\Omega^4 - 13.9102\Omega^3 + 9.91082\Omega^2$ $- 4.90783\Omega + 0.279435$
	ε	-40.688
	$E_N(\Omega)$	$\Omega^8 + (-1.42268 - j1.83172)\Omega^7$ $+ (-2.91618 + j2.24099)\Omega^6$ $+ (4.14107 + j2.81826)\Omega^5$ $+ (1.6612 - j3.65468)\Omega^4$ $+ (-2.84106 - j0.62744)\Omega^3$ $+ (0.140788 + j1.18397)\Omega^2$ $+ (0.323642 - j0.0861916)\Omega$ $+ (-0.0386639 - j0.0365482)$

2.6.2 Closely Adjacent Passbands

For the problem of closely adjacent passbands, the equal ripple characteristic might be affected due to parallel addition. However, even two passbands are close to each other and almost become one large passband, the return loss level is still lower than the specification. Here we give two examples.

For the first example, the passband #1 has the normalized central frequency at -0.4872 rad/s with the multi-band lowpass domain bandwidth δ_l of 1 rad/s, and the passband #2 has the normalized central frequency at 0.4847 rad/s with the multi-band lowpass domain δ_2 of 1 rad/s. The filter order is 3 and return loss is 20 dB in each passband. The corresponding polynomials are listed in Table 2.16 and the performance is shown in Figure 2-14 (a). In the figure, it can be noted that although the equal ripple characteristic has been affected slightly, the return loss is still larger than 20 dB within each passband.

For the second example, the different filter orders and return loss levels are used in each passband. The passband #1 has the normalized central frequency at -0.4872 rad/s, and its filter order is 3. The return loss is 20 dB. The passband #2 has the normalized central frequency at 0.4872 rad/s, and the filter order is 5 and return loss is 30 dB. The corresponding polynomials are listed in Table 2.16 and the performances are shown in Figure 2-14 (b). In the figure, it can be noted that the return loss is larger than 20 dB for passband #1 and 30 dB for passband #2.

Table 2.16 The Synthesized Polynomials in Two Examples with Closely Adjacent Passbands

Example #1	$F_N(\Omega)$	$\Omega^6 - 0.000102564\Omega^5 - 1.10651\Omega^4$ $+ 8.24019\text{e-}005\Omega^3 + 0.207899\Omega^2$ $- 3.63632\text{e-}006\Omega - 0.00038175$
	$P_N(\Omega)$	$\Omega^4 - 2564.1\Omega^3 - 0.0657462\Omega^2 - 1319.98\Omega$ $+ 0.00439994$
	ε	-3821.66
	$E_N(\Omega)$	$\Omega^6 + (-0.000102564 - j2.16546)\Omega^5$ $+ (-3.45111 + j0.000288766)\Omega^4$ $+ (0.00046724 + j3.12654)\Omega^3$ $+ (1.6354 - j0.000299605)\Omega^2$ $+ (-6.30921\text{e-}005 - j0.346969)\Omega$ $+ (-0.00038175 + j1.21151\text{e-}006)$
Example #2	$F_N(\Omega)$	$\Omega^8 - 0.974462\Omega^7 - 1.00056\Omega^6 + 1.07821\Omega^5$

		$+ 0.086371\Omega^4 - 0.206775\Omega^3 + 0.0224816\Omega^2$ $+ 0.00137135\Omega + 7.33732\text{e-}007$
	$P_N(\Omega)$	$\Omega^6 - 2566.05\Omega^5 + 6247.09\Omega^4 - 5778.09\Omega^3$ $+ 950.12\Omega^2 - 453.146\Omega - 10.5585$
	ε	-7643.31
	$E_N(\Omega)$	$\Omega^8 + (-0.974462 - j2.5058)\Omega^7$ $+ (-4.14008 + j2.28432)\Omega^6$ $+ (3.74292 + j4.25861)\Omega^5$ $+ (2.67563 - j3.63963)\Omega^4$ $+ (-2.11472 - j0.849448)\Omega^3$ $+ (-0.095197 + j0.589892)\Omega^2$ $+ (0.0607588 + j0.00368407)\Omega$ $+ (0.00136195 - j0.00023099)$
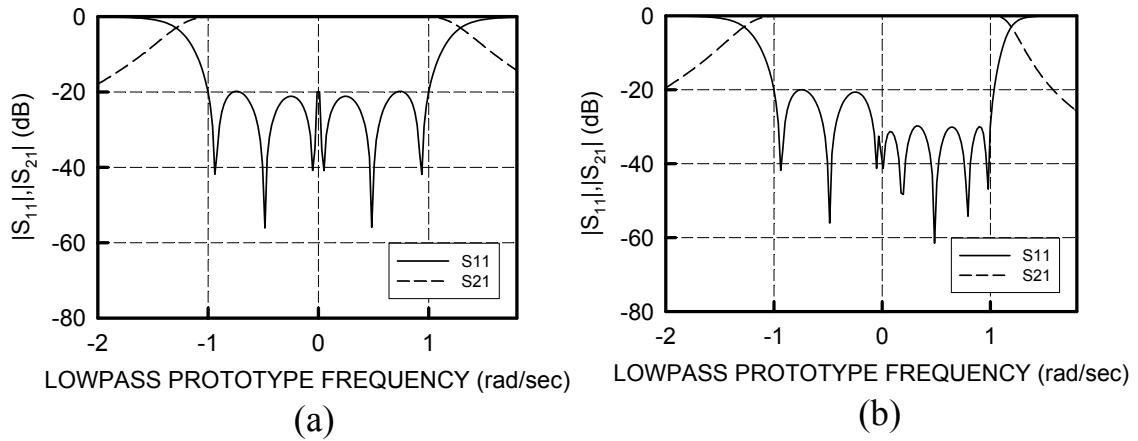
Figure 2-14 The S-parameters for the filters with two close adjacent passbands with polynomials in Table 2.16. (a) Equal ripple level, and (b) different ripple level.

From these two examples, the proposed method is shown to be valid to synthesize one single-band filter from two closely adjacent passbands, even if the return loss levels are different in each passband.

2.6.3 Intrinsic Transmission Zero

For the extra transmission zeros in Figure 2-6, when two filtering functions both have odd order, there will be an intrinsic transmission zero between two passbands after the parallel addition. But if there are two filtering functions, and they are both with even filter order, then the separation is not good enough after the parallel addition. Here we give an example. The passband #1 has Chebyshev characteristic with the normalized central frequency at -0.8 rad/s with the multi-band lowpass domain bandwidth δ_l of 0.4 rad/s, and it is the 3rd order filtering function. The passband #2 has Chebyshev characteristic with the normalized central frequency at 0.8 rad/s with the multi-band lowpass domain δ_2 of 0.4 rad/s, and it is the 5th order filtering function. The response is shown in Figure 2-15 (a). It is noted that there is no transmission zeros in each filtering function. After the parallel addition, one transmission zero is generated with the well isolation between two passbands.

(a)   (b)
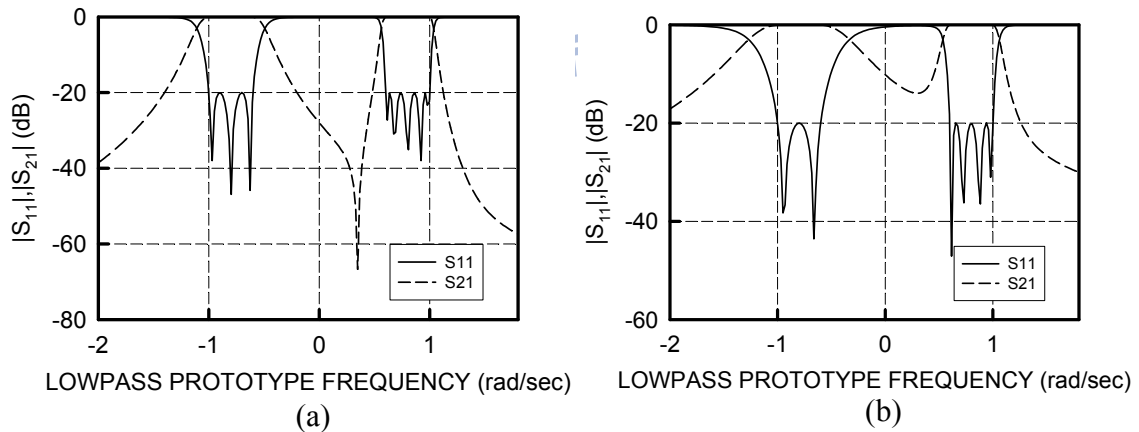
Figure 2-15 (a) Two odd-order filtering functions have been combined as a dual-mode filtering function with an extra transmission zeros, while two even-order filtering functions have been combined as a dual-mode filtering function has worse isolation between two passbands.

Another example is given for two filtering functions with even filter order. The filter

orders are modified as 2 and 4, and the other settings are same as those in the above example. The response is shown in Figure 2-15 (b). In this example, the isolation between two passbands is worse.

For the passband with one odd-order filtering function and one even-order filtering function, the odd-order one should be assigned as the upper passband in order to introduce the intrinsic transmission zero. To obtain the dual-band characteristic with odd-order filtering function as the lower passband and the even-order filtering function as the upper passband, no intrinsic transmission zero is introduced. To overcome the problem, the $\Omega = -\Omega$ is applied to the filtering function, which has the odd-order upper passband and even-order lower passband, to synthesize the dual-band characteristic, to generate an intrinsic transmission zero. The phenomenon can be observed in Figure 2-16.
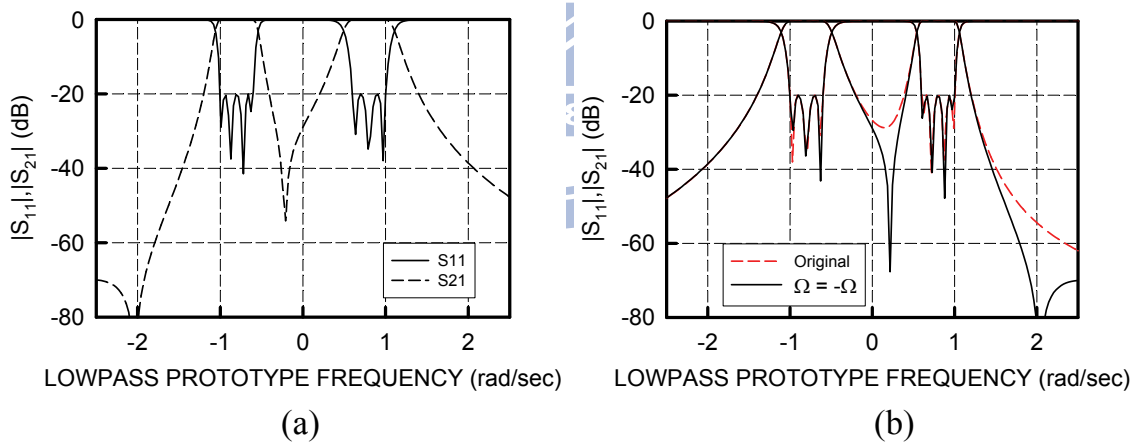
Figure 2-16 Two passbands with different order. (a) The odd-order upper passband and even-order lower passband are combined as the filtering function has an intrinsic transmission zero. (b) The even-order upper passband and odd-order lower passband are combined as the filtering function has no intrinsic transmission zero using the proposed method. But with $\Omega = -\Omega$ operation in the settings of (a), the extra intrinsic transmission zero can be introduced.

2.7 Conclusion

In this chapter, the novel analytical method to synthesize a dual-band or multi-band filtering function has been successfully developed. Based on the synthesized composite filtering function, the transversal coupling matrix can be obtained. Moreover, the arbitrarily located transmission zeros, arbitrary return losses within each passband, and various bandwidth of each passband are available in this method. Compared with the most popular method, analytical iterative method, the proposed method in this chapter provides the equal-ripple potential to give the practical insight in the filter design.
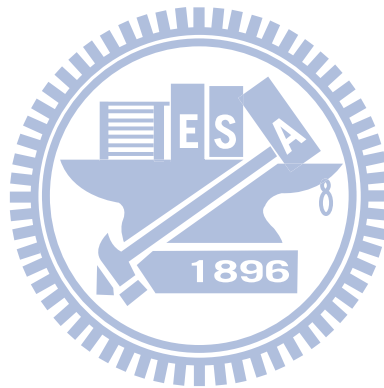
Chapter 3

Dual-band Filter Design Using Parallel-Coupled Line

3.1 Introduction

The coupling scheme corresponds to a physical placement of resonators in the filter design. By carefully adjusting the coupling strengths between resonators, the performance of the filter can be determined. For the single-band filter design, the coupling schemes are widely studied for the specific electrical responses. For examples, the tri-section topology is proposed for generating one transmission zero above or below the passband, and the quadruplet topology is used to generate two transmission zeros above and below the passband.

The coupling matrix provides an advantage of hardware implementation. Based on the advantage, the coupling matrix of the transversal topology needs to be transformed into some specific coupling schemes for practical realization of a filter. For the dual-band filter design, some coupling schemes, which are cul-de-sac [98], inline topology [97], and extended box topology [100], are generated via a series of similarity transformations, matrix rotation or optimization [98], [105]. Some of those topologies, however, are difficult to be realized by microstrip lines.

Considering the dual-band microstrip filter, dual-mode and frequency-separated coupling scheme is proposed to realized the dual-band filter characteristics. The phenomenon in placing transmission zeros related to corresponding coupling topology, however, is not clear yet such that the mechanism in transmission zeros generation of the dual-band filter is still unobservable under proper coupling scheme.

In this chapter, single-path and dual-path topologies are provided for the microstrip dual-band filter design. The single-path coupling scheme has rare physical insight and needs run-and-try process to check if the coupling scheme is valid for the requested specifications. For the dual-path coupling scheme, it is able to illustrate the dual-path characteristics via frequency-separated path. Furthermore, the mechanism of transmission zeros and the separation between two adjacent passbands, furthermore, will be studied via the coupling matrix.

3.2 Single-path Coupling Scheme

The single-path coupling scheme for a dual-band filter has a direct coupling path with some cross-coupling paths. To capture the phenomenon of the prescribed transmission zeros, the well-known cross-coupling topologies, such as tri-section and quadruplet coupling schemes, are used to the run-and-try process. To apply the trisection and quadruplet coupling schemes to the dual-band filter design in the single-path coupling scheme, finite transmission zeros will be placed to separate two passbands. Following is an example. A dual-band filter is designed to have two second-order filtering functions; one has a normalized transmission zero at 0 rad/s and the normalized central frequency at 0.75 rad/s with the multi-band lowpass domain bandwidth δ_1 of 0.5 rad/s, while the other one has a normalized transmission zero at 0 rad/s and the normalized central frequency at -0.75 rad/s with the multi-band lowpass domain bandwidth δ_2 of 0.5 rad/s. The return loss in each passband is 20 dB. The synthesized filtering functions and corresponding S-parameters are shown in Figure 3-1.

The transversal coupling matrix is shown in Table 3.1. Due to two transmission zeros from each passband are used to contribute the separation of two passbands, the quadruplet

topology is used. In order to convert the transversal coupling matrix for the single-path coupling scheme with quadruplet coupling scheme, the optimization proposed in [94] is used. The coupling scheme is shown in Figure 3-2 and the corresponding coupling matrix is listed in Table 3.2.

(a)

(b)
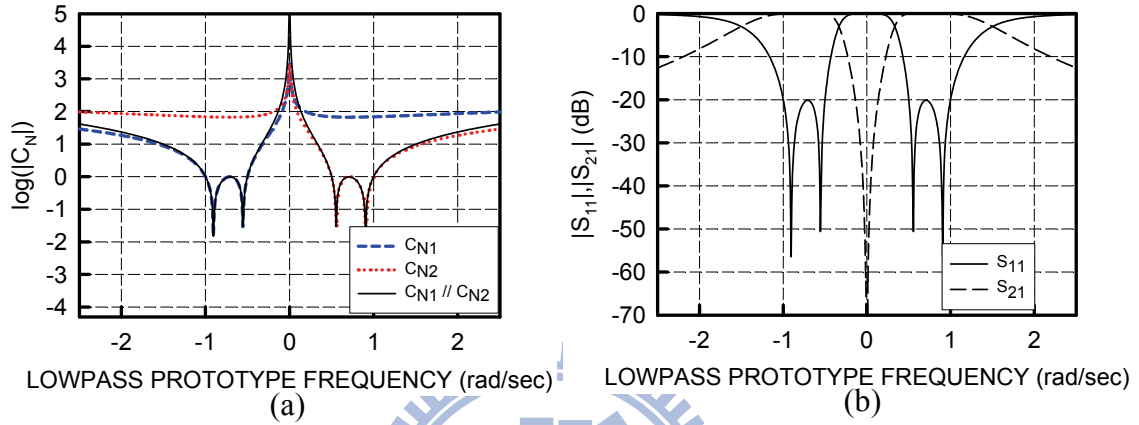
Figure 3-1 (a) Filtering functions for two single-band filters of degree 2 (C_{N1} has the transmission zero at 0 rad/s and the central frequency at -0.75 ras/s with the multi-band lowpass domain bandwidth δ_1 of 0.5 rad/s, and C_{N2} has the transmission zero at 0 rad/s and the central frequency at 0.75 rad/s with the multi-band lowpass domain bandwidth δ_2 of 0.5 rad/s), and the composite dual-band filter (C_{N1} // C_{N2}). The in-band return loss is 20 dB in each case. (b) The corresponding S_{11} and S_{21} for the dual-band filter.

Table 3.1 The Transversal Coupling Matrix for the Dual-band Filter in Figure 3-1.

	S	1	2	3	4	L
S	0.0	0.5315	-0.3046	0.3046	-0.5315	0.0
1	0.5315	1.2338	0.0	0.0	0.0	0.5315
2	-0.3046	0.0	0.4053	0.0	0.0	0.3046
3	0.3046	0.0	0.0	-0.4053	0.0	0.3046
4	-0.5315	0.0	0.0	0.0	-1.2338	0.5315
L	0.0	0.5315	0.3046	0.3046	0.5315	0.0

Table 3.2 The Coupling Matrix for the Dual-band Filter in Figure 3-1 with Coupling Scheme in Figure 3-2.

	S	1	2	3	4	L
S	0.0	0.5624	0.0	0.6590	0.0	0.0
1	0.5624	0.0	0.4590	0.0	0.0	0.0
2	0.0	0.4590	0.0	0.5379	0.0	0.0
3	0.6590	0.0	0.5379	0.0	1.0893	0.0
4	0.0	0.0	0.0	1.0893	0.0	0.8663
L	0.0	0.0	0.0	0.0	0.8663	0.0
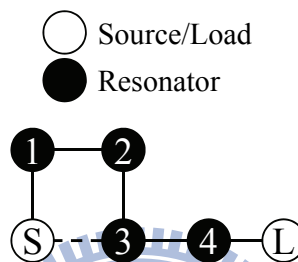
Figure 3-2 The single-path coupling scheme for the dual-band filter in Figure 3-1.

The single-path coupling scheme, however, is not always can be analyzed systematically using the information of transmission zeros. In most cases, the cross-coupling path needs to be run-and-try, and it even has no proper topology while the positions of transmission zeros are asymmetric to the passbands.

3.3 Dual-path Coupling Scheme

For the dual-band filter design, the single-path coupling scheme do not have an obvious relationship with the dual-band filter characteristics. To relate each passband with the coupling topology, the dual-path coupling scheme is considered. For example, there are two filtering functions; one is the 3rd order filtering function, which has the normalized transmission zero at -1.8 rad/s and the normalized central frequency at -0.8 rad/s with the

multi-band lowpass domain bandwidth δ_1 of 0.4 rad/s, while the other is the 3rd order

filtering function, which has the normalized transmission zeros at 1.8 rad/s and the

normalized central frequency at 0.8 rad/s with the multi-band lowpass domain bandwidth

δ_2 of 0.4 rad/s. The synthesized filtering functions and the corresponding S-parameters are

shown in Figure 3-3. The transversal coupling matrix in this example is listed in Table 3.3.

The transmission zero for the separation of two passbands is created as demonstrated

in the discussion in Section 2.4.1. In this case there are three finite transmission zeros

within the entire normalized low-pass domain there are -1.8, 0, and 1.8 rad/s. To illustrate

the dual-band characteristic and let each path govern one passband, the trisection portion of

each path is used to provide one transmission zero on the stopband. Figure 3-4 shows the

coupling scheme, and the corresponding coupling matrix is rotated by following steps [4].

The values of diagonal elements of the transversal matrix are categorized into two groups,

which are positive values and negative values, and then the original matrix can be

separated into two parts with values shown in Table 3.4. Based on these two sub-matrices,

the rotation sequence in Table 3.5 are applied and then the matrix for the coupling scheme

shown in Figure 3-4 are extracted with values listed in Table 3.6.
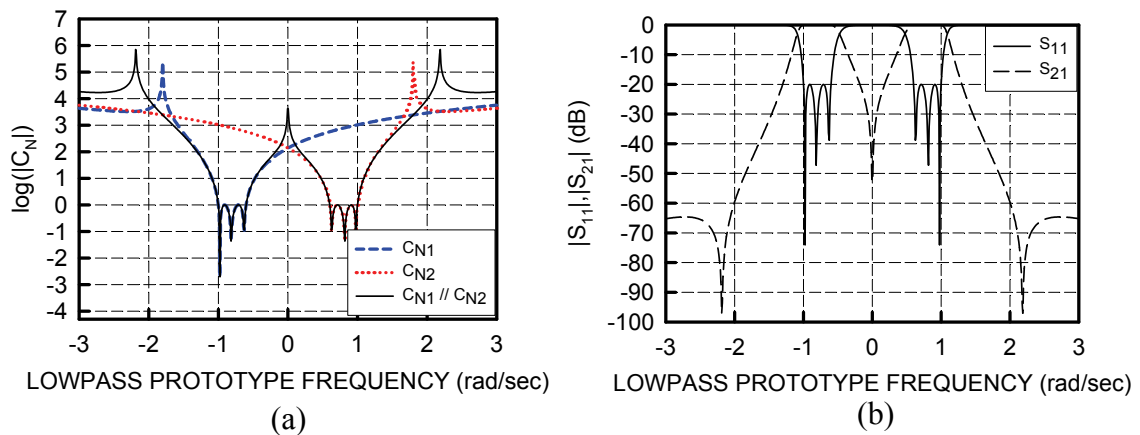
Figure 3-3 (a) Filtering functions for two single-band filters of degree 3 (C_{N1} has the
transmission zero at -1.8 rad/s and the central frequency at -0.8 rad/s with the multi-band
lowpass domain bandwidth δ_1 of 0.4 rad/s, and C_{N2} has the transmission zero at 1.8 rad/s

and the central frequency at 0.8 rad/s with the multi-band lowpass domain bandwidth δ_2 of 0.4 rad/s), and the composite filter (C_{N1} // C_{N2}). The in-band return loss is 20 dB in each case. (b) The corresponding S_{11} and S_{21} for the dual-band filter.

Table 3.3 The Transversal Coupling Matrix for the Dual-band Filter in Figure 3-3

	S	1	2	3	4	5	6	L
S	0.0	0.2295	-0.3419	0.2534	0.2534	-0.3419	0.2295	0.0
1	0.2295	1.0975	0.0	0.0	0.0	0.0	0.0	0.2295
2	-0.3419	0.0	0.8653	0.0	0.0	0.0	0.0	0.3419
3	0.2534	0.0	0.0	0.5272	0.0	0.0	0.0	0.2534
4	0.2534	0.0	0.0	0.0	-0.5272	0.0	0.0	0.2534
5	-0.3419	0.0	0.0	0.0	0.0	-0.8653	0.0	0.3419
6	0.2295	0.0	0.0	0.0	0.0	0.0	-1.0975	0.2295
L	0.0	0.2295	0.3419	0.2534	0.2534	0.3419	0.2295	0.0
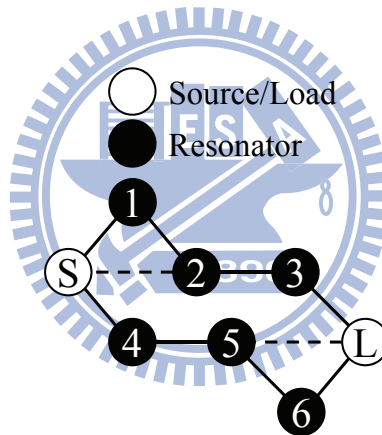
Figure 3-4 The dual-path coupling scheme for the dual-band filter in Figure 3-3.

Table 3.4 (a) The Transversal Coupling Matrix for the Upper Path (M1).
(b) The Transversal Coupling Matrix for the Lower Path (M2).

	S	1	2	3	L
S	0.0	0.2295	-0.3419	0.2534	0.0
1	0.2295	1.0975	0.0	0.0	0.2295
2	-0.3419	0.0	0.8653	0.0	0.3419
3	0.2534	0.0	0.0	0.5272	0.2534
L	0.0	0.2295	0.3419	0.2534	0.0

(a)

	S	4	5	6	L
S	0.0	0.2534	-0.3419	0.2295	0.0
4	0.2534	-0.5272	0.0	0.0	0.2534
5	-0.3419	0.0	-0.8653	0.0	0.3419
6	0.2295	0.0	0.0	-1.0975	0.2295
L	0.0	0.2534	0.3419	0.2295	0.0

(b)

Table 3.5 Rotation Sequence for Reduction of the Transversal Matrix to the Requested
Matrix with Topology in Figure 3-4

Transform Number t	Element to be Annihilated	Pivot [i, j]	$\theta_r = -\tan^{-1}(cM_{kl}/M_{mn})$				
			k	l	m	n	c
M1							
1	$M1_{S3}$	In row 1	[2, 3]	S	3	S	2	-1
2	$M1_{S2}$	---	[1, 2]	S	2	S	1	-1
3	$M1_{24}$	In column 4	[2, 3]	2	4	3	4	+1
4	$M1_{13}$	In column 3	[1, 2]	1	3	2	3	+1
M2							
1	$M2_{S5}$	In row 1	[4, 5]	S	5	S	4	-1
2	$M2_{S6}$	---	[4, 6]	S	6	S	4	-1
3	$M2_{46}$	In row 2	[5, 6]	4	6	4	5	-1

Table 3.6 The Coupling Matrix for the Dual-band Filter in Figure 3-3
with the Dual-path Coupling Scheme shown in Figure 3-4.

	S	1	2	3	4	5	6	L
S	0.0	0.4739	-0.0958	0.0	0.4835	0.0	0..0	0.0
1	0.4739	0.9033	0.1880	0.0	0.0	0.0	0.0	0.0
2	-0.0958	0.1880	0.8653	0.2047	0.0	0.0	0.0	0.0
3	0.0	0.0	0.2047	0.8247	0.0	0.0	0.0	0.4835
4	0.4835	0.0	0.0	0.0	-0.8247	0.2047	0.0	0.0
5	0.0	0.0	0.0	0.0	0.2047	-0.7619	0.1880	0.0958
6	0.0	0.0	0.0	0.0	0.0	0.1880	-0.9033	0.4739
L	0.0	0.0	0.0	0.4835	0.0	0.0958	0.4739	0.0

It can be noted that the values of diagonal elements in the extracted matrix are also categorized into two groups, which are positive values and negative values, and corresponds to the resonant frequency of each resonator. Hence, the upper path governs the lower passband, and the trisection portion of the upper path provides a transmission zero on the lower stopband (i.e., -1.8 rad/s). Similarly, the lower path governs the upper

passband and the trisection portion of the lower path generates a transmission zero on the upper stopband (i.e., 1.8 rad/s). By using such a dual-path coupling scheme, the transmission zeros on the upper and lower stopband can be generated by the trisection portion, while the additional transmission zero used to separate two passbands is generated by out-of-phase property of C_{N1} and C_{N2}.

3.4 Transmission Zeros Determination in Single-path and Dual-path Coupling Schemes

The coupling matrix is related to the responses of reflection and transfer function S_{11} and S_{21} via the following equations [46]:

$$S_{11} = 1 + 2j\left[\mathbf{A}^{-1}\right]_{1,1}, \quad S_{21} = -2j\left[\mathbf{A}^{-1}\right]_{N+2,1},$$
$$\mathbf{A} = \Omega\left[\mathbf{U}_0\right] + \left[\mathbf{M}\right] - j\left[\mathbf{R}\right],$$
(3-1)

where N is the order of filter, Ω is the angular frequency in the low-pass domain, $[\mathbf{U}_0]$ is similar to the (N+2)-by-(N+2) identity matrix except $[\mathbf{U}_0]_{1,1} = [\mathbf{U}_0]_{N+2, N+2} = 0$, $[\mathbf{M}]$ is the (N+2)-by-(N+2) coupling matrix, and $[\mathbf{R}]$ is the diagonal matrix with $[\mathbf{R}] = \mathrm{diag}\{1,0,\ldots,0, 1\}$.

To determine the locations of transmission zeros from the coupling matrix in arbitrary coupling topology, it is equivalent to find the roots of S_{21}. In order to find the roots of $[\mathbf{A}^{-1}]_{N+2,1}$, the technique in [136] is used,

$$\left[\mathbf{A}^{-1} \right]_{N+2,1} = \frac{\mathrm{cofactor}(\mathbf{A}_{1,N+2})}{\mathrm{Det}(\mathbf{A})}. \tag{3-2}$$

Hence the transmission zeros are consequently the zeros of the cofactor of $[\mathbf{A}]_{1,N+2}$. Now we present three examples of dual-band filters with single-path and dual-path coupling schemes, and show the mechanism in introducing transmission zeros under signle-path and dual-path topology.

3.4.1 Single-path Dual-band Filter Characteristic

In the first example, the dual-band filter consists of two 4th order filters with central frequency at -0.75 and 0.75 rad/s and transmission zeros at ±0.1118, ±1.3126, and ±j12.2234 rad/s, which j is the imaginary number. The multi-band lowpass domain bandwidth δ for both passband is 0.5 rad/s. The corresponding coupling matrix is listed in Table 3.7 and the performance is shown in Figure 3-5.

Table 3.7 The Coupling Matrix of the Single-path Dual-band Filter

	S	1	2	3	4	5	6	7	8	L
S	0.0	0.6849	0.0	-0.2442	0.0	0.0	0.0	0.0	0.0	0.0
1	0.6849	0.0	0.9474	0.0	0.0	0.0	0.0	0.0	0.0	0.0
2	0.0	0.9474	0.0	0.3120	0.0	0.0	0.0	0.0	0.0	0.0
3	-0.2442	0.0	0.3120	0.0	0.6952	0.0	0.0	0.0	0.0	0.0
4	0.0	0.0	0.0	0.6952	0.0	0.3670	0.0	0.0	0.0	0.0
5	0.0	0.0	0.0	0.0	0.3670	0.0	0.8023	0.0	0.0	0.0
6	0.0	0.0	0.0	0.0	0.0	0.8023	0.0	0.3811	0.0	0.4198
7	0.0	0.0	0.0	0.0	0.0	0.0	0.3811	0.0	0.5614	0.0
8	0.0	0.0	0.0	0.0	0.0	0.0	0.0	0.5614	0.0	0.5937
L	0.0	0.0	0.0	0.0	0.0	0.0	0.4198	0.0	0.5937	0.0

Figure 3-5 The performance of the single-path dual-band filter and the corresponding dual-path coupling scheme based on the coupling matrix in Table 3.7.

To understand the mechanism of the transmission zeros. Here the cross coupling paths are removed to see and estimate the transmission zeros. In Figure 3-6 (a), the cross coupling path S-3 is removed, then the outer transmission zeros are disappeared; while removing the path 6-L, the inner transmission zeros will be disappeared, as shown in Figure 3-6 (b). Applying (3-2) to evaluate the transmission zeros, the formulation is as follows:

$$
\begin{vmatrix}
M_{S1} & \Omega & M_{12} \\
 & M_{12} & \Omega & M_{23} \\
M_{S3} & & M_{23} & \Omega & M_{34} \\
 & & & M_{34} & \Omega & M_{45} \\
 & & & & M_{45} & \Omega & M_{56} \\
 & & & & & M_{56} & \Omega & M_{67} \\
 & & & & & & M_{67} & \Omega & M_{78} \\
 & & & & & & & M_{78} & \Omega \\
 & & & & & M_{6L} & & & M_{8L}
\end{vmatrix} = 0
$$

$$
\Rightarrow -M_{34}M_{45}M_{56}(-M_{12}M_{23}M_{S1} + M_{12}^2 M_{S3} - M_{S3}\Omega^2)(M_{67}M_{78}M_{8L} + M_{6L}(-M_{78}^2 + \Omega^2))=0 \qquad (3\text{-}3)
$$

$$
\Rightarrow
\begin{cases}
\Omega_1^2 = M_{12}^2 - \dfrac{M_{12}M_{23}M_{S1}}{M_{S3}}, \\[3mm]
\Omega_2^2 = M_{78}^2 - \dfrac{M_{67}M_{78}M_{8L}}{M_{6L}},
\end{cases}
$$

From the above solutions, if the matrix is symmetric, then the transmission zeros are symmetric to 0 rad/s. While removing path S-3 (i.e., $M_{S,3} = 0$), the transmission zeros of ±1.3126 rad/s are disappeared, and transmission zeros ±0.1118 rad/s will be disappeared when the path 6-L is removed.

Figure 3-6 The performances for the single-path dual-band filter with removing of cross couplings (a) removing path S-3 and (b) removing path 6-L.

3.4.2 Symmetric Dual-path Dual-band Filter Characteristic

In the second example, the dual-band filter consists of two 4th order filters with central frequencies at -0.75 and 0.75 rad/s in two passbands, and transmission zeros at ±0.1078, ±1.4657, and ±j0.9613 rad/s. The corresponding coupling matrix is listed in Table 3.8.

It is worthy to be noted that the diagonal terms of the coupling matrix are classified into two groups to present the central frequencies of two passbands, i.e., resonators numbered from 1 to 4 (passband with central frequency 0.75 rad/s), and resonators numbered from 5 to 8 (passband with central frequency -0.75 rad/s). The corresponding performance is shown in Figure 3-7, and the dual-path coupling scheme is shown in the subplot. For the dual-path topology, each path has a cross-coupled quadruplet, so that there are two transmission zeros symmetric to the central frequency of each passband. Once the cross couplings of these quadruplets are removed, the transmission zeros vanish, and it can be observed by the dashed line in Figure 3-7.

Table 3.8 The Coupling Matrix of the Symmetric Dual-path Dual-band Filter

	S	1	2	3	4	5	6	7	8	L
S	0.0	0.5110	0.0	-0.0433	0.0	0.5128	0.0	0..0	0.0	0.0
1	0.5110	-0.7914	0.2328	0.0	0.0	0.0	0.0	0.0	0.0	0.0
2	0.0	0.2328	-0.7405	0.1622	0.0	0.0	0.0	0.0	0.0	0.0
3	-0.0433	0.0	0.1622	-0.7464	0.2191	0.0	0.0	0.0	0.0	0.0
4	0.0	0.0	0.0	0.2191	-0.7911	0.0	0.0	0.0	0.0	0.5128
5	0.5128	0.0	0.0	0.0	0.0	0.7911	0.2191	0.0	0.0	0.0
6	0.0	0.0	0.0	0.0	0.0	0.2191	0.7464	0.1622	0.0	-0.0433
7	0.0	0.0	0.0	0.0	0.0	0.0	0.1622	0.7405	0.2328	0.0
8	0.0	0.0	0.0	0.0	0.0	0.0	0.0	0.2328	0.7914	0.5110
L	0.0	0.0	0.0	0.0	0.5128	0.0	-0.0433	0.0	0.5110	0.0

Due to the frequency-separated property, the mechanism of generation of corresponding transmission zeros can be observed in each passband. In Figure 3-8 (a), the quadruplet cross-coupling within the upper path introduces two transmission zeros

symmetric to the central frequency at 0.75 rad/s, which is the resonant frequency of resonators numbered from 1 to 4. Similarly the cross-coupled quadruplet within the lower path provided two zeros symmetrical to -0.75 rad/s, as shown in Figure 3-8 (b). Once the quadruplet cross coupling is removed from each path, the transmission zeros vanish. Furthermore, to identify the locations of transmission zeros in each path, (3-2) is applied to the following matrices $[\mathbf{A}]^{up}$ and $[\mathbf{A}]^{low}$:

$$
[\mathbf{A}]^{up} = \begin{bmatrix}
-j & M_{S,1} & 0 & M_{S,3} & 0 & 0 \\
M_{S,1} & \Omega + M_{1,1} & M_{1,2} & 0 & 0 & 0 \\
0 & M_{1,2} & \Omega + M_{2,2} & M_{2,3} & 0 & 0 \\
M_{S,3} & 0 & M_{2,3} & \Omega + M_{3,3} & M_{3,4} & 0 \\
0 & 0 & 0 & M_{3,4} & \Omega + M_{4,4} & M_{4,L} \\
0 & 0 & 0 & 0 & M_{4,L} & -j
\end{bmatrix},
\tag{3-4}
$$

$$
[\mathbf{A}]^{low} = \begin{bmatrix}
-j & M_{S,5} & 0 & 0 & 0 & 0 \\
M_{S,5} & \Omega + M_{5,5} & M_{5,6} & 0 & 0 & 0 \\
0 & M_{5,6} & \Omega + M_{6,6} & M_{6,7} & 0 & M_{6,L} \\
0 & 0 & M_{6,7} & \Omega + M_{7,7} & M_{7,8} & 0 \\
0 & 0 & 0 & M_{7,8} & \Omega + M_{8,8} & M_{8,L} \\
0 & 0 & M_{6,L} & 0 & M_{8,L} & -j
\end{bmatrix},
\tag{3-5}
$$

where $[\mathbf{A}]^{up}$ is the matrix of the upper path and $[\mathbf{A}]^{low}$ is the matrix of the lower path.

Consequently, the transmission zeros are 1.4897 and 0.0536 rad/s of the upper path, and they are -1.4897 and -0.0536 rad/s of the lower path. Moreover, it is noted that the transmission zeros can be obtained similarly in the dual-path topology without cross-coupled quadruplets, and they are $\pm j1.8360$ and $\pm j0.2883$ rad/s. It means even no cross-coupled quadruplet, dual-path topology also provides complex transmission zeros, so that the inherent separation between two adjacent passbands exists, as shown in Figure 3-7.
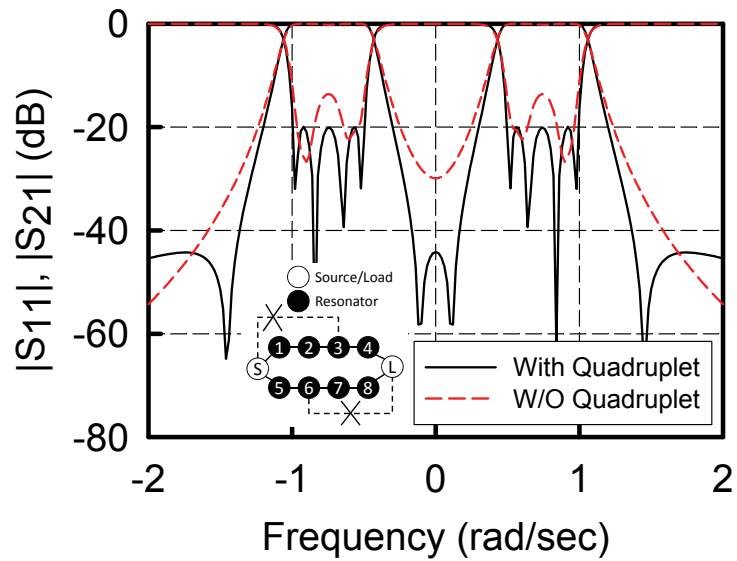
Figure 3-7 The performance of the symmetric dual-band filter and the corresponding dual-path coupling scheme based on the coupling matrix in Table 3.8.
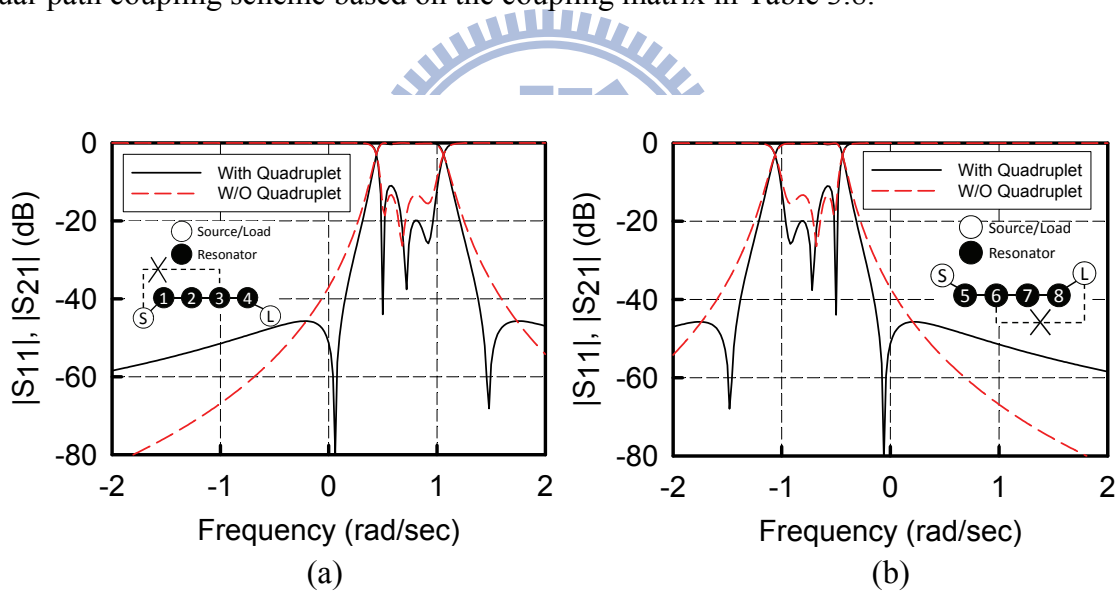
Figure 3-8 The performances of the (a) upper path and (b) lower path in the symmetric dual-band filter.

3.4.2 Asymmetric Dual-path Dual-band Characteristic

In the third example, the asymmetric dual-path dual-band filter consists of a 3rd and a 4th order filters with central frequencies at 0.7778 and -0.7778 rad/s in the lowpass domain with the multi-band lowpass domain bandwidth δ of 0.4444 rad/s for both passbands. It

contains six transmission zeros, which are -1.4305, -0.2078, 0.0948, 1.4802, and -0.7663 ±

j0.5029 rad/s. The corresponding coupling matrix is listed in Table 3.9.

In Figure 3-9, one group of resonators, namely resonators 1 to 3, governs the central

frequency at 0.7778 rad/s, while the other group of resonators 4 to 7 governs the central

frequency at -0.7778 rad/s. The value of entry $M_{5,L}$, however is small enough to be ignored

without influence on the dual-band characteristic.

Table 3.9 The Coupling Matrix of the Asymmetric Dual-band Filter.

	S	1	2	3	4	5	6	7	L
S	0.0	0.5005	0.0	-0.0597	0.4902	0.0	0.0	0..0	0.0
1	0.5005	-0.8187	0.2353	0.0	0.0	0.0	0.0	0.0	0.0
2	0.0	0.2353	-0.7752	0.2086	0.0	0.0	0.0	0.0	0.0
3	-0.0597	0.0	0.2086	-0.8179	0.0	0.0	0.0	0.0	0.5033
4	0.4902	0.0	0.0	0.0	0.8164	0.2002	0.0	0.0	0.0
5	0.0	0.0	0.0	0.0	0.2002	0.7782	0.1572	0.0	0.0
6	0.0	0.0	0.0	0.0	0.0	0.1572	0.7786	0.1983	0.0
7	0.0	0.0	0.0	0.0	0.0	0.0	0.1983	0.8165	0.4876
L	0.0	0.0	0.0	0.5033	0.0	0.0	0.0	0.4876	0.0

It is worthy to be noted that one quadruplet cross coupling introduces four

transmission zeros. To make clear the mechanism in generating of transmission zeros, the

analysis is applied as followings. Figure 3-10 (a) shows the performance in the upper path,

and it is obvious that the transmission zeros come from the quadruplet cross coupling, To

identify the transmission zeros of the lower path, the cross-coupled path is retained. This

extra path consists of the quadruplet cross coupling within the upper path and the resonator

3, which is shown in the subplot of Figure 3-10 (b). Moreover, the transmission zeros can

be determined via (3-2), and they are 0.1133 and 1.4806 rad/s of the upper path, while

-0.2613, -1.4191, and -0.7546 ± j0.4837 rad/s of the lower path. Furthermore, even no

cross coupling, the dual-path topology inherently maintains the isolation between two
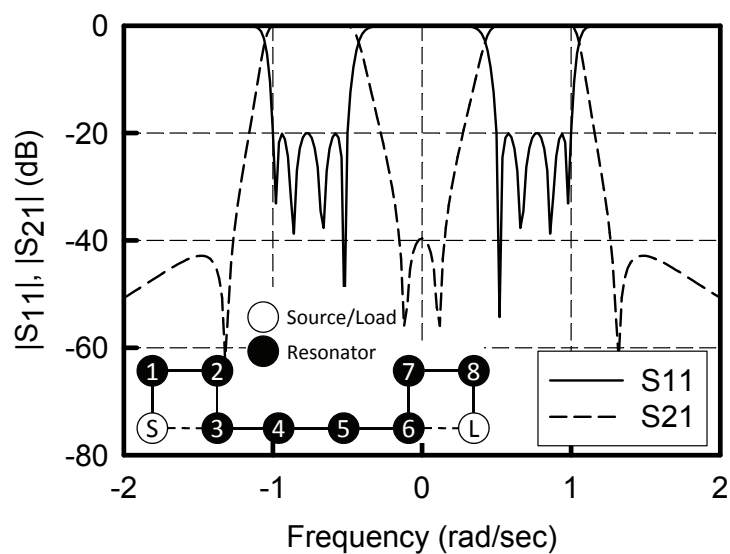
passbands, as shown in Figure 3-9.
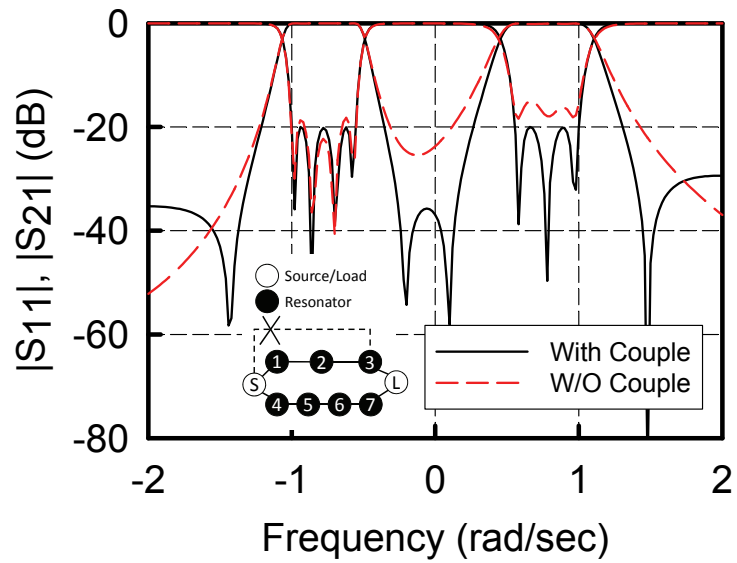
Figure 3-9 The performance of the asymmetric dual-band filter and the corresponding dual-path coupling scheme based on the coupling matrix in Table 3.9.
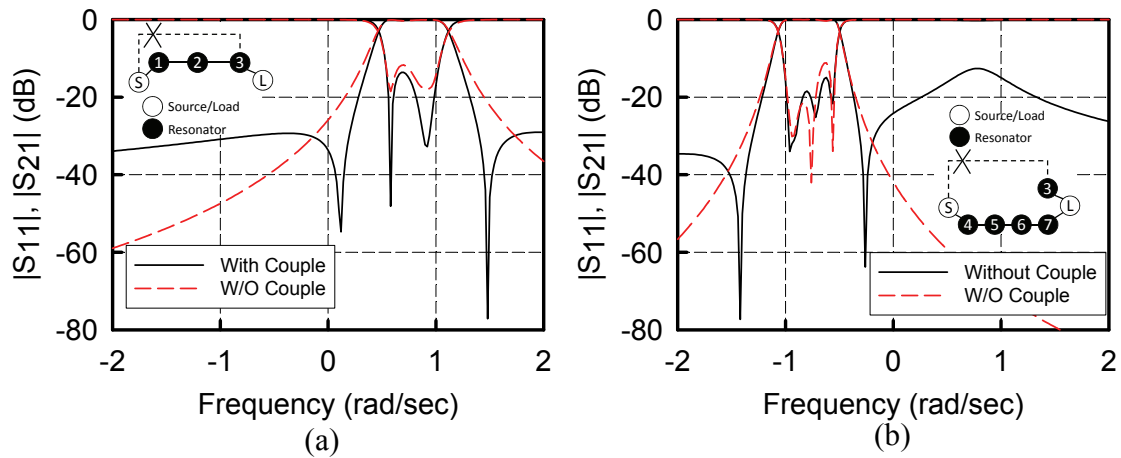
Figure 3-10 The performances of the (a) upper path and (b) lower path in the asymmetric dual-band filter.

3.5 Analytical Approach for Dual-band Filter Design Using Parallel-Coupled Lines

The previous section shows the specific coupling scheme for the microstrip implementation. Here the relations between the coupling coefficients and the parameters of the microstrip lines are discussed. To introduce the slope parameter of the resonator, the value of Js of the parallel-coupled line model can be obtained using the following equations [137]:

$$
\begin{aligned}
J_{0,1} &= M_{S,1}\sqrt{\Delta b_1 / Z_0}, \\
J_{j,j+1} &= M_{j,j+1}\Delta\sqrt{b_j b_{j+1}}, \quad j = 1,\cdots,n-1, \\
J_{n,n} &= M_{n,L}\sqrt{\Delta b_n / Z_0},
\end{aligned}
\tag{3-6}
$$

where Δ is the fractional bandwidth. Once the values of J inverters are obtained, the even- and odd-mode characteristic impedance for non-quarter-wavelength parallel-coupled line [138] can be calculated by

$$
\begin{aligned}
\frac{Z_{oe}}{Z_0} &= \frac{1+(JZ_0)\cos\theta+(JZ_0)^2}{1-(JZ_0)^2\cot^2\theta}, \\
\frac{Z_{oo}}{Z_0} &= \frac{1-(JZ_0)\cos\theta+(JZ_0)^2}{1-(JZ_0)^2\cot^2\theta}.
\end{aligned}
\tag{3-7}
$$

Based on (3-6) and (3-7), the parameters of the microstrip parallel-coupled lines can be obtained. Here an example for the dual-band filter is provided to show the validation. The filter design for the dual-band GPS at 1227 MHz and 1575 MHz is used to show the closely adjacent passbands. In the design, each passband has 10% fractional bandwidth.

Use (2-13), the central frequency of the dual-band filter is 1390 MHz with fractional bandwidth 35%. To transfer the information into the lowpass domain, the passband #1 has the normalized central frequency at -0.713 rad/s and the passband # 2 has the normalized central frequency at 0.713 rad/s. Both filter orders are 3 and the return loss are 15 dB. The dual-path coupling scheme is used in this example, as shown in Figure 3-11. The corresponding performance is shown in Figure 3-11 and the coupling scheme is listed in Table 3.10.
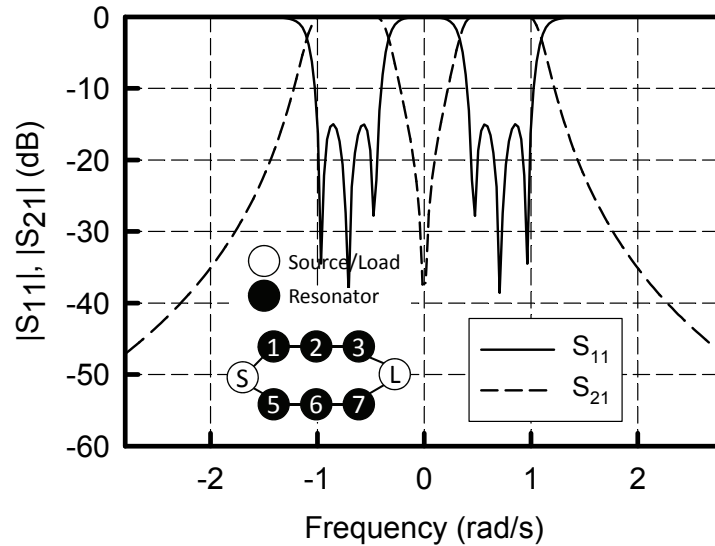
Figure 3-11 The performance and coupling scheme of the dual-band filter design for GPS system.

Table 3.10 The Coupling Matrix of the Dual-band Filter for GPS System Design.

	S	1	2	3	4	5	6	L
S	0.0	0.5054	0.0	0.0	0.5053	0.0	0.0	0.0
1	0.5054	-0.7588	0.2490	0.0	0.0	0.0	0.0	0.0
2	0.0	0.2490	-0.7152	0.2490	0.0	0.0	0.0	0.0
3	0.0	0.0	0.2490	-0.7588	0.0	0.0	0.0	0.5054
4	0.5053	0.0	0.0	0.0	0.7587	0.2491	0.0	0.0
5	0.0	0.0	0.0	0.0	0.2491	0.7153	0.2491	0.0
6	0.0	0.0	0.0	0.0	0.0	0.2491	0.7587	0.5053
L	0.0	0.0	0.0	0.5054	0.0	0.0	0.5053	0.0

Based on the coupling matrix, now the parameters of the parallel-coupled lines can be obtained in (3-6) and (3-7). Let f_1 = 1575 MHz and f_2 = 1227 MHz. For the microstrip implementation of the upper path of the dual-path coupling scheme, the schematic is shown in Figure 3-12. For the passband at f_1, the corresponding path is S-1-2-3-L. Choosing $\theta_{S1} = \theta_{12} = \theta_{23} = \theta_{3L} = \theta_1 = \theta_2 = \theta_3 = 60^\circ$ (i.e., the length of each resonator is 180°, so that the slope parameter $b = \pi/2/Z_0$), the calculated parameters of the parallel-coupled lines are listed in Table 3.11. The similar procedure is applied to the lower path, and the schematic is shown in Figure 3-13 and parameters are listed in Table 3.12. In Table 3.10, the asymmetric property of the passband comes from the different diagonal terms, so that the length of the coupled line should be slightly tuned.
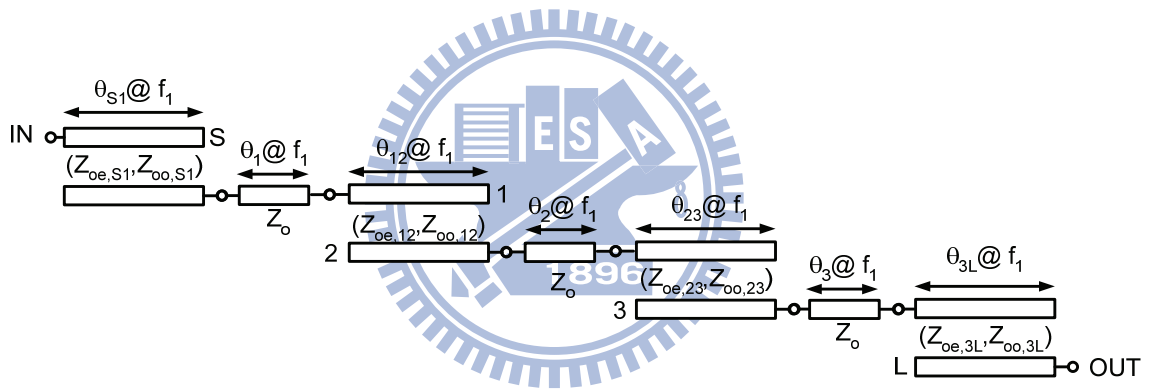
Figure 3-12 The schematic of the parallel-coupled line for the upper path of the dual-path coupling scheme.

Table 3.11 The Calculated Parameters for the Parallel-Coupled Line of the Upper Path.

	f_1 = 1575 MHz			
	M_{S1}	M_{12}	M_{23}	M_{3L}
J	0.0075	0.0014	0.0014	0.0075
Z_{oe} (Ω)	82.5198	57.8927	57.8927	82.5198
Z_{oo} (Ω)	37.1236	40.0080	40.0080	37.1236
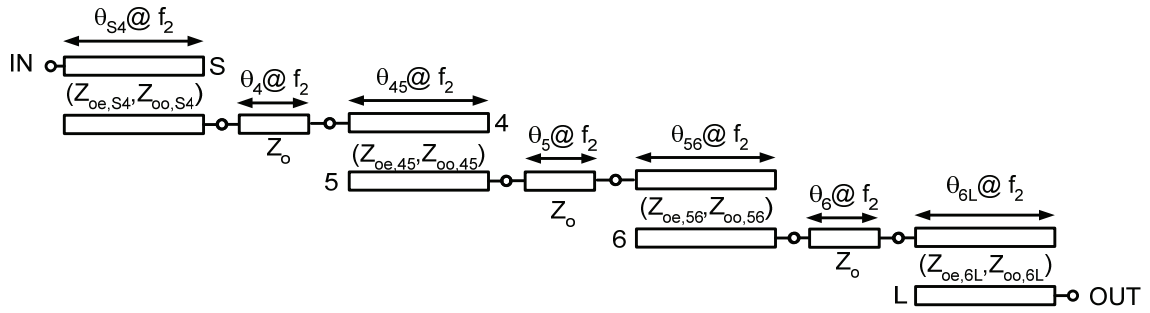
Figure 3-13 The schematic of the parallel-coupled line for the upper path of the dual-path coupling scheme.

Table 3.12 The Calculated Parameters for the Parallel-Coupled Line of the Lower Path.

$f_2 = 1227$ MHz				
	M_{S4}	M_{45}	M_{56}	M_{6L}
J	0.0075	0.0014	0.0014	0.0075
Z_{oe} (Ω)	82.5108	57.8963	57.8963	82.5108
Z_{oo} (Ω)	37.1245	40.0060	40.0060	37.1245
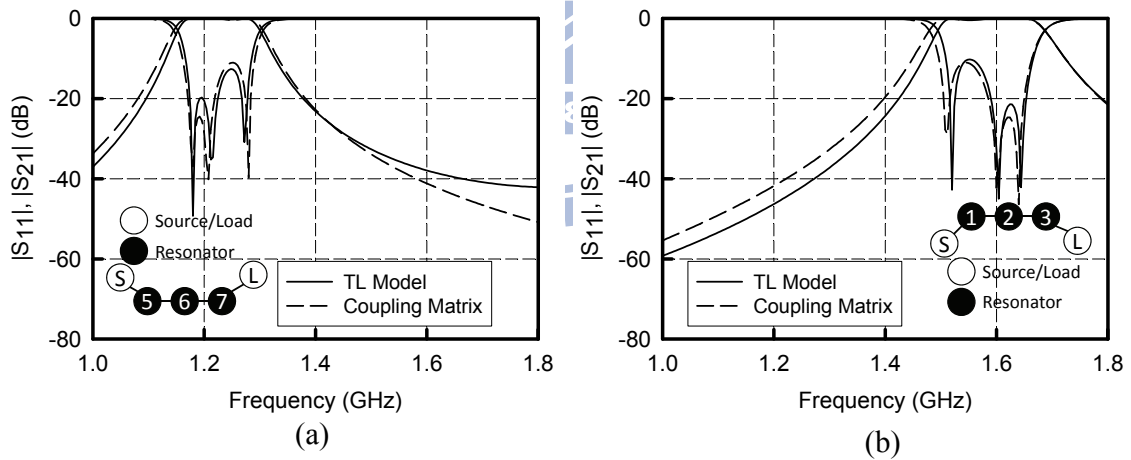
Figure 3-14 The performances for the parallel-coupled line model and coupling matrix of lower and upper paths.

Table 3.13 The Tuned Lengths of the Parallel-Coupled Line in Figure 3-12 and Figure 3-13

$f_1 = 1575$ MHz		$f_2 = 1227$ MHz	
θ_{S1}	55°	θ_{S4}	57°

θ_{12}	65°	θ_{45}	65°
θ_{23}	65°	θ_{56}	65°
θ_{3L}	55°	θ_{6L}	57°
θ_1	58°	θ_4	59°
θ_2	49°	θ_5	50°
θ_3	58°	θ_6	59°

After tuning the lengths, the performances for the upper and lower path are shown in Figure 3-14 with the tuned lengths listed in Table 3.13. To combine two filters into a dual-band filter, the double-diplexing configuration is used, as shown in Figure 3-15. The f_0 in the figure is the central frequency of the dual-band filter. In [132], the imaginary part of the input admittance for the path S-1-2-3-L (which is passband at f_1) is zero at f_2, while the imaginary part of the input admittance for the path S-4-5-6-L is zero at f_1. Applying this procedure to the dual-band filter for the GPS system and fine tuning the lengths of each filter, the final lengths are listed in Table 3.14. The performances are shown in Figure 3-16.
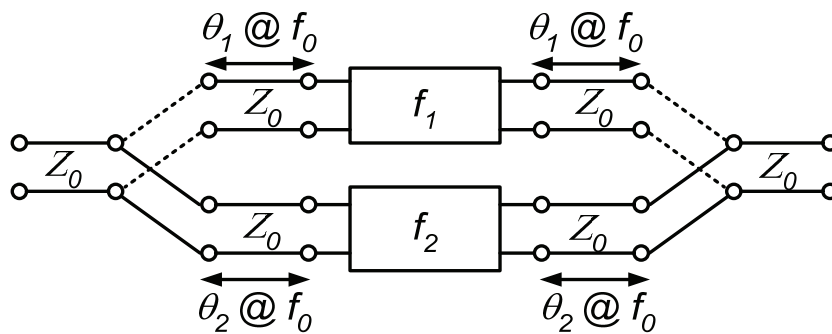
Figure 3-15 The double-diplexing configuration proposed by [132]

Table 3.14 The Final Lengths of the Dual-band Filter for GPS System.

f_1 = 1575 MHz		f_2 = 1227 MHz		f_0 = 1390 MHz	
θ_{S1}	58.5°	θ_{S4}	57.5°	θ_1	150°
θ_{12}	68°	θ_{45}	64°	θ_2	97°
θ_{23}	68°	θ_{56}	64°		
θ_{3L}	58.5°	θ_{6L}	57.5°		
θ_1	54°	θ_4	57.5°		
θ_2	45°	θ_5	50°		
θ_3	54°	θ_6	57.5°		

Figure 3-16 The bandpass performances of the dual-band filter for the GPS system.

3.6 Microstrip Implementation for Single-path and Dual-path Dual-band filters

The synthesis procedure has been illustrated completely. In this section, the microstrip

implementations for the filters described in the previous section will be used to demonstrate the validation of the proposed filter synthesis.

3.6.1 The Single-path Dual-band Filter

Table 3.2 lists the coupling matrix with the coupling scheme shown in Figure 3-2. The central frequencies of the two passbands in the practical design are 2.3 and 2.7 GHz, while the fractional bandwidth is 5% in each passband. For the practical implementation, a 0.508-mm-thick Rogers RO4003 substrate with a relative dielectric constant 3.58 and a loss tangent of 0.0021 is used. Based on the design procedure in [139] for choosing the length of the quadruplet cross-coupling, the layout of the proposed microstrip filter is shown in Figure 3-17. The dimensions are listed in Table 3.15.

In Table 3.2, the element of cross coupling $M_{S,3}$ is 0.6590, which is even larger than the direct couple $M_{S,1}$ (0.5624) along the main path. Hence the cross couple will be treated similarly as the direct coupled path between source and resonator 3. Such a strong cross-coupling strength $M_{S,3}$ contributes the separation of two passbands. In the practical design, the length of each coupled line section is initially set to be a quarter-wave length at 2.5 GHz. It is then simulated by ADS to obtain the final practical length.
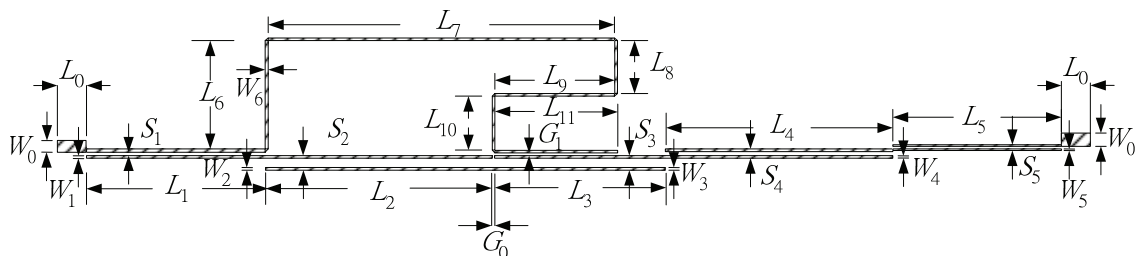
Figure 3-17 The circuit layout for the filter with the coupling matrix listed in Table 3.2

Table 3.15 Dimensions for the Layout Shown in Figure 3-17. (Unit: *mm*)

W_0	W_1	W_2	W_3	W_4	W_5	W_6	L_0
1.1180	0.2540	0.2540	0.2540	0.3302	0.2032	0.2032	2.5400
L_1	L_2	L_3	L_4	L_5	L_6	L_7	L_8
16.7400	20.8500	15.7700	21.0600	15.7200	10.1600	32.1300	4.9780
L_9	L_{10}	L_{11}	S_1	S_2	S_3	S_4	S_5
11.2300	5.0800	11.4300	0.2540	0.8382	0.8382	0.2540	0.2032
G_0	G_1						
0.2540	0.2032						
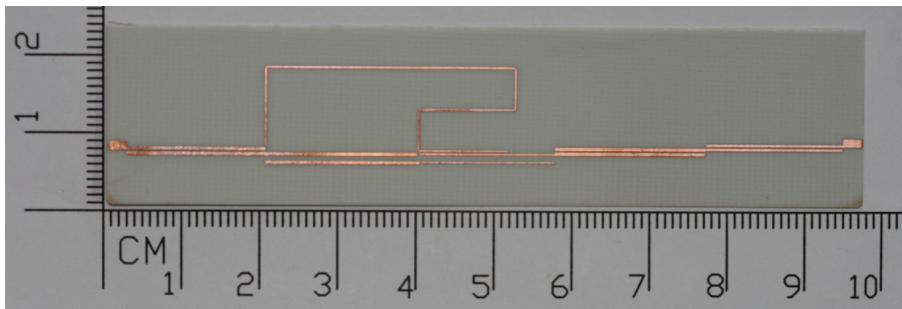
Figure 3-18 The practical microstrip implementation for the filter with the coupling matrix listed in Table 3.2
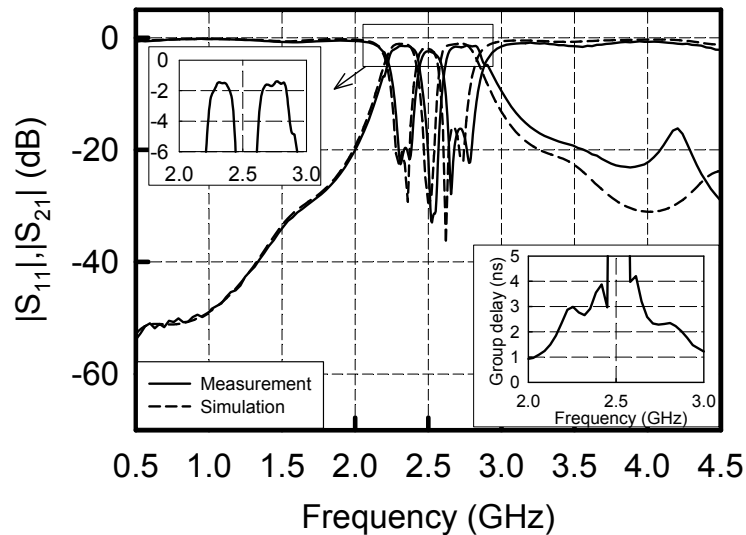
Figure 3-19 The responses for the single-path dual-band filter in Figure 3-18.

Figure 3-18 shows the photograph for the single-path dual-band filter and the measured S-parameters are shown in Figure 3-19. In the figure, the measured results agree

well with the simulated one.

3.6.2 The Symmetric Dual-path Dual-band Filter

Table 3.6 lists the coupling matrix with the coupling scheme shown in Figure 3-4. The central frequencies of the two passbands in the practical design are 2.2 and 2.7 GHz, while the fractional bandwidth is 5% in each passband. For the practical implementation, a 0.6350mm-thick Rogers RT/Duroid 6010 substrate, with a relative dielectric constant 10.2 and a loss tangent of 0.0021, is used to implement such a dual-band filter. The design parameters can be obtained using (3-6) and (3-7). The layout of the dual-band microstrip filter is shown in Figure 3-20 with the dimensions are listed in Table 3.16.

In this example, the transmission zeros within the stopbands are known to be governed by the trisection portion of coupling scheme $M_{S,2}$ and $M_{5,L}$ in Figure 3-4. The values of the corresponding elements are -0.0958 and 0.0958 in Table 3.6, which are smaller than the element value along the main path. This makes sense because the locations of transmission zeros are far from the corresponding passbands. In Figure 3-20, the lengths of the two coupling lines L_{16} (0.685 mm) and L_{20} (0.7112 mm) are obviously shorter than other coupled lines in the main path. The gaps G_1 and G_2 are also wider than the gaps of the main coupling path. Because of the dual-path schematic, a transmission zero to separate two passbands exists inherently. The dual-path coupling scheme also provides another advantage, which is the initial length of each coupled line that can be obtained at each resonant frequency due to each path governs one passband. After simulated by ADS, the final practical dimensions will be obtained.
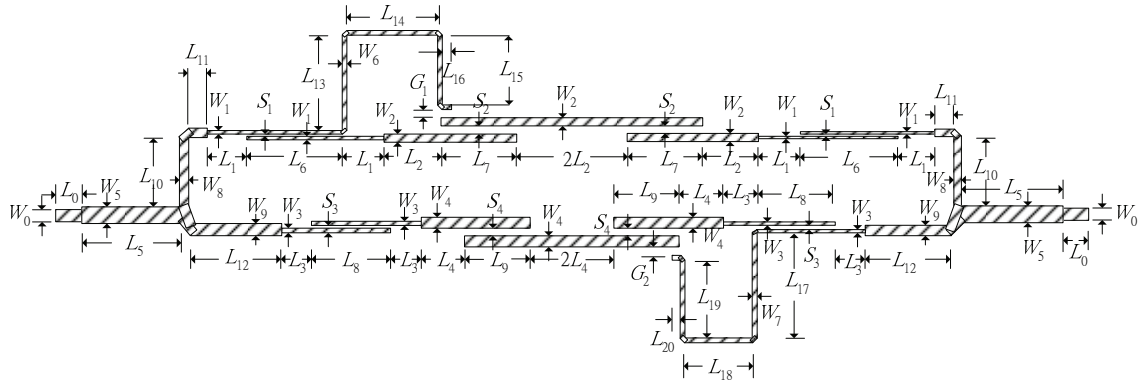
Figure 3-20 The layout for the dual-path dual-band filter with the coupling matrix listed in Table 3.6.

Table 3.16 Dimensions for the Layout Shown in Figure 3-20. (Unit: *mm*)

W_0	W_1	W_2	W_3	W_4	W_5	W_6	W_7
1.1180	0.2032	0.8636	0.4064	1.0160	1.1940	0.2286	0.2286
L_0	L_1	L_2	L_3	L_4	L_5	L_6	L_7
2.5400	3.9120	7.1120	2.9970	4.0130	9.2960	9.0420	7.1120
L_8	L_9	L_{10}	L_{11}	L_{12}	L_{13}	L_{14}	L_{15}
7.5180	6.0710	6.9090	1.6510	8.1030	9.3470	8.6870	6.9090
L_{16}	L_{17}	L_{18}	L_{19}	L_{20}	S_1	S_2	S_3
0.6850	10.5400	6.5530	8.0010	0.7112	0.2032	0.5080	0.2032
S_4	G_1	G_2					
0.5080	0.9144	1.0920					
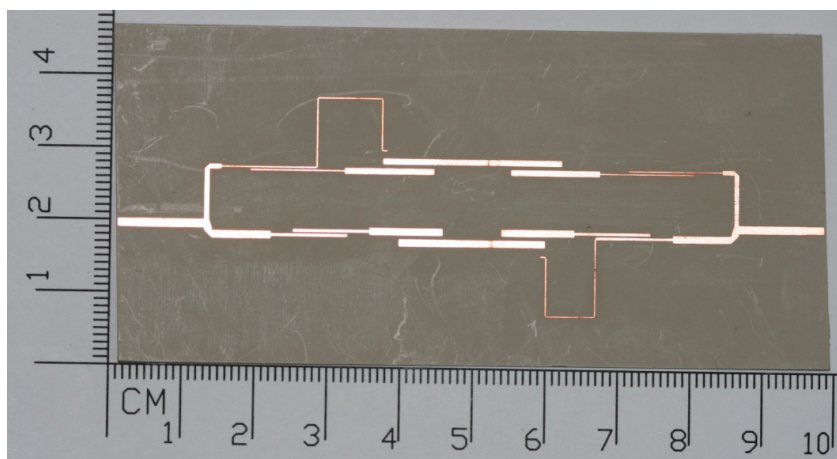
Figure 3-21 The photograph of implemented microstrip symmetric dual-band filter with the coupling matrix listed in Table 3.6.
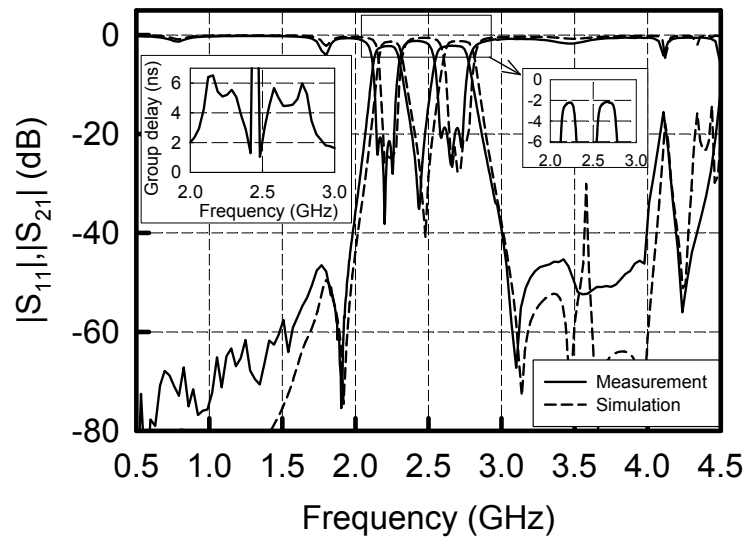
Figure 3-22 The responses for the symmetric dual-path dual-band filter in Figure 3-21.

Figure 3-21 shows the photograph for the symmetric dual-path dual-band filter and the measured S-parameters are shown in Figure 3-22. In the figure, the measured results agree well with the simulated one.

3.6.3 The Asymmetric Dual-path Dual-band Filter

Table 3.9 lists the coupling matrix with the coupling scheme shown in Figure 3-9. The central frequencies of the two passbands in the practical design are 2.26 and 2.7 GHz, while the fractional bandwidth is 5% in each passband. For the practical implementation, a 0.508-mm-thick Rogers RO4003 substrate, with a relative dielectric constant 3.58 and a loss tangent of 0.0021, is used to implement such a dual-band filter. The design parameters can be obtained using (3-6) and (3-7). The layout of the dual-band microstrip filter is shown in Figure 3-23 with the dimensions are listed in Table 3.17. The circuit photograph is shown in Figure 3-24 and Figure 3-25 shows the measured results, which agree well with the simulated performance.
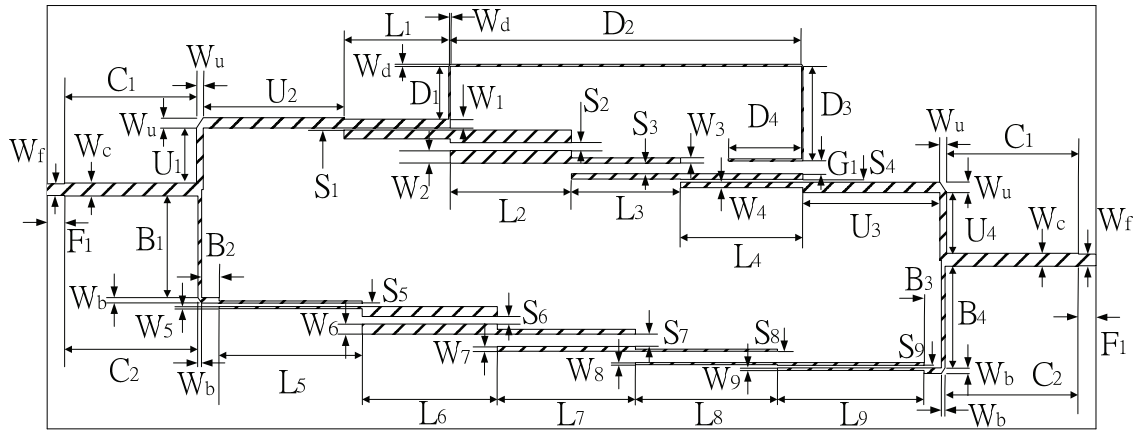
Figure 3-23 The layout for the asymmetric dual-path dual-band filter with the coupling matrix listed in Table 3.9.

Table 3.17 Dimensions for the Layout Shown in Figure 3-23. (Unit: *mm*)

W_1	W_2	W_3	W_4	W_5	W_6	W_7	W_8
1.2500	1.2500	0.9250	0.2000	0.6000	0.7000	0.2000	1.2500
W_9	W_{10}	L_1	L_2	L_3	L_4	L_5	L_6
0.6000	1.0250	20.0500	12.1000	19.6500	15.1000	18.6500	19.5000
L_7	L_8	L_9	L_{10}	S_1	S_2	S_3	S_4
20.1250	17.4750	19.9500	18.0250	0.2750	0.6500	1.2500	1.0750
S_5	S_6	S_7	S_8	S_9	S_{10}	W_d	D_1
0.2000	0.2000	1.2250	0.7500	1.1750	0.2000	0.2000	10.2250
D_2	D_3	D_4	D_5	D_6	D_7	D_8	G_1
46.6500	16.4500	0.7750	0.6000	12.5750	57.3500	6.5000	0.2250
G_2	W_a	U_1	U_2	U_3	U_4	W_b	B_1
0.2000	0.2000	23.4500	6.3250	4.9600	23.6000	0.2250	1.6500
B_2	B_3	B_4	W_c	C_1	C_2	W_f	F_1
1.7000	1.7000	1.6500	1.67500	10.0500	10.0500	1.1000	2.5000
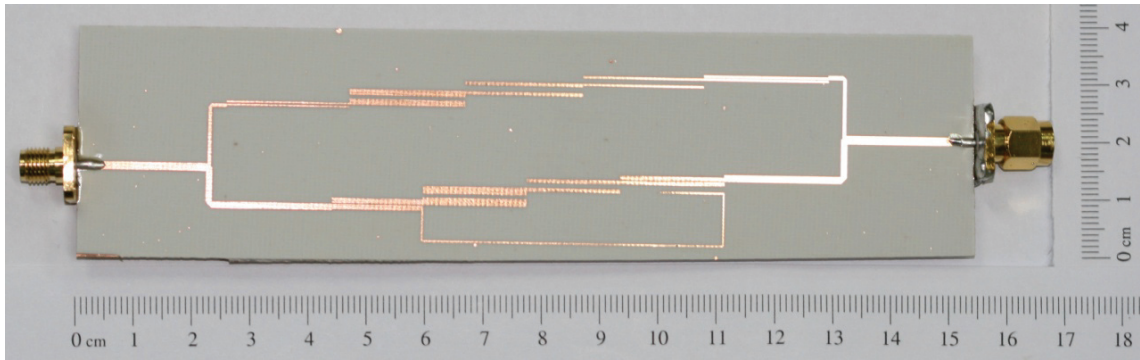
Figure 3-24 The photograph of implemented microstrip asymmetric dual-band filter with the coupling matrix listed in Table 3.9.
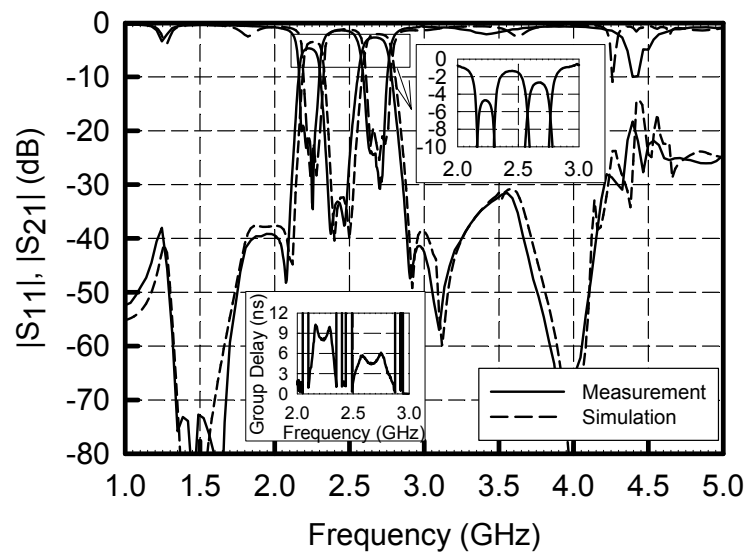
Figure 3-25 The responses for the asymmetric dual-path dual-band filter in Figure 3-24.

Furthermore, to observe the mechanism of the cross-coupling in each passband, the current density under two passbands is simulated. In Figure 3-26 (a), the current mainly flows through the upper path and the cross-coupled quadruplet at 2.69 GHz. At 2.263 GHz, the current flows through not only the lower path, but also the cross-coupled quadruplet within the upper path and the resonator 3, as shown in Figure 3-26 (b). It agrees with the discussion in Sec. 3.4.2.
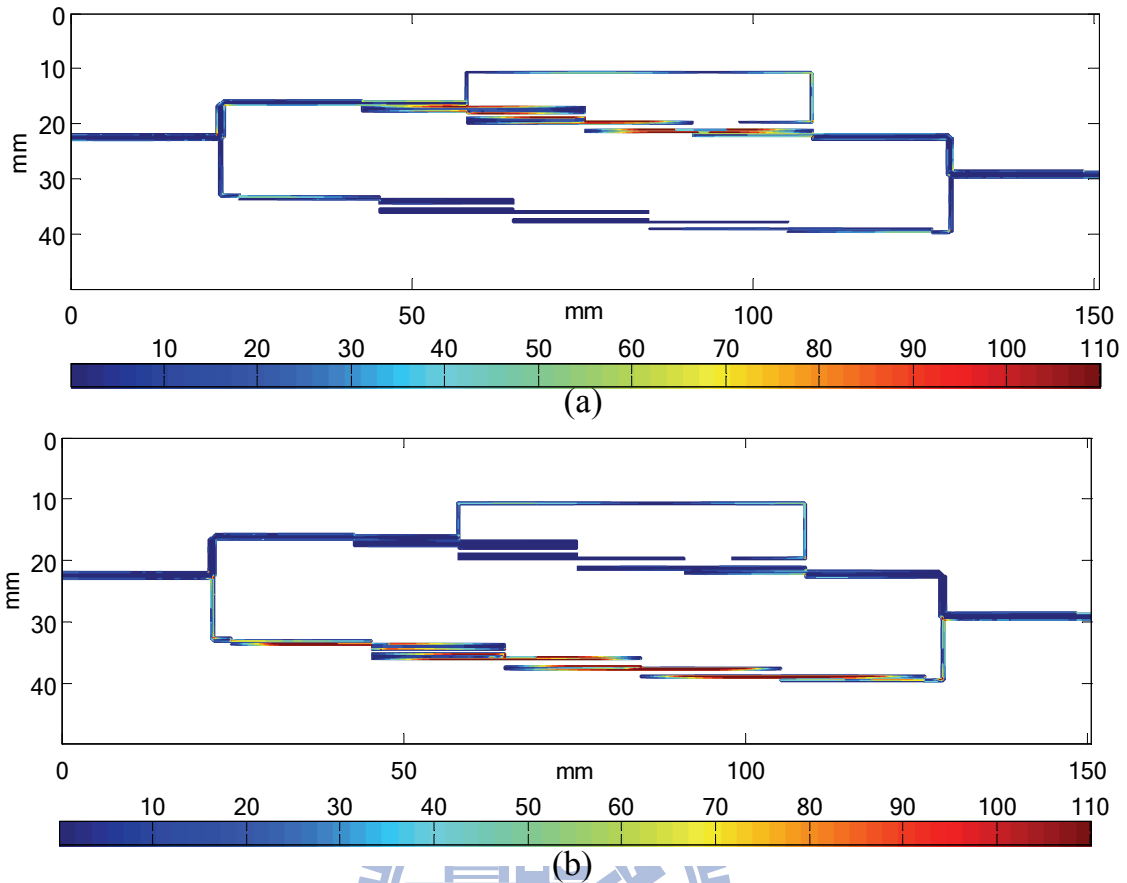
Figure 3-26 Simulated current density of the filter in Figure 3-24 (a) at 2.69 GHz, and (b) at 2.263 GHz.

3.7 Conclusion

In this chapter, we introduce the relations between the coupling coefficients and parameters of the parallel-coupled line. For the convenient of the implementation, the single-path and dual-path coupling schemes are proposed. Within these two topologies, the dual-path coupling scheme shows the advantage of the physical insights, and the transmission zeros can be assigned to each passband using the well-known mechanisms in the single-band filter design. By adding the additional quadruplet or trisection coupling scheme in the coupling paths, the dual-band filter with finite transmission zeros is design and implemented. The measured results have shown good agreement with simulated results.

Based on the synthesis procedure in Chapter 2, the proposed dual-band filters have shown

properties of the flexible response, good performance, and quick design procedure.

Chapter 4

Two-mode Dual-band Filter Design Using E-shaped Resonators

4.1 Introduction

Two-mode resonators are attractive for its advantage of the size reduction in the filter design. Based on the property of two-mode, the interaction between these two modes of the resonator can be completely separated for the physical consideration. Many articles have been provided to design the dual-band filter with two-mode resonators. However, the fully analytical design has not been proposed yet.

E-shaped resonator is validated in dual-mode single-band filter design [122]-[124] and is a good candidate in dual-band filter design [125]. The even- and odd-mode analysis of the E-shaped resonator is proposed in [122] and corresponding coupling scheme is proposed in [124]. In this chapter, the analytical approach for two-mode dual-band filter synthesis using E-shaped resonators is proposed. Based on the dual-band coupling matrix synthesis proposed in Chapter 2, the odd-mode of the E-shaped resonators is firstly analyzed to determine the dimensions corresponding to the odd-mode portion of the filter. Then, the central open-stub of the E-shaped resonator can be used to adjust the slope parameter of the even-mode to fit the requirement of the even-mode filter parameters. In addition, the out-of-phase property of the coupled edge of the E-shaped resonator is also discussed and used to improve the separation of two adjacent passbands. By properly arranging the filter layout, the filter order can be increased and the requested transmission zeros are available. The details are discussed in the following sections.

4.2 E-shaped Resonator

Figure 4-1 (a) shows the layout of the E-shaped resonator. Due to the electrically symmetric of the layout, the even- and odd-mode analysis can be applied, as shown in Figure 4-1 (b) and (c). Considering the boundary conditions of the electric field, that is, magnitude of electric field is maximum at the open end and is zero at the short end, the electric field distributions for even and odd modes of the E-shaped resonator are illustrated in Figure 4-2. In the figure, $L_b = L_{b1} + L_{b2}$, so that the λ_o is larger than λ_e. Consequently, the self-resonant frequency of the even mode is higher than that of the odd mode. Based on the property, the self-resonant frequency of the even mode can be adjusted by tuning the length of the central stub of the E-shaped resonator(i.e., L_c) while the self-resonant frequency of the odd-mode is kept unchanged.

Due to the property of the separately adjusting the resonant frequency of these two modes, the dual-band filter is now analyzed using even-odd mode analysis and the analytical synthesized procedure is provided based on the synthesized coupling matrix.
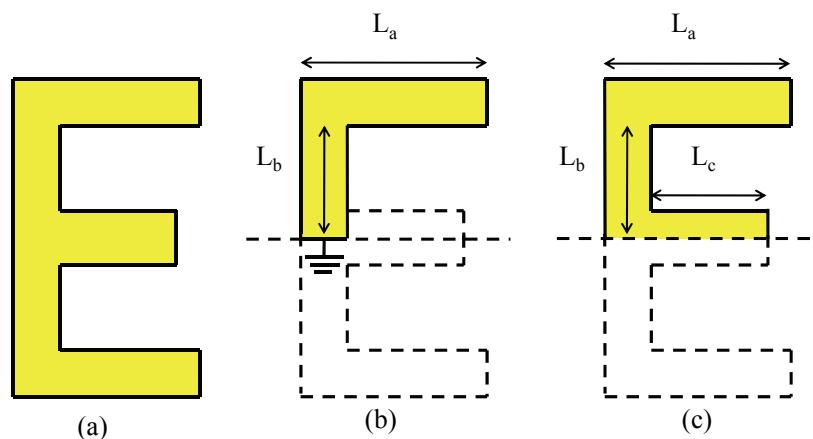
Figure 4-1 The schematic of the E-shaped resonator. (a). Layout. (b) Odd-mode. (c) Even-mode.
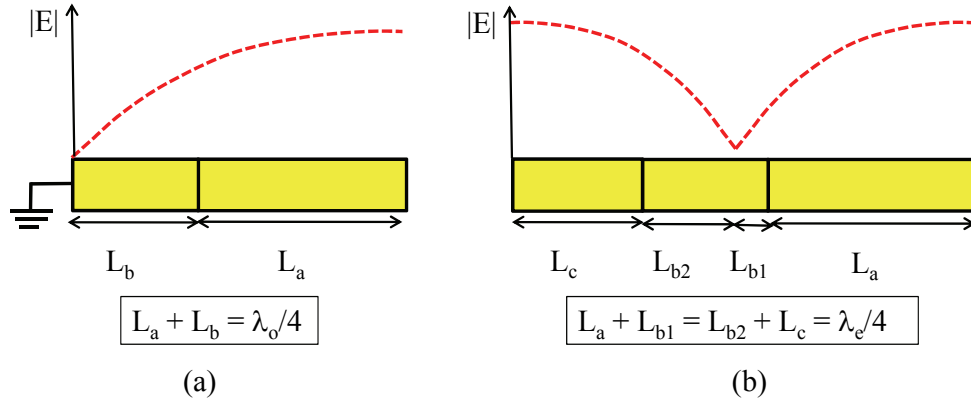
Figure 4-2 The E-field distribution for the (a) odd-mode and (b) even mode of the E-shaped resonator.

4.3 Analytical Approach in Two-mode Dual-band Filter Design Using E-shaped Resonators

Due to the even- and odd-mode of the resonators are at different resonant frequency, they are independent of the effects between each other at their operated frequency. Using these two modes to design a dual-band filter, each passband will be governed by its corresponding mode. Therefore, the proposed two-mode dual-band filter can be described by the coupling scheme shown in Figure 4-3. The two-mode mechanism is controlled by even- and odd-modes. The contributions from even- and odd-modes can be separated by two different coupling paths, and the dual-band performance of the two modes are then extracted using the coupling matrix synthesis. Each mode governs the performances of one passband. Here the back-to-back E-shaped resonator is used to construct the two-mode dual-band filter. Figure 4-4 (a) shows the layout for the proposed two-mode dual-band filter. Removing the central open stubs from the layout, as shown in Figure 4-4 (b), the odd-mode response can be analytically synthesized from the corresponding odd-mode portion of the coupling matrix. And then, the effects from the even-mode will be

introduced by adding the open stubs, which dimensions are also determined in an analytical approach. In the following, we will introduce these analytical procedures to synthesize the two-mode dual-band filters.
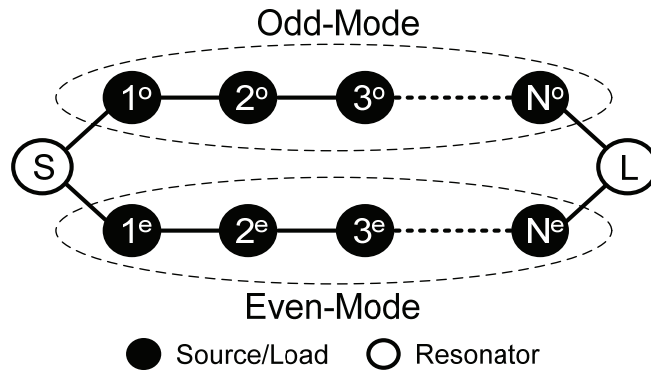
Figure 4-3 The coupling scheme for the two-mode dual-band filter design.

(a)   (b)
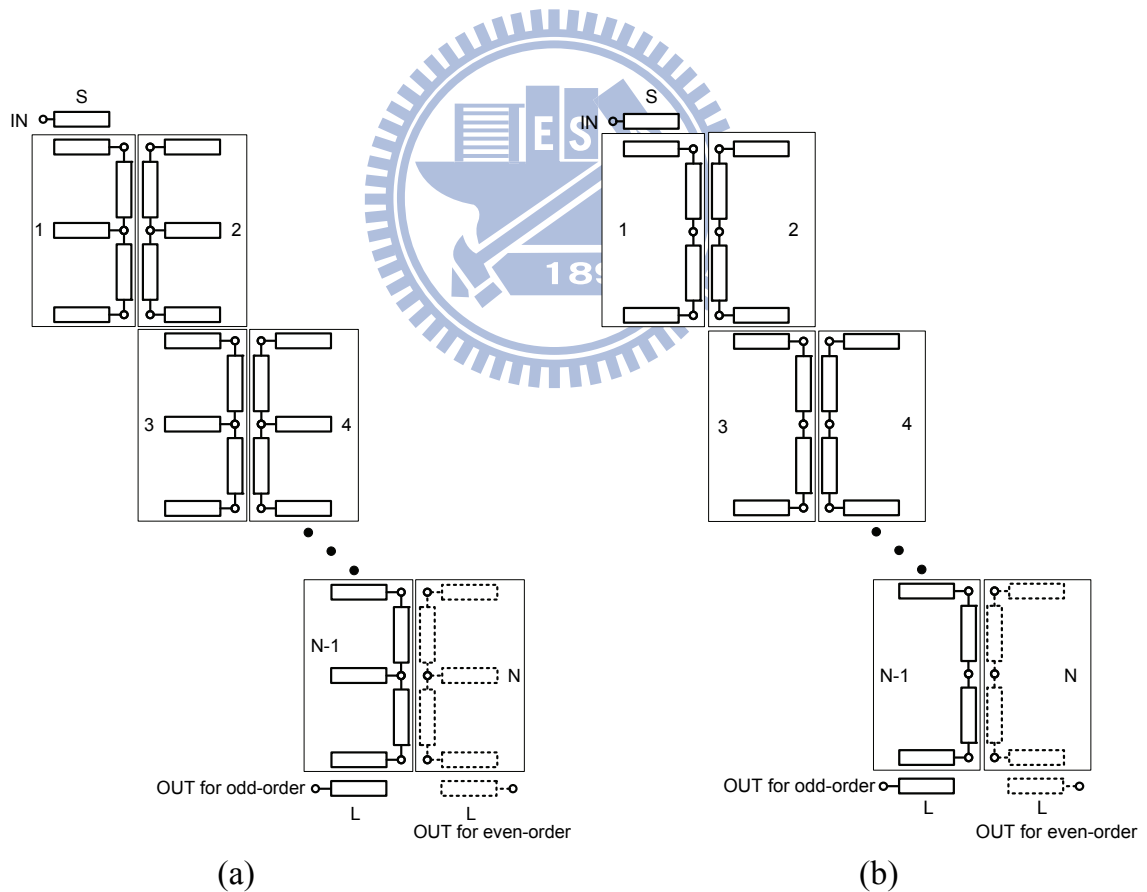
Figure 4-4 (a) The proposed two-mode dual-band filter. (b) The layout for the odd-mode portion of the two-mode dual-band filter. The number shows the resonator index.

4.3.1 Analytical Approach for the Odd-mode Analysis

For the odd-mode analysis, the central open-stub in each E-shaped resonator has no effect. Therefore, it can be removed when designing the odd-mode filter. Figure 4-5 shows a generalized representation of a bandpass filter with resonators and J inverters. To evaluate the values of Js, (3-6) is applied. Once the values of the J inverters are obtained, the even- and odd-mode characteristic impedance for parallel-coupled line can be calculated by (3-7). For the anti-parallel coupled line [141], the formulation is shown in (4-1). Note that the electrical length if the anti-parallel coupled line should not equal 90°.

$$\frac{Z_{oe}}{Z_0} = \frac{1 + (JZ_0)\tan\theta}{1 - (JZ_0)\cot\theta},$$
$$\frac{Z_{oo}}{Z_0} = \frac{1 - (JZ_0)\tan\theta}{1 - (JZ_0)\cot\theta}. \tag{4-1}$$
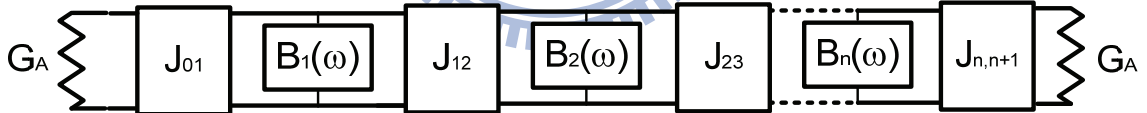
Figure 4-5 A generalized band-pass filter circuit using admittance inverters.

4.3.2 Analytical Approach for the Even-mode Analysis

Now adding the central open-stub to the E-shaped resonator as shown in Figure 4-6 to design the even-mode-filter, note that the only adjustable parameters are the impedance and the electrical length of the central open-stub. These parameters must be adjusted to match the even-mode resonant frequency and the slope parameter to fit the requirement of $J^e_{j-1,j}$. Based on the extracted $Z_{oe,j-1,j}$ and $Z_{oo,j-1,j}$ for the coupled lines, the $J^e_{j-1,j}$ is obtained

by (3-7). By the known $J^e_{j-1,j}$ and $M^e_{j-1,j}$, the slope parameter can be obtained by (3-6).

To calculate the slope parameter from the equivalent circuit, Figure 4-7 shows the corresponding half circuit for even-mode analysis. In Figure 4-7, the slope parameter for even-mode half circuit can be obtained by (4-2)

$$Z^e_{in} = Z_0 \frac{2Z_S - Z_0 \tan\theta_1' \tan\theta_2}{jZ_0 \tan\theta_2 + j2Z_S \tan\theta_1'},$$

$$Y^e_{in} = j \frac{Z_0 \tan\theta_2 + 2Z_S \tan\theta_1'}{2Z_0 Z_S - Z_0^2 \tan\theta_1' \tan\theta_2} = jB^e, \qquad (4\text{-}2)$$

$$b^e = \frac{\omega_e}{2}\left(\frac{dB^e}{d\omega}\right).$$

where ω_e is the even-mode resonant frequency.

In Figure 4-7, the even-mode resonant condition is

$$Y^e_{in} = 0 \Rightarrow Z_S = -\frac{Z_0 \tan\theta_2}{2 \tan\theta_1'}. \qquad (4\text{-}3)$$
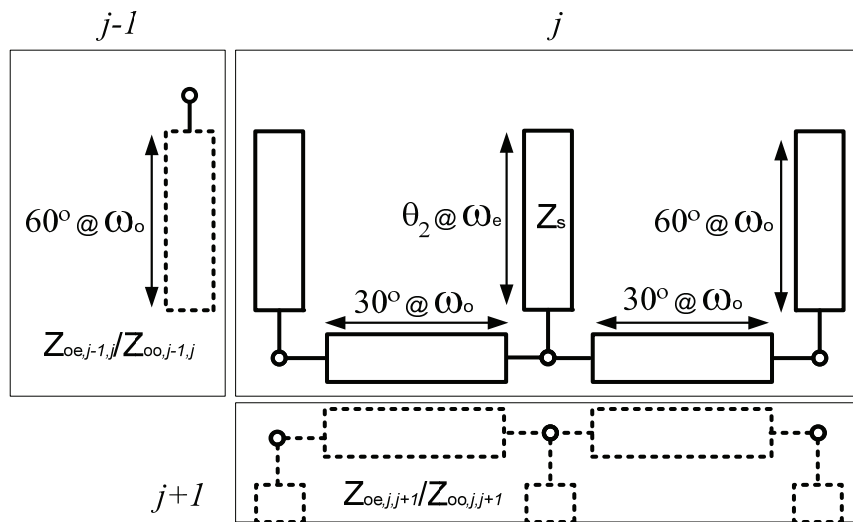
Figure 4-6 The circuit schematic of the E-shaped resonator.
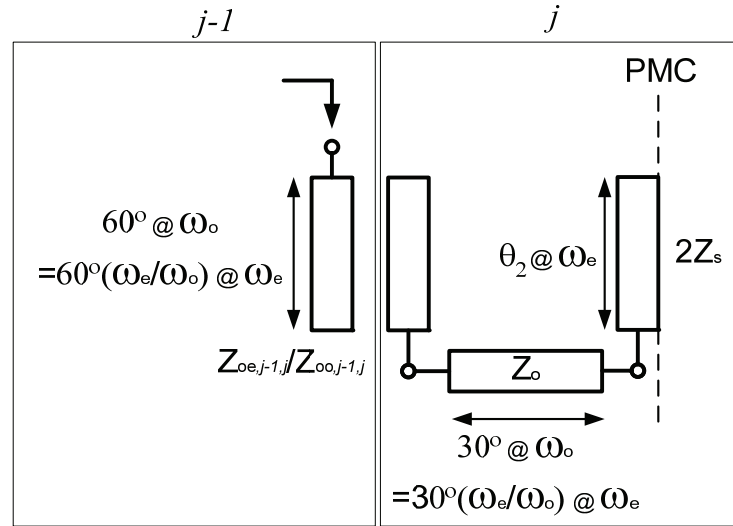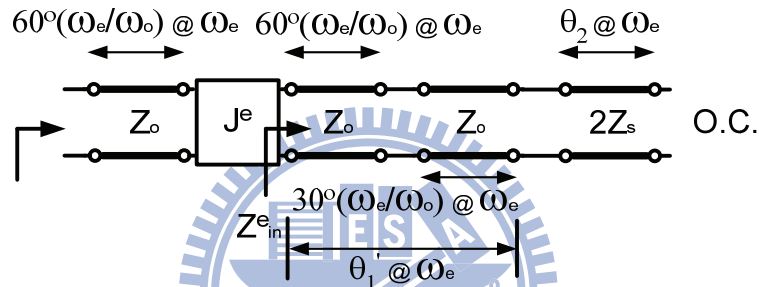
Figure 4-7 (a) The even-mode analysis for the E-shaped resonator in Figure 4-6. (b) The equivalent circuit for the even-mode analysis.

By rearranging (4-2) we have

$$Z_S = \frac{Z_0 \theta_2 \sec^2 \theta_2 + 2Z_0^2 \tan \theta_1' \tan \theta_2 b^e}{4b^e Z_0 - 2\theta_1' \sec^2 \theta_1'}. \qquad (4\text{-}4)$$

To solve (4-3) and (4-4), the variables Z_S and θ_2 can be determined. Because the Z_{oe} and Z_{oo} based on $M^o_{j,j+1}$ are already fixed when designing the odd-mode filter, once the Z_S and θ_2 are obtained, the corresponding coupling coefficient for even-mode $M^e_{j,j+1}$ is fixed accordingly. This phenomenon restricts the achievable filter parameters for the even-mode.

To identify the available dual-band characteristics, the $M^e_{j,j+1}$ of the extracted layout needs to be estimated. Figure 4-8 shows the circuit that is used to identify the coupling coefficient between two E-shaped resonators operating at even-mode.
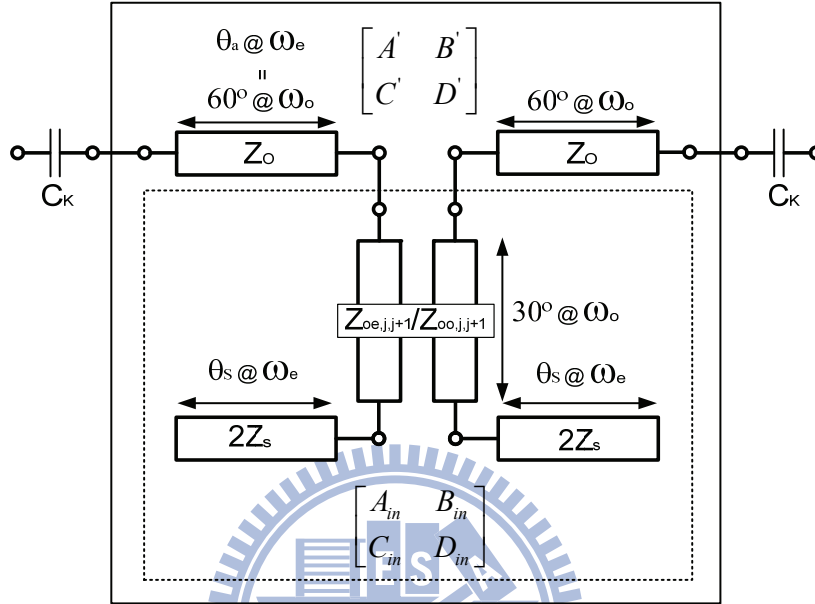
Figure 4-8 The circuit is proposed to identify the coupling coefficient between two E-shaped resonators operating at even-mode.

The S_{21} can be derived based on the *ABCD* matrix of the circuit shown in Figure 4-8. The poles of S_{21} are dominated by element *C'* of the sub-*ABCD* matrix shown in Figure 4-8 due to the weak coupling (i.e., a very small value of capacitor C_K). To find the roots of *C'*, the details is derived as follows. Firstly, the well-known equation for determining the coupling coefficient is

$$k = M_{1,2}\Delta = \frac{f_H^2 - f_L^2}{f_H^2 + f_L^2}.$$

(4-5)

Let

$$f^e = \frac{f_H + f_L}{2}.$$ (4-6)

The above equations can be represented as

$$f_H = \frac{2f^e}{1 + \sqrt{\frac{1+k}{1-k}}}, f_L = \sqrt{\frac{1+k}{1-k}} f_H.$$ (4-7)

Based on the coupling coefficient, two resonant frequencies can be obtained. Furthermore, the resonant frequencies can be also derived from the circuit in Figure 4-8. To use the cascade *ABCD* matrix, the *ABCD* matrix of the whole circuit can be represented as

$$\begin{bmatrix} A & B \\ C & D \end{bmatrix} = \begin{bmatrix} A' + \dfrac{C'}{j\omega C_K} & \dfrac{A'}{j\omega C_K} + B' - \dfrac{C'}{(\omega C_K)^2} + \dfrac{D'}{j\omega C_K} \\ C' & D' + \dfrac{C'}{j\omega C_K} \end{bmatrix}.$$ (4-8)

Based on the *ABCD* matrix, the S_{21} can be represented as

$$S_{21} = \frac{2}{A + B/Z_0 + CZ_0 + D}$$

$$= \frac{2}{A'\left(1 + \dfrac{1}{j\omega C_K Z_0}\right) + C'\left(Z_0 + \dfrac{2}{j\omega C_K} - \dfrac{1}{(\omega C_K)^2 Z_0}\right) + \dfrac{B'}{Z_0} + D'\left(1 + \dfrac{1}{j\omega C_K Z_0}\right)} \cdot$$ (4-9)

The resonances are the roots of the denominator of S_{21}. For the weak coupling test, here the

capacitance of C_K is chosen as a very small value, say 0.0001 pF, Hence the $1/(\omega C_K)^2$ has relatively larger value than other terms, so the roots of C' is close to the roots of the denominator of S_{21}.

To find the expression C', the analysis procedure in [141] can be applied to obtained the A_{in}, B_{in}, C_{in}, and D_{in} by terminating two terminals of the coupled line with transmission lines, which have θ_S length and characteristic impedance $2Z_S$. Finally, C' can be represented as

$$C' = jA_{in}Y_0 \sin\theta_a \cos\theta_a - Y_0^2 B_{in}\sin^2\theta_a + C_{in}\cos^2\theta_a + jY_0 D_{in}\sin\theta_a\cos\theta_a. \quad (4\text{-}10)$$

In (4-10), where

$$A_{in} = \left(a_{11}\chi + b_{11}\right)\left(-c_{11}\chi - d_{11}\right) + b_{12}c_{12}\chi,$$
$$B_{in} = -\left(a_{11}\chi + b_{11}\right)\left(a_{22}\chi + b_{22}\right) + b_{12}b_{21},$$
$$C_{in} = \left(c_{11}\chi + d_{11}\right)\left(-c_{22}\chi - d_{22}\right) + c_{12}c_{21}\chi^2,$$
$$D_{in} = -\left(c_{11}\chi + d_{11}\right)\left(a_{22}\chi + b_{22}\right) - c_{12}b_{21}\chi,$$

and

$$a_{11} = a_{22} = d_{11} = d_{22} = \cos\left(\theta_a/2\right),$$
$$a_{12} = a_{21} = d_{12} = d_{21} = 0,$$
$$b_{11} = b_{22} = 0.5j\left(Z_{oe} + Z_{oo}\right)\sin\left(\theta_a/2\right),$$
$$b_{12} = b_{21} = 0.5j\left(Z_{oe} - Z_{oo}\right)\sin\left(\theta_a/2\right),$$
$$c_{11} = c_{22} = 0.5j\left(1/Z_{oe} + 1/Z_{oo}\right)\sin\left(\theta_a/2\right),$$
$$c_{12} = c_{21} = 0.5j\left(1/Z_{oe} - 1/Z_{oo}\right)\sin\left(\theta_a/2\right).$$

From the above equation, it can be noted that C' is a real coefficient equations and it is a second order equation with variable $\chi = -2Z_S\cot\theta_S$. Hence the roots of C' can be

obtained using the quadratic formula.

Based on (4-10), the roots of the denominator of S_{21} can be obtained by root finding for C' under the weak coupling test. The exact value of the roots can be also obtained by (4-7). Due to the solutions from (4-7) are equal to the roots of C', the derived equation is obtained as follows:

$$\alpha\chi^2 + \beta\chi + \gamma = 0, \text{ where}$$

$$\begin{cases}
\alpha = \dfrac{1}{Z_0}\left(\dfrac{1}{Z_{oe,j,j+1}} + \dfrac{1}{Z_{oo,j,j+1}}\right)S_1 C_1 S_2 C_2 + \dfrac{1}{Z_0^2}C_1^2 S_2^2 + \dfrac{1}{Z_{oe,j,j+1}Z_{oo,j,j+1}}C_2^2 S_1^2, \\[2ex]
\beta = \dfrac{1}{Z_0}\left(\dfrac{Z_{oo,j,j+1}}{Z_{oe,j,j+1}} + \dfrac{Z_{oe,j,j+1}}{Z_{oo,j,j+1}}\right)S_1^2 S_2 C_2 - \dfrac{2}{Z_0^2}C_1^2 S_2 C_2 \\[2ex]
\quad + \dfrac{1}{Z_0}\left(Z_{oe,j,j+1} + Z_{oo,j,j+1}\right)S_2^2 S_1 C_1 - \left(\dfrac{1}{Z_{oe,j,j+1}} + \dfrac{1}{Z_{oo,j,j+1}}\right)C_2^2 S_1 C_1, \\[2ex]
\gamma = -\dfrac{1}{Z_0}\left(Z_{oe,j,j+1} + Z_{oo,j,j+1}\right)S_1 C_1 S_2 C_2 + \dfrac{Z_{oe,j,j+1}Z_{oo,j,j+1}}{Z_0^2}S_1^2 S_2^2 + C_1^2 C_2, \\[2ex]
S_1 = \sin\dfrac{\theta_a}{2}, C_1 = \cos\dfrac{\theta_a}{2}, S_2 = \sin\theta_a, C_2 = \cos\theta_a.
\end{cases} \qquad (4\text{-}11)$$

Solving the equation, two resonant frequencies, which are f_H and f_L, can be extracted, and they are corresponding to two peaks of S_{21}. Then the coupling coefficient is

$$k_{j,j+1}^e = M_{j,j+1}\Delta = \frac{f_H^2 - f_L^2}{f_H^2 + f_L^2}. \qquad (4\text{-}12)$$

where f_H is the root with larger value than f_L.

4.3.3 Impact of the Constrained Even-Mode k^e on the Filter Performance

Because the even-mode coupling coefficient of the back-to-back E-shaped resonator is fixed during designing the odd-mode filter, the available even-mode filter parameters have limitations and will be discussed in the following. Here two cases are analyzed. The first one is to change the bandwidth ratio with frequency ratio as a parameter but the odd-mode bandwidth is fixed as 10%. The second condition is with a fixed frequency ratio but the bandwidth ratio is varied. Using (4-12), the impact on the return loss of the even-mode passband due to the relative error of coupling coefficient (Δk^e) can be observed through following examples. Here three topologies are used, as shown in Figure 4-9. Figure 4-10 shows the theoretical results of the two-mode dual-band filter with different central frequency ratio but the odd-mode bandwidth is fixed to be 10% and the bandwidth ratio is also fixed to be 1.3. Figure 4-11 shows the calculated Δk^e of the proposed analytical design of back-to-back E-shaped resonator versus bandwidth ratio with frequency ratio as a parameter where the odd-mode bandwidth keeps being 10%. On the other hand, Figure 4-12 shows the theoretical return loss of the same coupling scheme. In this case, however, the central frequency ratio is fixed to be 0.75 with different fractional bandwidth. Again, Figure 4-13 shows the Δk^e versus bandwidth ratio.
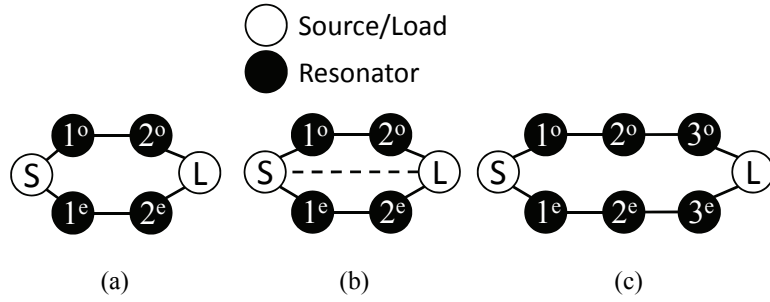
Figure 4-9 Three topologies used for estimating k^e. (a) The coupling scheme for the coupling matrix in Table 4.1. (b) The coupling scheme for the Example 1 in the following section. (c) The coupling scheme for the Example 2 in the following section.
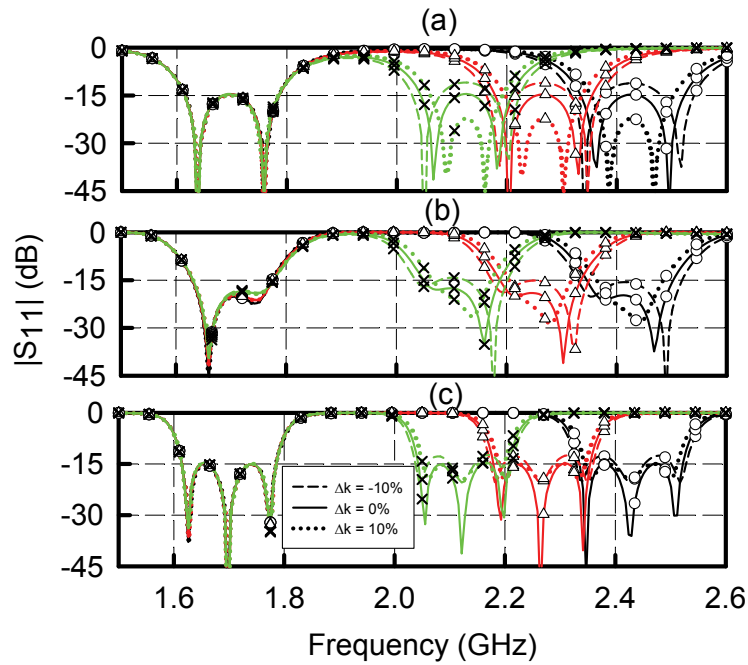
Figure 4-10 S_{11} with various even-mode frequencies. (a) Coupling scheme shown in Figure 4-9 (a) with 15 dB return loss. (b) Coupling scheme shown in Figure 4-9 (b) with 20 dB return loss. (c) Coupling scheme shown in Figure 4-9 (c) with 15 dB return loss. (Circle: f_o = 0.8f_e. Triangle: f_o = 0.75f_e, X: f_o = 0.7f_e). All cases are under the 10% fractional bandwidth on odd-mode and $\Delta^{odd}/\Delta^{even}$ = 1.3.
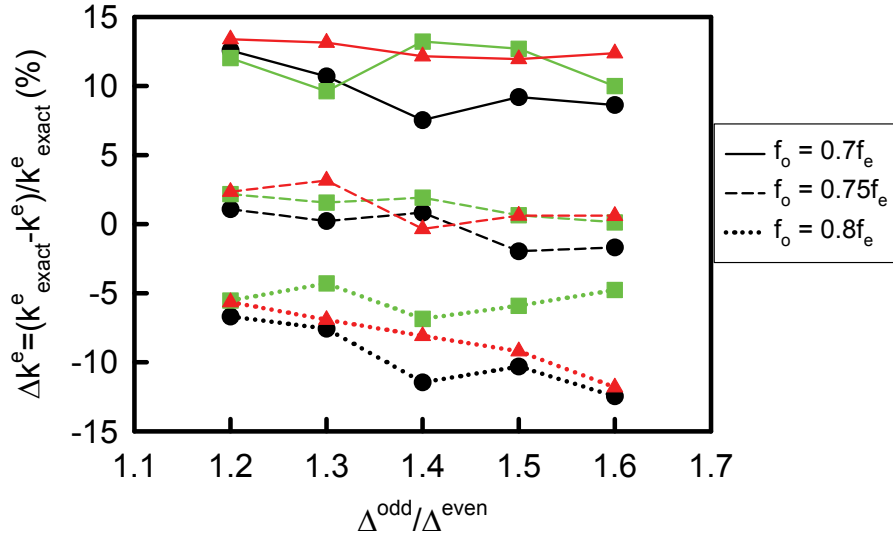
Figure 4-11 The difference between the exact and the estimated coupling coefficients with various fractional bandwidth on even-mode and different frequency ratios of two passbands. (Triangle: Coupling scheme shown in Figure 4-9 (a) with 15 dB return loss. Circle: Coupling scheme shown in Figure 4-9 (b) with 20 dB return loss. Square: Coupling scheme shown in Figure 4-9 (c) with 15 dB return loss). All cases are under the 10% fractional bandwidth on odd-mode.
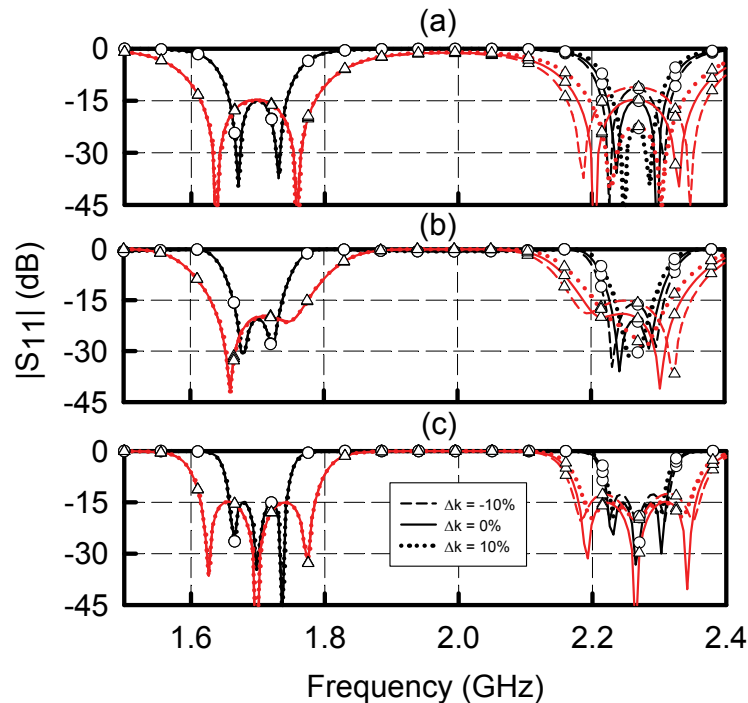
Figure 4-12 S_{11} with various fractional bandwidths on odd-mode. (a) Coupling scheme shown in Figure 4-9 (a) with 15 dB return loss. (b) Coupling scheme shown in Figure 4-9 (b) with 20 dB return loss. (c) Coupling scheme shown in Figure 4-9 (c) with 15 dB return

loss. (Circle: Δ^{odd} = 5%. Triangle: Δ^{odd} = 10%). All cases are under $f_o = 0.75f_e$ and Δ^{odd} / Δ^{even} = 1.3.
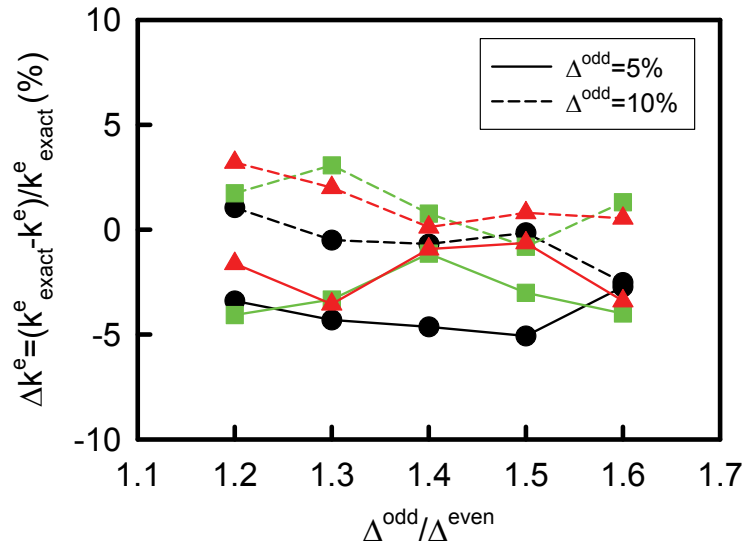
Figure 4-13 The difference between the exact and estimated coupling coefficients with various fractional bandwidth on both odd- and even-modes. (Triangle: Coupling scheme shown in Figure 4-9 (a) with 15 dB return loss. Circle: Coupling scheme shown in Figure 4-9 (b) with 20 dB return loss. Square: Coupling scheme shown in Figure 4-9 (c) with 15 dB return loss). All cases are under $f_o = 0.75f_e$.

Figure 4-11 gives designers a guideline to choose the frequency ratio under the specific coupling scheme. Here Δ^{odd} /Δ^{even} = 1.3 is used as an example to explain how to choose the frequency ratio. For the case which has the coupling scheme in Figure 4-9 (b) with 20 dB return loss (circle symbol), it shows Δk^e is about +11% under $f_o = 0.7f_e$ (solid line), Δk^e is about +0.5% under $f_o = 0.75f_e$ (dashed line), and Δk^e is about -7% under $f_o = 0.8f_e$ (dotted line). Compared with the results shown in Figure 4-10 (b), the S-parameters under $f_o = 0.7f_e$ with +11% relative error is close to the dotted line with X symbols, the S-parameters under $f_o = 0.75f_e$ with +5% relative error is close to the solid line with triangle symbols, and the S-parameters under $f_o = 0.8f_e$ with -7% relative error is close to the dashed line with circle symbols.

From the discussion above, while the coupling scheme in Figure 4-9 (b) with 20 dB

return loss chosen with $\Delta^{odd}/\Delta^{even} = 1.3$, the frequency ratio $f_o = 0.75f_e$ is the better choice

for the small relative error. For the example shown in Figure 4-18, the $\Delta^{odd}/\Delta^{even} = 1.3$ and

$f_o = 0.718f_e$, such that the relative error of coupling coefficient is within 0~10% as shown

in Figure 4-11. The same analysis can be applied to Figure 4-13. For other specific

coupling scheme, the figure of relative errors has to be firstly analyzed to provide the

guideline in two-mode dual-band filter design.

4.3.4 Analytical Calculation Example: Fourth-order Two-mode Dual-band Bandpass Filter

To demonstrate the proposed analytical approach for two-mode dual-band bandpass

filter design, a forth-order two-mode dual-band filter is used as an example. The filter

parameters for the dual-band synthesis are as follows: The first passband central frequency

is firstly shifted from 0 to -0.764 rad/s at the lowpass domain and the multi-band lowpass

domain bandwidth is 0.4587 rad/s. Similarly, the second passband central frequency is

shifted from 0 to 0.8211 rad/s and the multi-band lowpass domain bandwidth is 0.3489

rad/s. Both filters are the second-order filters with return loss of 15 dB. After parallel

addition of two filtering functions, the corresponding coupling matrix is obtained in Table

4.1 with coupling scheme shown in Figure 4-9. The four-pole dual-band filter is then

transformed to the bandpass domain with central frequency at 2 GHz and the fractional

bandwidth bandwidth 40%. It means the frequencies for odd- and even-mode are 1.707 and

2.376 GHz, with odd-mode bandwidth 1.3 times larger than that of even-mode. The circuit

schematic of the two-mode dual-band filter is illustrated in Figure 4-14. To evaluate the

parameters for odd-mode firstly, the central open-stubs are removed and the corresponding

layout is shown in Figure 4-15. The values of the J inverters are then calculated by (3-6)

and Z_{oe} and Z_{oo} of the coupled line are obtained by (3-7) and (4-1) and shown in Table 4.2 with $E_1 = E_2 = 2E_3 = 60^o$. The Z_{oe} and Z_{oo} for the $M_{S,1}{}^o$ and $M_{2}{}^o{}_{,L}$ are calculated by (3-7), and Z_{oe} and Z_{oo} for the $M_{1}{}^o{}_{,2}{}^o$ are calculated by (4-1). The odd-mode performances are simulated with ADS and shown in Figure 4-16, where the performances from the extracted circuits agree well with that from the coupling matrix.

Table 4.1 Coupling Matrix for the Two-mode Dual-band Filter

	S	1°	2°	1^e	2^e	L
S	0.0	0.4973	0.0	0.4404	0.0	0.0
1°	0.4973	0.8043	0.2872	0.0	0.0	0.0
2°	0.0	0.2872	0.8043	0.0	0.0	-0.4973
1^e	0.4404	0.0	0.0	-0.8614	0.2202	0.0
2^e	0.0	0.0	0.0	0.2202	-0.8614	0.4404
L	0.0	0.0	-0.4973	0.0	0.4404	0.0
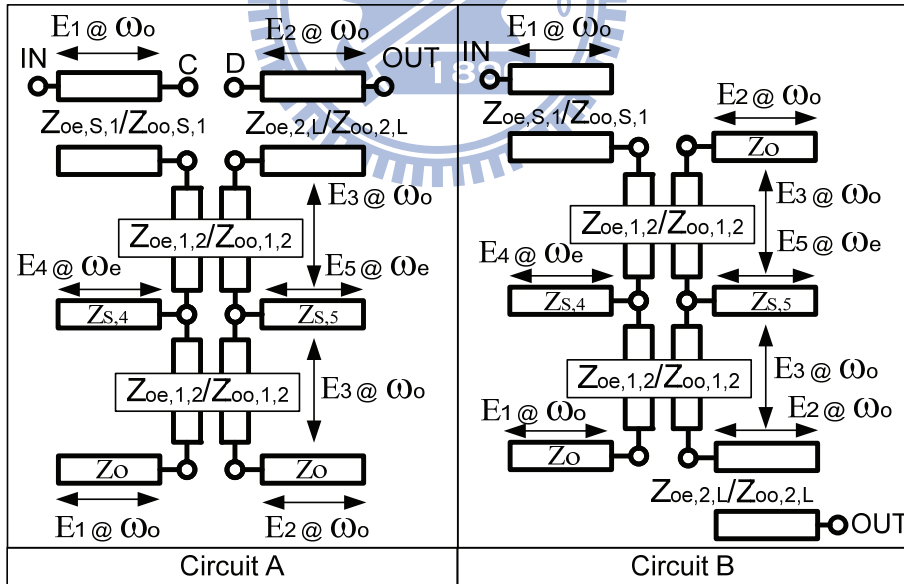
Figure 4-14 Two proposed layouts of back-to-back E-shaped resonators.
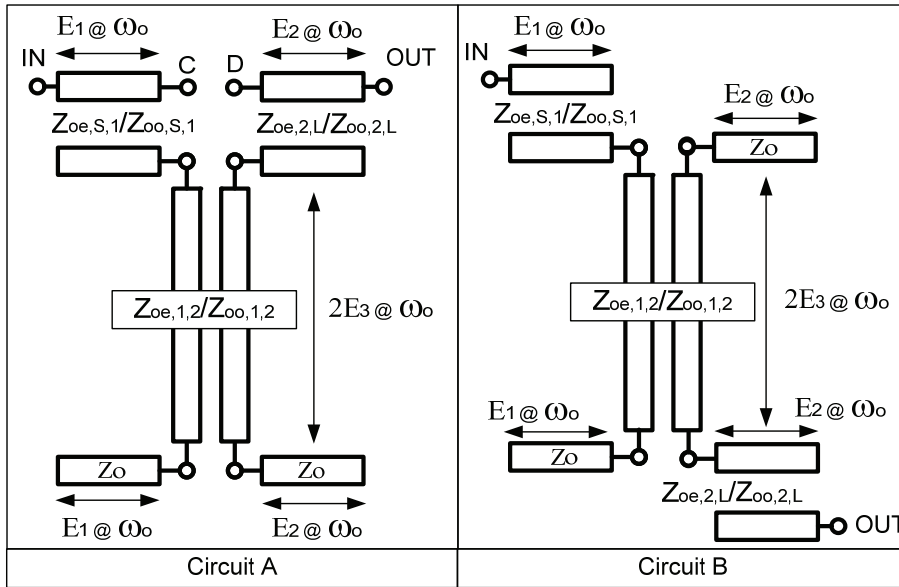
Figure 4-15 The corresponding layout for the odd-mode part of the filter

Table 4.2 The Calculated Impedances for the Odd-mode Analysis

	$M_{S,1}^{o}$	$M_{1^o,2^o}$	$M_{2^o,L}$
J	0.0079	0.0018	0.0079
Z_{oe}	84.9270	62.3482	84.9270
Z_{oo}	36.9231	40.9896	36.9231
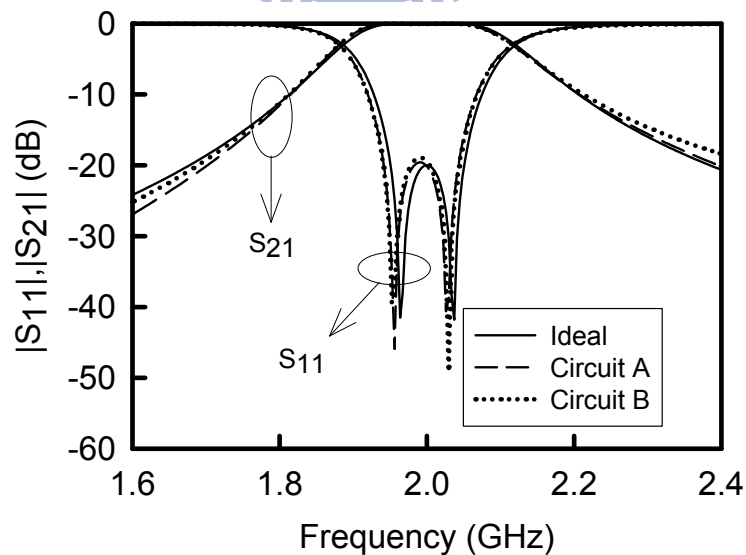
Figure 4-16 The performances for the odd-mode part of the filter in Figure 4-15.

Furthermore, it is worth to point out that the two output ports in circuit A and circuit

B receive signals with the same amplitude but 180 degree out-of-phase, as shown in Figure 4-16 and Figure 4- 17. It can be illustrated using the odd-mode analysis. Due to the odd-mode, the electrical fields ate two ends of the resonator have same magnitude but they are 180-degree out-of-phase. This phase inversion has no influence on a single mode filter but can provide an extra transmission zero for two-mode filter. Now, the odd mode filter design is completed.
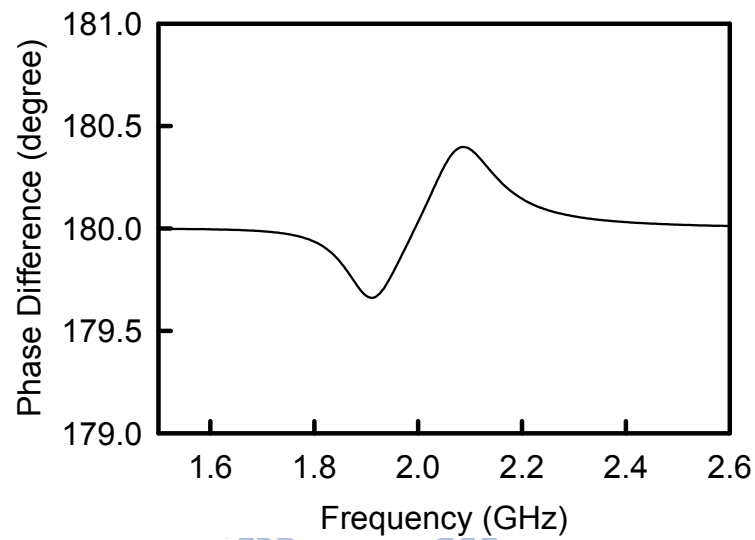
Figure 4- 17 The 180-degree out-of-phase between two output ports in Figure 4-15.

To introduce the even-mode, we add the central open-stubs. Use (4-3) and (4-4), $Z_{S,4}$ = $Z_{S,5}$ = 20.3602 Ω and E_4 = E_5 = 49.025$^\text{o}$. Using (4-11) and (4-12), the estimated $k^e_{1,2}$ is 0.0829, such that the approximated $M_{1,2}^{e}$ is 0.2072. (Here the ideal $M_{1,2}^{e}$ is 0.2202.) The simulation results are obtained using ADS and shown in Figure 4-18.
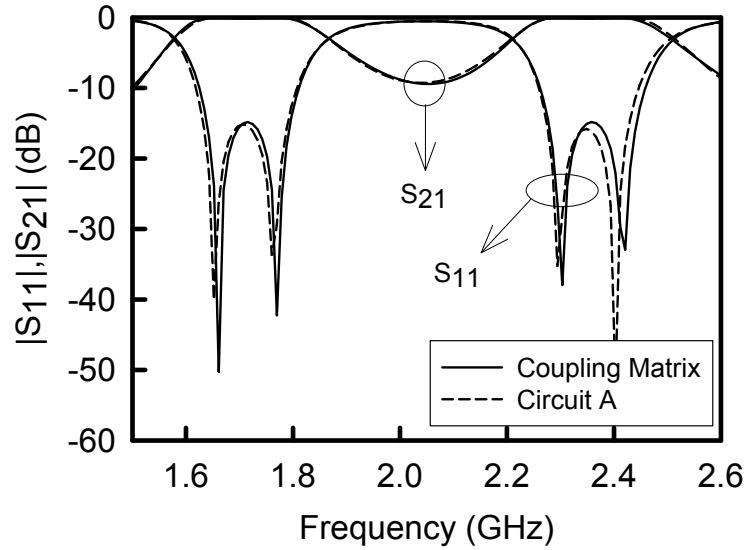
Figure 4-18 The performance of the two-mode dual-band filter of the circuit A in Figure 4-14

It should be pointed out that as the sign of elements $M_{2^o,L}$ and $M_{L,2^o}$ in Table 4.1 is changed, i.e., -0.4973, a transmission zero appears between two passbands and provides a good rejection of these two passbands. As we have mentioned, different circuit prototypes of back-to-back E-shaped resonators provide 180 degree phase difference, and it corresponds to the sign change in the coupling coefficient. Hence when choosing the circuit B in Figure 4-14 without changing the layout dimensions, the new response is shown in Figure 4-19. It provides an easy physical mechanism to change the sign of the coupling coefficient. In this case, with moving the output port location, the stopband rejection can be enhanced.

In this example, the $\Delta^{odd}/\Delta^{even} = 1.3$ and $f^o = 0.718f^e$, such that the relative error of the coupling coefficient is within 0~10% as shown in Figure 4-11. Hence in Figure 4-10 we predict the return loss level of the second passband will be larger than 20 dB, and it agrees with the result shown in Figure 4-19.
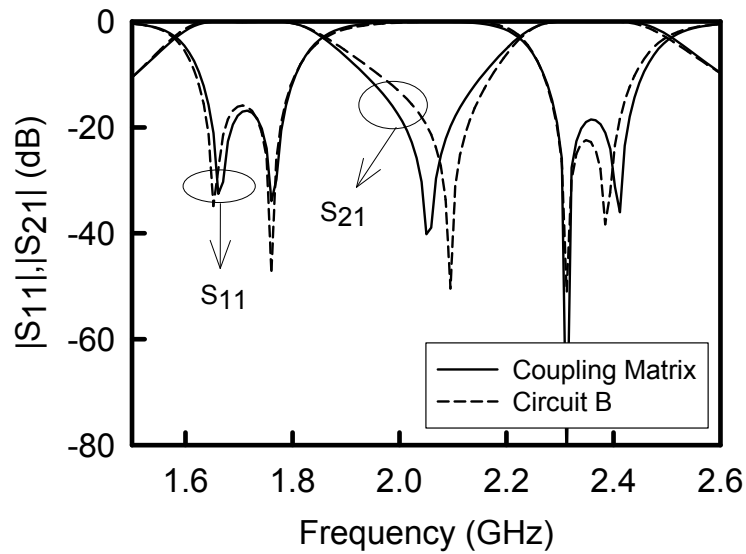
Figure 4-19 The performance of the two-mode dual-band filter of the circuit B in Figure 4-14.

4.4 Examples for Practical Filter Implementation

The two-mode dual-band filters with E-shaped resonators have been synthesized analytically using the proposed approach. Furthermore, the additional transmission zeros on the stopbands can be analyzed using the coupling matrix synthesis, and they are introduced in the following examples. For the practical implementation, a 0.635-mm-thick Rogers RT/Duroid 6010 substrate, with a relative dielectric constant 10.2 and a loss tangent of 0.0021, is used to implement following filters.

4.4.1 Example 1: Fourth-order Two-mode Dual-band Bandpass Filter with 4 Transmission Zeros

In this example, the performance of the fourth-order two-mode-dual-band bandpass

filter is determined by the analytical coupling matrix synthesis procedure in Chapter 2. The relative error of coupling coefficient can be obtained by the lines with triangle symbol in Figure 4-11. In this example we choose $\Delta^{odd}/\Delta^{even} = 1.3$ and $f_o = 0.707f_e$, so that the relative error is 0~10%. Based on the above relation, we choose $f_o = 1.688$ GHz and $f_e = 2.385$ GHz. The settings for the synthesis procedure are as follows: The first passband central frequency is firstly shifted from 0 to -0.8219 rad/s with two shifted transmission zeros at -1.55 and -0.095 rad/s and the multi-band lowpass domain bandwidth is 0.43 rad/s in the lowpass domain. Similarly, the second passband central frequency is shifted from 0 to 0.863 rad/s with two shifted transmission zeros at 0.15 and 1.6 rad/s and the multi-band lowpass domain bandwidth is 0.36 rad/s in the lowpadd domain. Both filters are the second-order filters with return loss 14.5 dB. After parallel addition of two filtering functions, the lowpass domain response of the dual-band filter is shown in Figure 4-20 and the coupling scheme is shown in Figure 4-9 (b). The corresponding coupling matrix is listed in Table 4.3. The four-pole dual-band filter is then transformed to the bandpass domain with central frequency of 2 GHz and bandwidth of 40%.

Figure 4-20 The lowpass response and the coupling scheme for example 1.

Table 4.3 The Coupling Matrix for the Filter in Example 1.

	S	1°	2°	1^e	2^e	L
S	0.0	0.4973	0.0	0.4244	0.0	-0.2427
1°	0.4973	0.8331	0.3007	0.0	0.0	0.0
2°	0.0	0.3007	0.8439	0.0	0.0	0.4304
1^e	0.4244	0.0	0.0	-0.8739	0.2309	0.0
2^e	0.0	0.0	0.0	0.2309	-0.8846	0.3831
L	-0.2427	0.0	0.4304	0.0	0.3831	0.0

To implement this filter using the proposed method, here the source-load coupling is firstly neglected and it will be discussed latter. The first phase is odd-mode analysis. The odd-mode portion governs the lower passband and the odd-mode coupling path is S-1°-2°-L of the coupling scheme in the Figure 4-9 (b). Based on that E_1 and E_2 are both 60° and E_3 is 30° in Figure 4-15, the values of J inverters can be calculated by (3-6), (3-7), and (4-1) with $M_{S,1}{}^o$, $M_{1}{}^o{}_{,2}{}^o$, and $M_2{}^o{}_{,L}$, and the calculated Z_{oe} and Z_{oo} are listed in Table 4.4. After determining the Z_{oe} and Z_{oo}, the second phase is to do the even-mode analysis. The central frequency of these two passbands are 1.688 and 2.385 GHz, such that the extracted $Z_{S,4}$ and θ_4 based on $M_{S,1}{}^e$ are 19.5383 Ω and 45.8750^o, and $Z_{S,5}$ and θ_5 based on $M_2{}^e{}_{,L}$ are 14.5280 Ω and 37.4750^o by (4-3) and (4-4). Furthermore, for the implementation issue, the circuit A in Figure 4-14 is used for the convenience of the source-load coupling.

Table 4.4 The Calculated Impedances for the Odd-mode Analysis in Example 1.

	$M_{S,1}{}^o$	$M_{1}{}^o{}_{,2}{}^o$	$M_2{}^o{}_{,L}$
J	0.0076	0.0019	0.0068
Z_{oe}	83.1529	63.0422	78.5648
Z_{oo}	37.0656	40.6257	37.5806

To model the source-load coupling the capacitive type π section is used due to the negative source-load coupling coefficient (i.e., $M_{S,L}$ = -0.2427), and the π section to is

shown in Figure 4-21. To make Y matrices of the π section and the source-load coupling equal, the value of C is

$$C = -\frac{M_{S,L}}{\omega_0 Z_0} \tag{4-13}$$
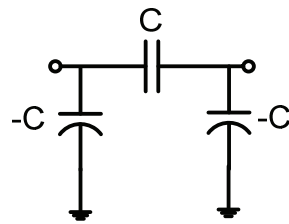
Figure 4-21 The capacitor type π section for source-load coupling in example 1.

Here the designated central frequency 2 GHz is used and then initial C is 0.386 pF. Connecting the π section to the node C and D in the Figure 4-14 and fine tuning the value of C, the performance is shown in Figure 4-22 with $C = 0.26$ pF. The performance will be further improved by tuning lengths of coupled lines due to the asynchronously tuned property.
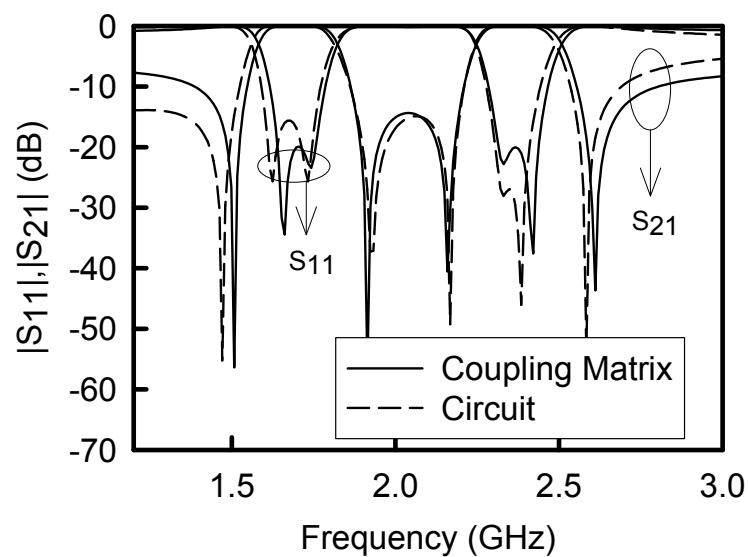
Figure 4-22 The performance of the synthesized circuit in example 1.

For the microstrip implementation, the interdigital capacitor is used to replace the capacitor type π section [142]. The final schematic and circuit photograph are shown in Figure 4-23 with dimensions listed in Table 4.5.
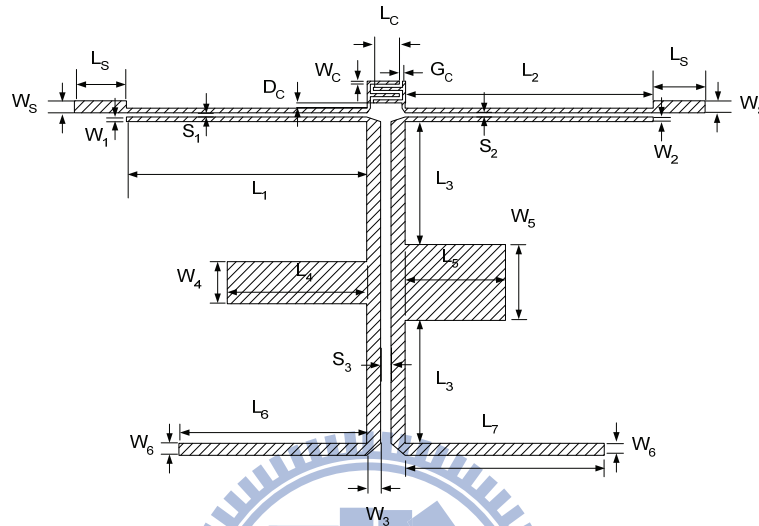
Figure 4-23 The schematic layout of the two-mode dual-band filter in example 1.

Table 4.5 The Dimensions in Figure 4-23 (Unit: *mm*)

W_S	W_1	W_2	W_3	W_4	W_5	W_6	W_C
0.575	0.225	0.225	0.675	2.025	3.650	0.575	0.150
L_S	L_1	L_2	L_3	L_4	L_5	L_6	L_7
2.500	11.550	11.925	6.725	6.700	4.825	9.025	9.575
L_C	S_1	S_2	S_S	G_C	D_C		
1.250	0.200	0.200	0.500	0.150	0.250		

Figure 4-24 shows the circuit photograph, and Figure 4-25 shows the simulated and measured performances and the corresponding group delays. The EM simulator Sonnet is used to efficiently provide the simulated results. Here the inter-digital capacitor is used to produce the source/load coupling, so that two quadruplet coupling schemes, S-1°-2°-L-S and S-1^e-2^e-L-S, are presented to introduce the upper and lower sideband transmission zeros in each passband. Two back-to-back E-shaped resonators contribute two passbands,

and each passband is governed by either even-mode or odd-mode. By two-mode operation of the E-shaped resonator, the coupling scheme shown in Figure 4-9 (b) can be achieved successfully. The measured result agrees well with the simulated performance, hence the proposed design flow is validated well.
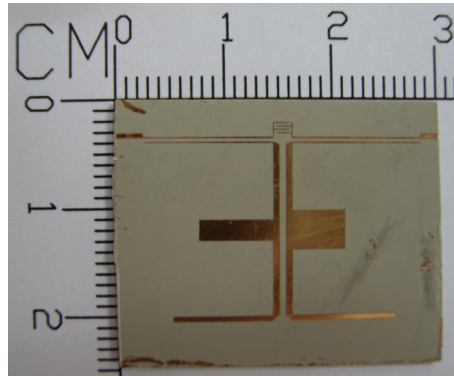
Figure 4-24 The circuit photograph of the two-mode dual-band filter in example 1.
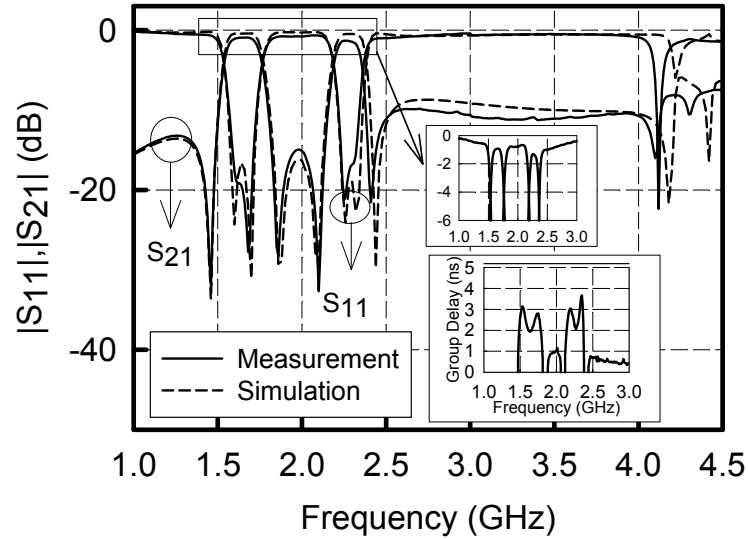
Figure 4-25 Measured and simulated performances and group delay of the two-mode dual-band filter in example 1.

4.4.2 Example 2: Sixth-order Two-mode Dual-band Bandpass Filter

To validate the ability of the proposed method for high order two-mode dual-band filter, here a sixth-order two-mode dual-band filter is used. The performance of the sixth-order two-mode dual-band bandpass filter is also determined by the analytical coupling matrix synthesis procedure in Chapter 2. The relative error can be obtained by the lines with square symbol in Figure 4-11. In this example, we choose $\Delta^{odd}/\Delta^{even} = 1.3$ and f_o = 0.79f_e, so that the relative error is within 0% ~ -7%. Here we choose f_o = 1.79 GHz and f_e = 2.265 GHz. The settings for the synthesis procedure are as follows: The first passband central frequency is firstly shifted from 0 to -0.738 rad/s and the multi-band lowpass domain bandwidth is 0.515 rad/s in the lowpass domain. Similarly, the second passband central frequency is shifted from 0 to 0.797 rad/s and the multi-band lowpass domain bandwidth is 0.396 rad/s in the lowpass domain. Both filters are the third-order filters with return loss of 15 dB. After parallel addition of two filtering functions, the lowpass domain response of the dual-band filter is shown in Figure 4-26 and the coupling scheme is shown in Figure 4-9 (c). The corresponding coupling matrix is listed in Table 4.6. The six-pole dual-band filter is then transformed to the bandpass domain with the central frequency of 2GHz and bandwidth of 30%.
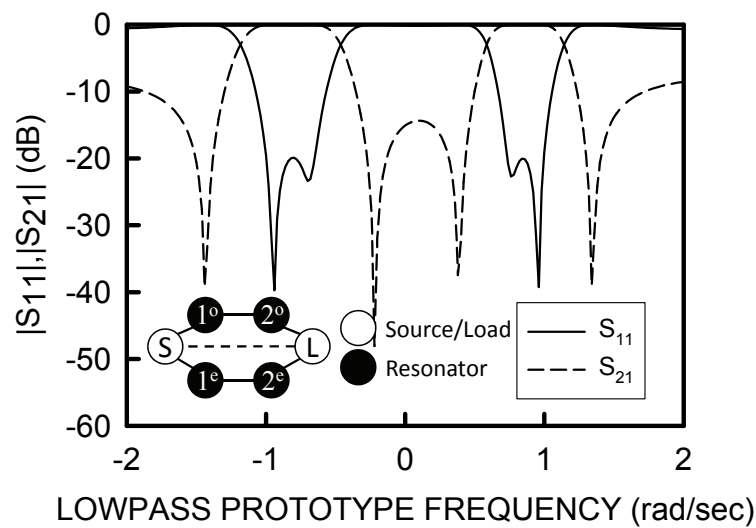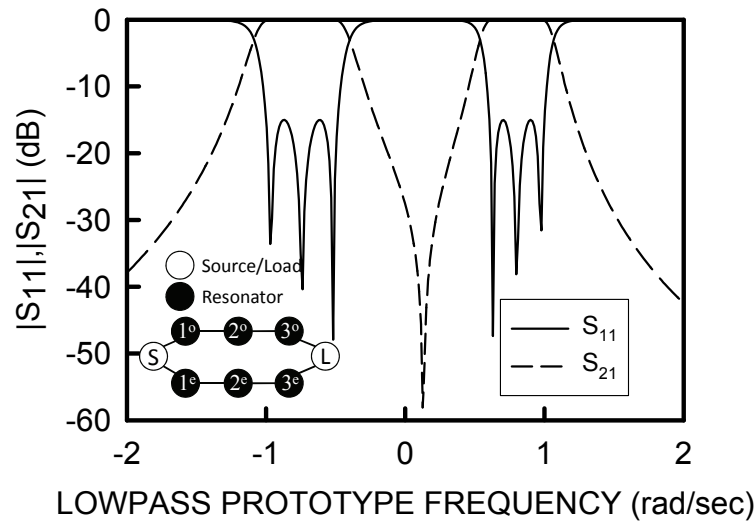
Figure 4-26 The lowpass response and the coupling scheme for example 2.

Table 4.6 The Coupling Matrix for Dual-band Filter in Example 2

	S	1	2	3	4	5	6	L
S	0.0	0.4783	0.0	0.0	0.4214	0.0	0..0	0.0
1	0.4783	0.7689	0.2247	0.0	0.0	0.0	0.0	0.0
2	0.0	0.2247	0.7435	0.2247	0.0	0.0	0.0	0.0
3	0.0	0.0	0.2247	0.7689	0.0	0.0	0.0	0.4783
4	0.4214	0.0	0.0	0.0	-0.8282	0.1729	0.0	0.0
5	0.0	0.0	0.0	0.0	0.1729	-0.8025	0.1729	0.0
6	0.0	0.0	0.0	0.0	0.0	0.1729	-0.8282	0.4214
L	0.0	0.0	0.0	0.4783	0.0	0.0	0.4214	0.0

Before applying the proposed method to analyze the sixth-order two-mode dual-band filter, the circuit layout used in this example is circuit A in Figure 4-27. First phase is to determine the values of J inverter. The coupling path of odd-mode analysis is S-1°-2°-3°-L of the coupling scheme in Figure 4-9 (c). The initial E_1, E_3, and E_4 are 60°, and E_2 and E_5 are 30°. Hence the values of J inverters can be calculated by (3-6), (3-7), and (4-1) with $M_{S,1}^o$, $M_{1',2'}^o$, $M_{2',3'}^o$, and $M_{3',L}^o$, and the calculated Z_{oe} and Z_{oo} are listed in Table 4.7. After determining the Z_{oe} and Z_{oo}, the second phase is to do the even-mode analysis. The central

frequencies of these two passbands are 1.79 and 2.265 GHz, such that the $Z_{S,6}$ is 15 Ω, E_6 is 53.5750° based on $M_{S,1}{}^e$, $Z_{S,7}$ is 29.3353 Ω, E_7 is 59.3250° based on $M_{2,3}{}^e$, and $Z_{S,8}$ is 15 Ω, E_8 is 53.5750° based on $M_{3,L}{}^e$ by (4-3) and (4-4). The performance can be improved due to the asynchronously tuned property. By slightly tuning the lengths, E_1 is 59°, E_2 is 31°, E_3 is 58.5°, E_4 is 61.5°, E_5 is 30.5°, E_6 is 53.5°, E_7 is 71°, and E_8 is 52.5°. The response of the synthesized circuit is illustrated in Figure 4-28. As we mention previously, the circuit A and circuit B in Figure 4-15 will have 180 degree out-of-phase. To validate the separation enhancement, the performances of circuit A and B in Figure 4-27 are analyzing without changing values of design parameters and they are presented in Figure 4-29. The S_{11} are similar, but the rejection between two passbands is better in the circuit A than that in the circuit B.
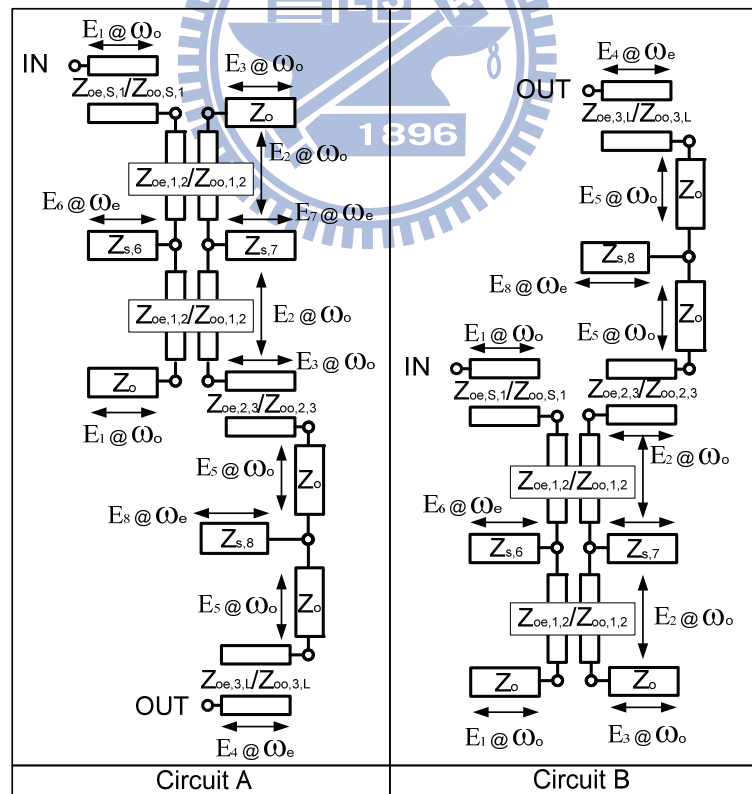
Figure 4-27 The circuit schematic of two-mode dual-band filter in example 2.

Table 4.7 The Calculated Impedances for the Odd-mode Analysis in Example 2.

	$M_{S,1}^{o}$	$M_{1^o,2^o}$	$M_{2^o,3^o}$	$M_{3^o,L}$
J	0.0066	0.0011	0.0021	0.0066
Z_{oe}	77.1181	56.7306	56.8866	77.1181
Z_{oo}	37.7917	44.4001	44.6139	37.7917
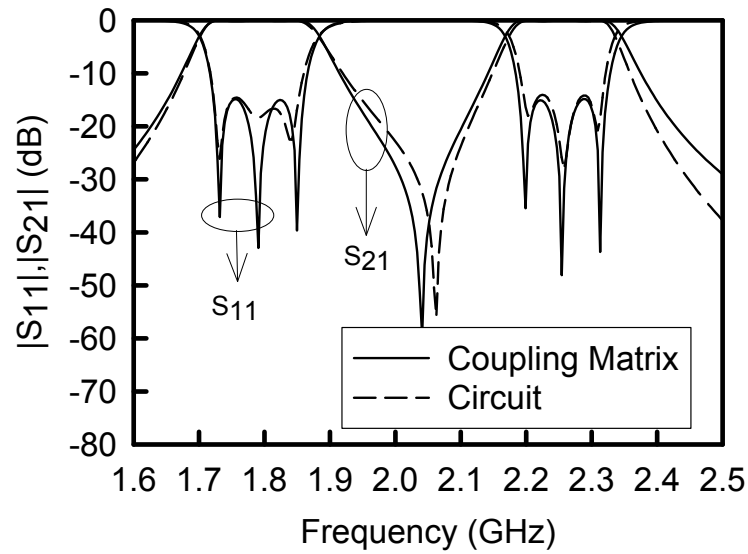
Figure 4-28 The performance of the synthesized circuit in example 2.
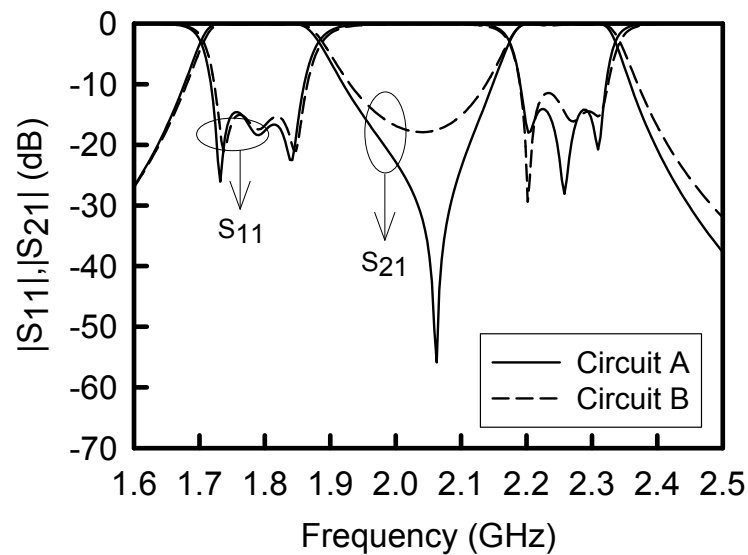
Figure 4-29 The performance of circuit A and circuit B in example 2.

For the microstrip implementation, the final layout is shown in Figure 4-30 and the

circuit photograph is shown in Figure 4-31 with dimensions listed in Table 4.8. The measured and simulated results are shown in Figure 4-32.
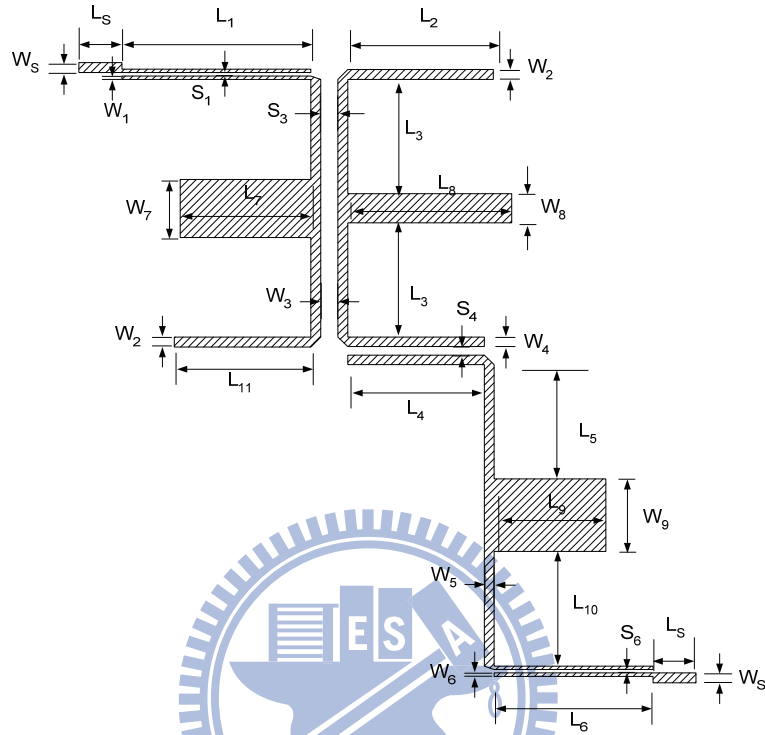
Figure 4-30 The layout of the two-mode dual-band filter in example 2.
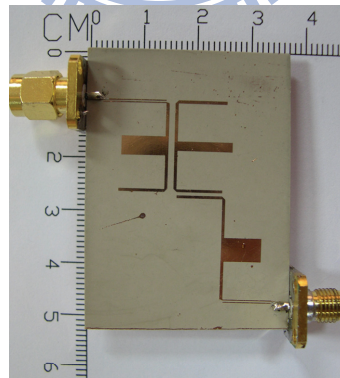
Figure 4-31 The circuit photograph of the two-mode dual-band filter in example 2.

Table 4.8 The Dimensions in Figure 4-31 (Unit: *mm*)

W_S	W_1	W_2	W_3	W_4	W_5	W_6	W_7
0.575	0.200	0.575	0.575	0.550	0.575	0.2	3.375
W_8	W_9	L_S	L_1	L_2	L_3	L_4	L_5
1.700	4.225	2.500	11.000	8.475	6.650	7.950	6.650

L_6	L_7	L_8	L_9	L_{10}	L_{11}	S_1	S_3
9.250	7.600	9.550	6.500	6.675	7.950	0.200	1.000
S_4	S_6						
0.500	0.200						
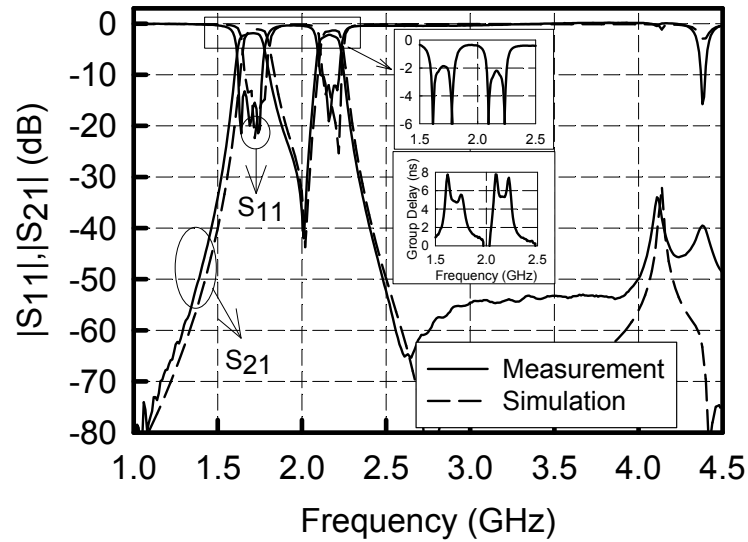
Figure 4-32 Measured and simulated performances and group delay of the two-mode dual-band filter in example 2.

4.5 Conclusion

The novel analytical approach has been presented to design two-mode dual-band filters. Two examples with different filter orders have been implemented to show the feasibility of the method. By using these configurations and requested coupling matrices, even- and odd-mode analysis of E-shaped resonators have been used to determine the circuit parameters. Back-to-back E-shaped resonators have been analyzed to show the out-of-phase property by coupling at the specific edge. This out-of-phase property is used to enhance the filter selectivity. The transmission zeros are implemented to achieve the sharp rollpff. With the coupling-matrix-based synthesis of two-mode dual-band filter

design, the compact size, flexible responses, good performances and quick design procedure are achieved.
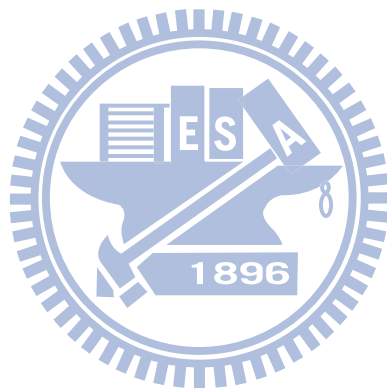
Chapter 5

Two-mode Tri-band and Quad-band Filter Design with Close

Adjacent Passbands Using E-shaped Resonators

5.1 Introduction

Dual-path topology has been validated for the convenient coupling scheme for dual-band filter design in the microstrip implementation. Based on the idea, that is one path governs one passband, the tri-path and quad-path topologies here are proposed for the tri-band and quad-band filters design. The filter consisted of the parallel-coupled lines discussed in Chapter 3 will be limited in tri-band and quad-band filter design by its spatial limitation, that is, the coupling between adjacent paths will ruin the filter performance due to the close distance. Moreover, the size of such kind of filters is large.

The two-mode E-shpaed resonator proposed in Chapter 4 has been proposed to used in dual-band filter design with small size and is valid in microstrip implementation. Furthermore, the dual-band coupling scheme has been demonstrated the validation in illustrating the coupling effects in this two-mode dual-band filter. Due to these properties, in this chapter the E-shaped resonators are proposed to be applied in tri-band and quad-band filter design using the tri-path and quad-path topologies.

Based on the analysis in Chapter 4, the design parameters can be extracted analytically. Moreover, by grouping two adjacent passbands, the tri-band and quad-band performances are then divided into two groups in each design. In each group, the filter with dual-band performance can be synthesized analytically using E-shaped resonator. Finally, to combine these two synthesized filter, double diplexing configuration is used with some

fine tunes, and then the tri-band and quad-band filter can be obtained.

5.2 Double Diplexing Configuration

The double diplexing configuration for dual-band filter design is shown in Figure 3-15. To apply the configuration for the tri-band and quad-band filter, Figure 5-1 shows the schematic. The design equation will be modified as follows:

$$\mathrm{Im}\big[Y_1\big]_{f\in(f_3,f_4)} = 0,$$
$$\mathrm{Im}\big[Y_2\big]_{f\in(f_1,f_2)} = 0. \tag{5-1}$$

The above equation needs to be satisfied within an interval of frequencies, such that the configuration has bandwidth limitation in each path. Hence the passbands in each path should be close enough to each other. Moreover, in order to cover the dual-band bandwidth in each path, three transmission lines with characteristic impedance Z_A, Z_B, and Z_C and electrical length θ_A, θ_B, and θ_C are used as variables to meet the specifications.
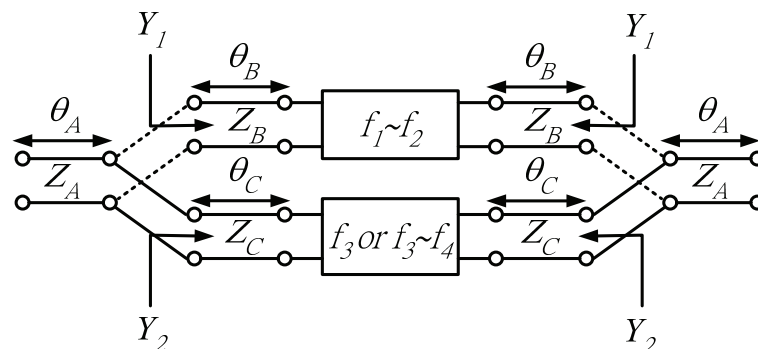
Figure 5-1 Double diplexing configuration for tri-band and quad-band filter design.

5.3 Tri-band and Quad-band Filter Synthesis

To take the quad-band filter as example, the quad-band coupling matrix is firstly synthesized. Next, grouping it as two dual-band filters from the frequency domains and synthesize each dual-band filter with the filter topology shown in Figure 5-2. Finally, the double-diplexing configuration is applied to connect two dual-band filters to form the quad-band filter. For the tri-band filter, substitute one of the dual-band filters to be a single-band filter by changing E-shape two-mode resonators to hair-pin single-mode resonators. For the practical implementation, a 0.635-mm-thich Rogers RT/Duroid 6010 substrate, with a relative dielectric constant 10.2 and a loss tangent of 0.0021.
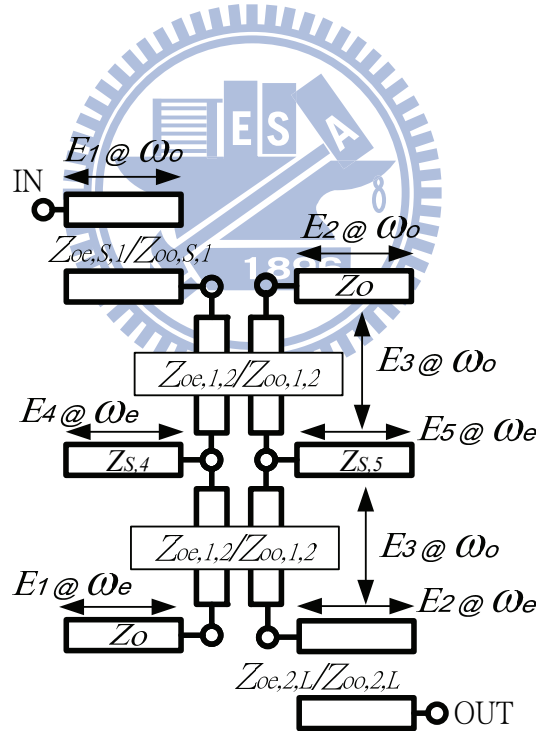
Figure 5-2. Proposed unit cell for the two-mode dual-band filter.

5.3.1 Example 1: Tri-band Filter

In the tri-band filter design, the tri-band coupling matrix is synthesized using the

proposed multi-band coupling matrix synthesis. The settings are shown in Table 5.1, and coupling matrix is shown in Table 5.2 with corresponding coupling scheme shown in Figure 5-3. For the bandpass filter design, the central frequency is 1.92 GHz and fractional bandwidth is 56.2%, the performance of the coupling matrix is shown in Figure 5-4.

Table 5.1 Setting of Tri-band Coupling Matrix Synthesis

Passband f_c (rad/s)	δ	RL (dB)	Circuit Performances		
			f_c (GHz)	RL (dB)	Bandwidth
-0.825	0.35	15	1.523	16	9.77%
0	0.3	15	1.935	19.5	9.11%
0.825	0.35	15	2.417	16	9.81%

Table 5.2 Coupling Matrix of the Tri-band Filter

	S	1	2	3	4	5	6	L
S	0.0	0.4430	0.0	0.3796	0.0	0.4435	0.0	0.0
1	0.4430	0.8807	0.2211	0.0	0.0	0.0	0.0	0.0
2	0.0	0.2211	0.8807	0.0	0.0	0.0	0.0	-0.4430
3	0.3796	0.0	0.0	0.0	0.1866	0.0	0.0	0.0
4	0.0	0.0	0.0	0.1866	0.0	0.0	0.0	0.3796
5	0.4435	0.0	0.0	0.0	0.0	-0.8806	0.2215	0.0
6	0.0	0.0	0.0	0.0	0.0	0.2115	-0.8806	-0.4435
L	0.0	0.0	-0.4430	0.0	0.3796	0.0	-0.4435	0.0
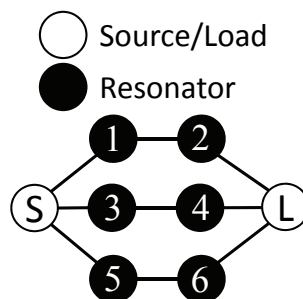
Figure 5-3 The coupling scheme of the tri-band filter in example 1.
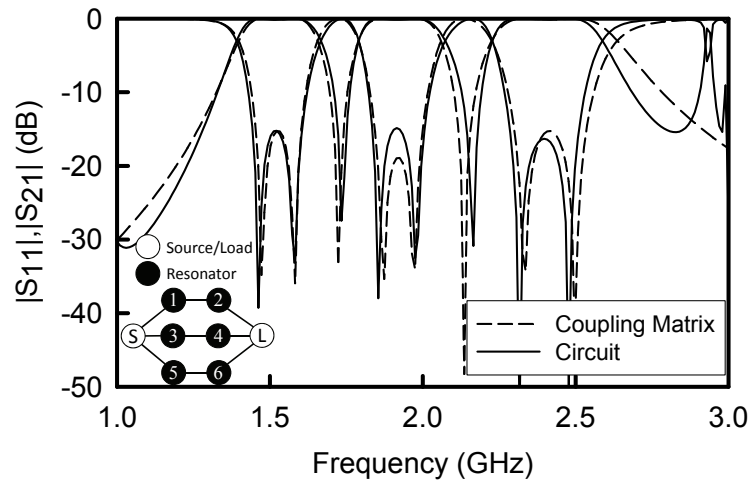
Figure 5-4 Performances of the coupling matrix and synthesized circuit in example 1.

The central frequencies of three passbands are 1.533, 1.92, and 2.417 GHz, and their return losses are 15.01, 19.33 and 15 dB, with individual bandwidth 9.21%, 8.37% and 9.63%. To implement this filter, the two-mode dual-band filter is used to govern the first two passbands (i.e., the resonators numbered #1, #2, #3, and #4) and a single bandpass filter (i.e., resonators numbered #5 and #6) is used to govern the third passband. The synthesized variables are listed in Table 5.3 and Table 5.4. To connect these two filters, the double-diplexing configuration is design at 1.92 GHz with Z_A, Z_B, and Z_C are 39 Ω, 41 Ω, and 72 Ω, and E_A, E_B, and E_C are 96°, 96°, and 136°. The synthesized filter performance is also shown in Figure 5-4.

Table 5.3 Synthesized Z_{oe} and Z_{oo} Based on Coupling Matrix in Table 5.2

	$M_{S,1}$	$M_{1,2}$	$M_{2,L}$	$M_{S,5}$	$M_{5,6}$	$M_{6,L}$
Z_{oe} (Ω)	88.95	63.16	88.95	88.95	63.16	88.95
Z_{oo} (Ω)	36.79	40.56	36.79	36.79	40.56	36.79

Table 5.4 Synthesized Electrical Lengths and Stub Impedances Based on Coupling Matrix in

Table 5.2

Passband #1 & #2	f_o = 1.533 GHz, f_e = 1.92 GHz						
Design Variable	$Z_{S,4}$ (Ω)	$Z_{S,5}$ (Ω)	E_1	E_2	E_3	E_4	E_5
Synthesized	12.877	12.877	60°	60°	30°	47.09^o	47.09^o
Fine tuned	13	13	58°	58°	33°	47°	47°
Passband # 3	f_o = 2.417 GHz						
Design Variable	E_1	E_2	E_3				
Synthesized	60°	60°	30°				
Fine tuned	60°	60°	28°				

For microstrip implementation, the layout is shown in Figure 5-5 with dimensions listed in Table 5.5, and the circuit photograph is shown in Figure 5-6. Figure 5-7 shows the simulated and measured results.

Figure 5-5 The layout of the tri-band filter.

Table 5.5 Dimensions of the Tri-band Filter (Unit: *mm*)

W_S	L_S	W_{feed}	L_{feed}	W_u	L_{U1}	L_{6_2}	L_{U2}
0.58	2.5	1.2	13.13	0.50	7.53	12.15	15.33
L_{U3}	L_{U4}	W_D	L_{D1}	L_{D2}	W_{1Z}	L_{D3}	L_{D4}
12.00	10.85	1.00	2.85	10.13	4.48	6.93	6.05
W_1	S_1	L_{1_1}	L_{1_2}	L_Z	W_Z	W_2	S_2
0.20	0.20	8.75	5.00	7.30	0.58	0.28	0.43
L_2	W_3	S_3	L_{3_1}	L_{3_2}	W_4	S_4	L_{4_1}
6.40	0.20	0.20	8.20	5.78	0.20	0.20	13.45
L_{4_2}	W_5	S_5	L_5	W_6	S_6	L_{6_1}	
11.48	0.28	0.43	3.98	0.20	0.20	12.78	
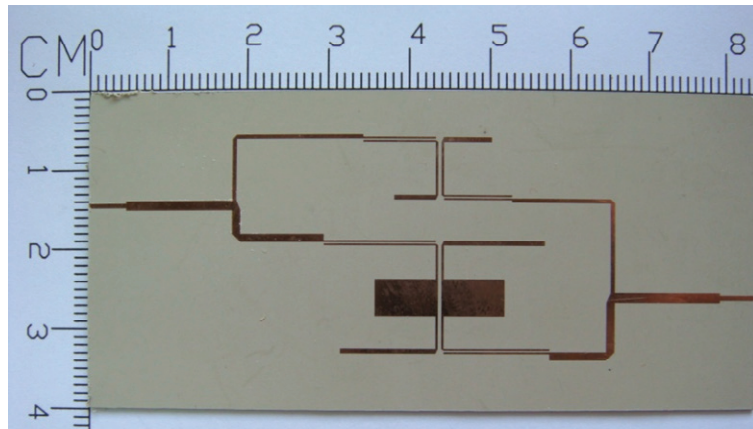
Figure 5-6 The circuit photograph of the tri-band filter in example 1.
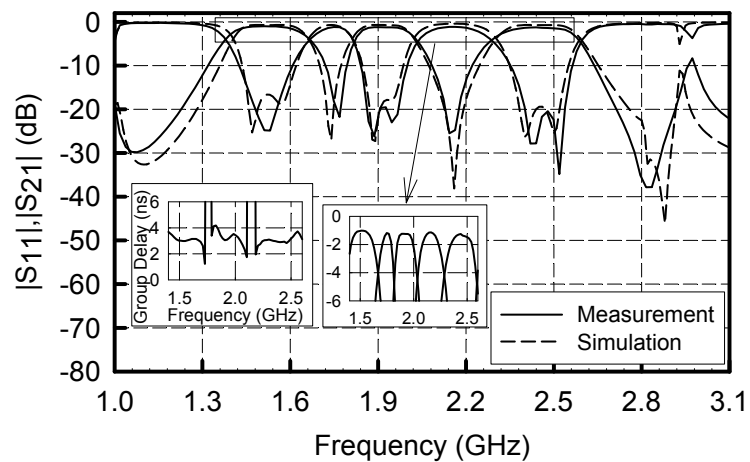
Figure 5-7 The simulated and measured results of the tri-band filter.

5.3.2 Example 2: Quad-band Filter

In the quad-band filter design, the quad-band coupling matrix synthesized using the proposed method in Chapter 2. The settings are shown in Table 5.6, and corresponding coupling matrix is shown in Table 5.7 with corresponding coupling matrix shown in Figure 5-8. The synthesized values of $M_{4,L}$, $M_{L,4}$, $M_{8,L}$, and $M_{L,8}$, are all positive based on the settings in Table 5.6. In order to generate two transmission zeros between passband #1 and #2 and passband #3 and #4, these four components of the coupling matrix should be set to be negative, as shown in Table 5.7.

Table 5.6 Setting of Quad-band Coupling Matrix Synthesis.

Passband f_c (rad/s)	δ	Circuit Performances		
		f_c (GHz)	RL (dB)	Bandwidth
-0.8990	0.2	1.286	14.86	6.97%
-0.2929	0.1	1.663	20.47	4.27%
0.2929	0.17	2.176	16.97	6.49%
0.8990	0.12	2.809	15.88	5.02%

*# of poles = 2, # of zeros = 0 & RL = 13 dB in each passband

Table 5.7 Coupling Matrix of the Quad-band Filter in Example 2.

	S	1	2	3	4	5	6	7	8	L
S	0.0	0.3143	0.0	0.2700	0.0	0.3056	0.0	0.2791	0.0	0.0
1	0.3143	0.9240	0.1142	0.0	0.0	0.0	0.0	0.0	0.0	0.0
2	0.0	0.1142	0.9240	0.0	0.0	0.0	0.0	0.0	0.0	0.3143
3	0.2700	0.0	0.0	0.2975	0.0853	0.0	0.0	0.0	0.0	0.0
4	0.0	0.0	0.0	0.0853	0.2975	0.0	0.0	0.0	0.0	-0.2700
5	0.3056	0.0	0.0	0.0	0.0	-0.3208	0.1106	0.0	0.0	0.0
6	0.0	0.0	0.0	0.0	0.0	0.1106	-0.3208	0.0	0.0	0.3056
7	0.2791	0.0	0.0	0.0	0.0	0.0	0.0	-0.9411	0.0881	0.0
8	0.0	0.0	0.0	0.0	0.0	0.0	0.0	0.0881	-0.9411	-0.2791
L	0.0	0.0	0.3143	0.0	-0.2700	0.0	0.3056	0.0	-0.2791	0.0
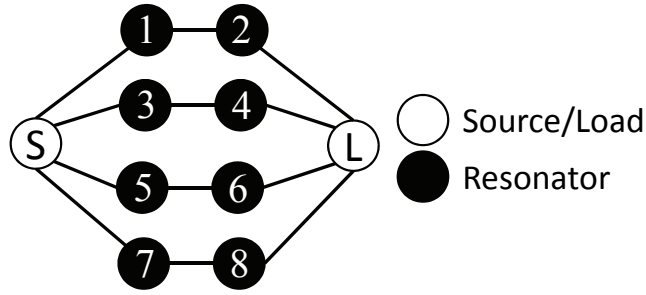
Figure 5-8. The coupling scheme for the quad-band filter in example 2.

For the bandpass filter design, the central frequency is 1.9 GHz and fractional bandwidth is 87.4%, the performance is shown in Figure 5-9, and the synthesized central frequencies, return loss and fractional bandwidth are shown in Table 5.6. To implement this filter, one two-mode dual-band filter is used to govern the first two passbands, while the other one is used to govern the third and fourth passbands. The synthesized variables are listed in Table 5.8 and Table 5.9. To connect these two filters, the double-diplexing configuration is designed at 2 GHz with Z_A, Z_B, and Z_C are 43 Ω, 54 Ω, and 52 Ω, and E_A, E_B, and E_C are 99°, 40°, and 125°. The circuit performance is shown in Figure 5-9.
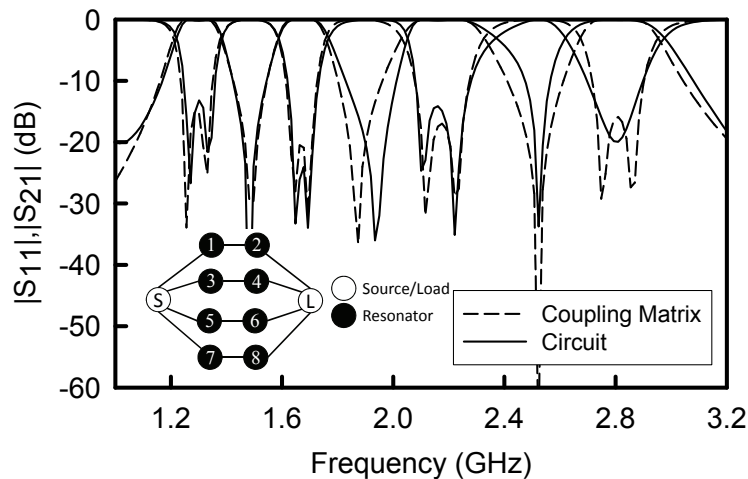
Figure 5-9 Performances of the coupling matrix and synthesized circuit.

Table 5.8 Synthesized Z_{oe} and Z_{oo} Based on Coupling Matrix in Table 5.7.

	$M_{S,1}$	$M_{1,2}$	$M_{2,L}$	$M_{S,5}$	$M_{5,6}$	$M_{6,L}$
Z_{oe} (Ω)	81.74	60.47	81.74	80.53	60.10	80.53
Z_{oo} (Ω)	37.20	42.02	37.20	37.33	42.25	37.33

Table 5.9 Synthesized Electrical Lengths and Stub Impedances

Based on Coupling Matrix in Table 5.7

Passband #1 & #2	f_o = 1.286 GHz, f_e = 1.663 GHz						
Design Variable	$Z_{S,4}$ (Ω)	$Z_{S,5}$ (Ω)	E_1	E_2	E_3	E_4	E_5
Synthesized	20.78	20.78	60°	60°	30°	59.17^o	59.17^o
Fine tuned	17	17	62°	62°	30°	51°	51°
Passband # 3	f_o = 2.176 GHz, f_e = 2.809 GHz						
Design Variable	$Z_{S,4}$ (Ω)	$Z_{S,5}$ (Ω)	E_1	E_2	E_3	E_4	E_5
Synthesized	10.94	10.94	60°	60°	30°	41.70^o	41.70^o
Fine tuned	12	12	60°	60°	28°	49°	49°
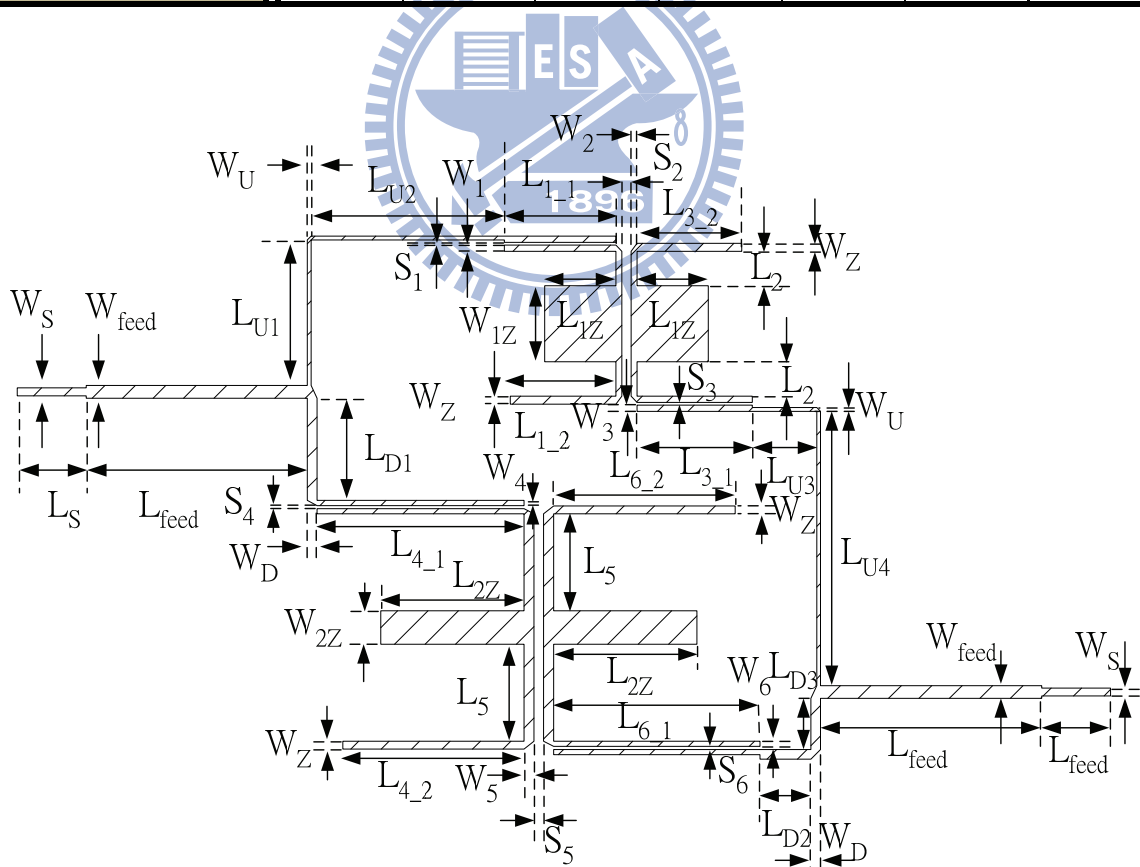
Figure 5-10 The layout of the quad-band filter

For the microstrip implementation, the layout is shown in Figure 5-10 with dimensions listed in Table 5.10. The circuit photograph is shown in Figure 5-11, and the simulated and measured results are shown in Figure 5-12
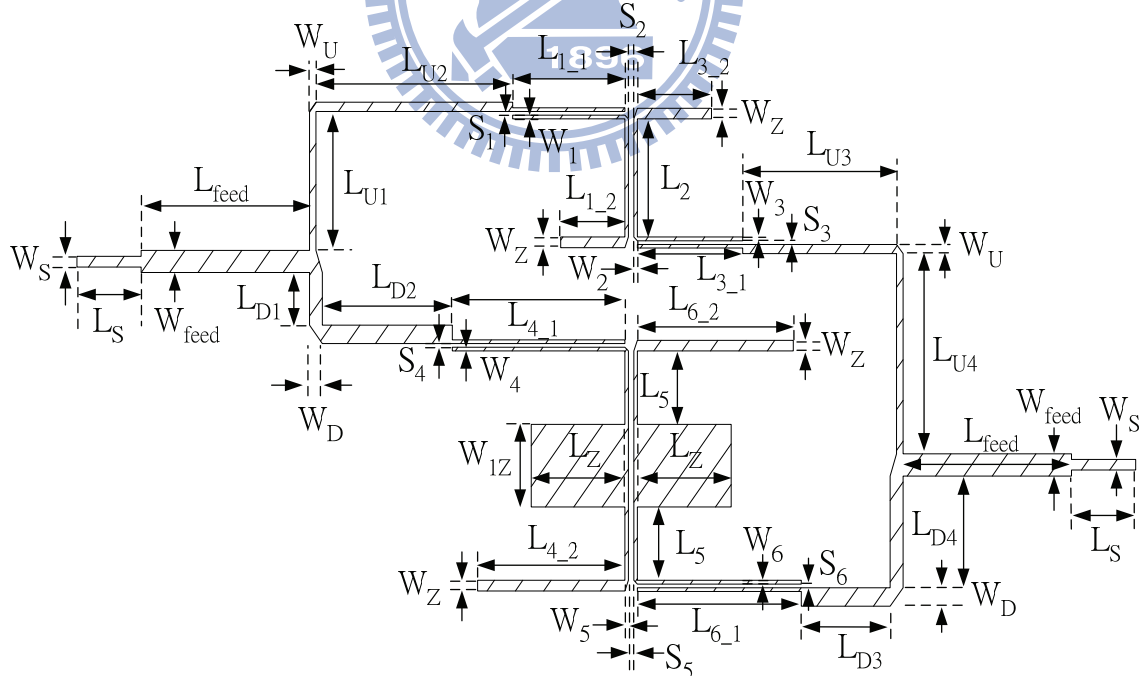
Table 5.10 Dimensions of the Quad-band Filter (Unit: *mm*)

W_S	L_S	W_{feed}	L_{feed}	W_u	L_{U1}	W_{1Z}	L_{U2}
0.58	5.00	0.93	16.13	0.28	10.55	5.50	14.03
L_{U3}	L_{U4}	W_D	L_{D1}	L_{D2}	L_{1Z}	L_{D3}	W_1
4.68	19.88	0.70	7.40	3.75	5.18	3.75	0.45
S_1	L_{1_1}	L_{1_2}	W_Z	W_{2Z}	W_2	S_2	L_2
0.20	8.10	7.68	0.58	2.43	0.43	0.68	2.50
W_3	S_3	L_{3_1}	L_{3_2}	L_{2Z}	W_4	S_4	L_{4_1}
0.45	0.20	8.38	7.60	10.40	0.38	0.23	15.03
L_{4_2}	W_5	S_5	L_5	W_6	S_6	L_{6_1}	L_{6_2}
13.15	0.73	0.70	7.03	0.38	0.23	14.98	13.18
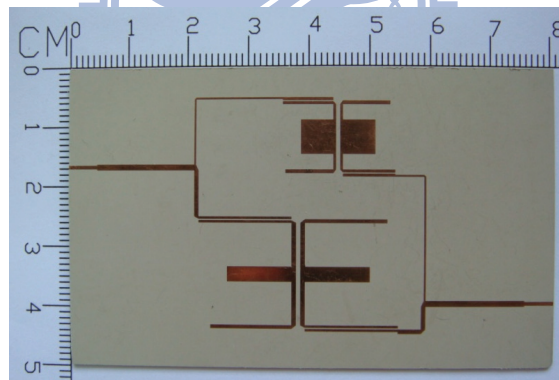
Figure 5-11 The circuit photograph of the quad-band filter in example2.
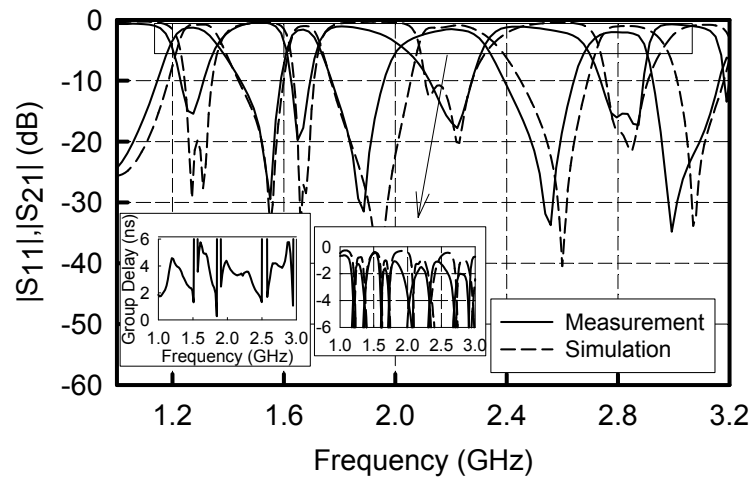
Figure 5-12 The simulated and measured results of the quad-band filter.

5.4 Conclusion

A coupled-matrix based semi-analytic procedure, i.e., analytic synthesis for the two-mode dual-band filters and then connecting them together by the double-diplexing configuration with slight tuning, for tri-band and quad-band filter design has been provided. For tri-band and quad-band filter, two examples with tri-band and quad-band filters are shown to validate the procedure and the measured results show the good agreement with the simulated performances. The proposed procedure in tri-band and quad-band filter design has shown the properties of good performance, semi-analytic synthesized method and quick design procedure.

Chapter 6

Conclusion and Future Work

6.1 Conclusion

This dissertation describes a design flow for the dual-band, tri-band and quad-band filter. Based on the specifications, the corresponding coupling matrix of the requested filter is synthesized. For the aspect of the filter realization, the multi-path coupling scheme is analyzed and validated for its convenient in multi-band filter design. The analytical filter synthesis procedures, which are based on parallel-coupled line or two-mode E-shaped resonator, are then applied to extract the design parameters based on the corresponding coupling matrix with the multi-path topology. The measured results show the well agreement with the simulated responses.

In chapter 2, a novel multi-band coupling matrix synthesis for multi-band filter design is developed. Based on the well-known single-band coupling matrix synthesis, the extracted polynomials are then shifted to the specific central frequencies and shrank to the specific bandwidths. After parallel addition, the multi-band filtering function and corresponding polynomials can be obtained. Moreover, the prescribed transmission zeros can be placed to the specific locations once the transmission zeros in each passband are assigned carefully.

In chapter 3, the single-path and dual-path coupling schemes for the dual-band filter design are analyzed. The dual-path coupling scheme has been validated to be convenient in dual-band filter design, Cross-coupling paths are designed in each passband in order to generate the specific transmission zeros. Tri-section coupling topology is used to generate

one transmission zero above or below the corresponding central frequency in one passband, while the quadruplet coupling scheme is used to generate two transmission zeros above and below the corresponding central frequency. Moreover, the dual-path coupling topology provides an intrinsic transmission zero, which can improve the isolation between adjacent passbands.

The dual-band filters with two-mode E-shaped resonators are analyzed and designed based on the dual-path coupling schemes. The detail derivations of the analytical synthesized procedure are described in chapter4. The 180-degree out-of-phase property also shows its advantage in the isolation improvement between two adjacent passbands. The limitation in back-to-back E-shaped resonators has also been discussed and find out the feasible design based on the specific coupling scheme.

In the chapter 5, the tri-band and quad-band filter designs are realized based on the E-shaped resonator and double-diplexing configuration. By grouping the tri-band or quad-band into two categories, one is a dual-band characteristic, and the other is a single-band characteristic for the tri-band filter design or a dual-band characteristic for the quad-band filter design. And then, the double diplexing configuration is used to connect the two filters in these two categories.

6.2 Future Work

In this dissertation, the double-diplexing configuration is widely used, but there is no analytical approach to determine the design parameters. Such an approach can be studied in the future to make the whole design more efficient. Moreover, based on the synthesized multi-band coupling matrix, some specific coupling scheme can be studied for its property in transmission zeros generation for the multi-band filter design. Moreover, some specific

two-mode resonators can be analyzed based on the coupling matrix and provide a systematic guide line in multi-band filter design. To use the diagnosis technique [143] to fine-tuning the EM performance of dual-band and multi-band filter, a automatic tuning can be achieved via Matlab-EM co-simulation.

To make the multi-band design flow more easy and convenient, a user-interface can be developed in Matlab. Users can enter the specifications, such as number of passband, filter order, return loss, and transmission zeros in each passband, and then they can describe the user-specific coupling scheme, and then the corresponding coupling matrix will be extracted. Moreover, while choose the prescribed layout, the initial design parameters can be obtained and then be optimized by the Matlab-EM co-simulation solver. Thus, if we can complete all above steps, the requested layout will then be generated automatically. It will provide filter designers a fast and efficient design procedure.
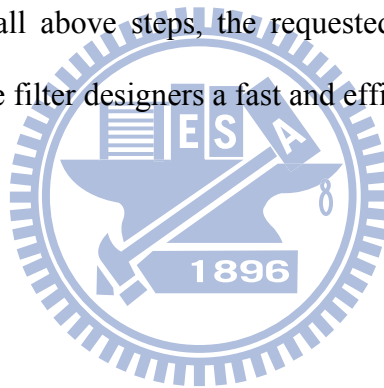
References

[1] J. W. Baik, L, Zhu, Y. S. Kim, "Dual-mode dual-band bandpass filter using balun structure for single substrate configuration," *IEEE Microw. Wireless Compon. Lett.*, vol. 20, no. 11, pp. 613-615, Nov. 2010.

[2] E. E. Djoumessi and K. Wu, "Multilayer dual-mode dual-bandpass filter," *IEEE Microw. Wireless Compon. Lett.*, vol. 19, no. 1, pp. 21-23, Jan. 2009.

[3] F. C. Chen and Q. X. Chu, "Novel multistub loaded resonator and its application to high-order dual-band filters," *IEEE Trans. Microw. Theory Tech.*, vol. 58, no. 6, pp. 1551–1556, Dec. 2010.

[4] X. H. Wu, Q. X. Chi, and L. Fan, "Compact dual-band bandpass filter with controllable bandwidths," in *International Conference on Microwave and Millimeter Wave Technology*, Chengdu, China, May 2010, pp. 1305–1307.

[5] S. Lee and Y. Lee, "A uniform coupled-line dual-band filter with different bandwidths," *IEEE Microw. Wireless Compon. Lett.*, vol. 20, no. 10, pp. 545-547, Oct. 2010.

[6] S. Lee and Y. Lee, "A planar dual-band filter based on reduced-length parallel coupled lines," *IEEE Microw. Wireless Compon. Lett.*, vol. 20, no. 1, pp. 16-18, Jan. 2010.

[7] C. X. Zhou, Y. X. Guo, S. L. Yan, and Z. L. Wang, "Dual-band UWB filter with LTCC technology," *Electron. Lett.*, vol. 47, no. 22, pp. 1230-1232, Oct. 2011.

[8] X. Y. Zhang, C. H. Chan, Q. Xue, and B. J. Hu, "Dual-band bandpass filter with controllable bandwidths using two coupling paths," *IEEE Microw. Wireless Compon. Lett.*, vol. 20, no. 11, pp. 616-618, Nov. 2010.

[9] L. Wang, C. Zhao, C. Li, and X. Lin, "Dual-band bandpass filter using stub loaded resonators with multiple transmission zeros," in *9th International Symposium on Antennas Propagation and EM Theory*, Guangzhou, China, Nov. 2010, pp. 1208–1211.

[10] H. W. Deng, Y. J. Zhao, X. S. Zhang, W. Chen, and J. K. Wang, "Compact and high selectivity dual-band dual-mode microstrip BPF with single stepped-impedance resonator," *Electron. Lett.*, vol. 47, no. 5, pp. 326-327, Mar. 2011.

[11] H. W. Deng, Y. J. Zhao, L. Zhang, X. S. Zhang, and W. Zhao, "Dual-band BPF with DSIR and TSIR," *Electron. Lett.*, vol. 46, no. 17, pp. 1205-1206, Aug. 2010.

[12] W. S. Chang and C. Y. Chang, "Analytical design of microstrip short-circuit terminated stepped-impedance resonator dual-band filters," *IEEE Trans. Microw. Theory Tech.*, vol. 59, no. 7, pp. 1730–1739, Jul. 2011.

[13] Z. Yang, L. Zhang, Z. Ma, and X. Yang, "A compact microstrip dual-mode dual-band

filter with source-load coupling," in *China-Japan Joint Microwave Conference*, Hangzhou, China, Apr. 2011, pp. 1–4.

[14] W. P. Liu and Y. W. Tung, "Dual-band stepped-impedance resonant filter with dual-band admittance inverter," in *International Conference on Microwave and Millimeter Wave Technology*, Chengdu, China, May 2010, pp. 1409–1493.

[15] M. L. Chuang, M. T. Wu, and S. M. Tsai, "Dual-band filter design using L-shaped stepped impedance resonators," *IET Microw. Antenna. P.*, vol. 4, no. 7, pp. 855–862, Jul. 2010.

[16] C. H. Tseng and H. Y. Shao, "Design of dual-band net-type bandpass filter," in *IEEE MTT-S Int. Microw. Symp. Dig.*, Anaheim, California, May 2010, pp. 572–575.

[17] M. A. Nikravan and Z. Atlasbaf, "Compact dual-band microstrip bandpass filter using folded linear tapered-line resonator," in *Proc. Asia-Pacific Microw. Conf.*, Yokohama, Japan, Dec. 2010, pp. 1755-1757.

[18] X. S. Zhang, H. W. Deng, L. Zhang, Y. J. Zhao, L. Qiang, "Compact dual-band BPF for GPS and WLAN with two dual-mode stepped impedance resonators," in *Global Mobile Congress*, Shanghai, China, Oct. 2010, pp. 1-3.

[19] T. Jiang, C. Y. Liu, Y. S. Li, and J. Zhang, "A novel compact dual-band micro-strip band-pass filter design," in *International Conference on Wireless Communications and Signal Processing*, Suzhou, China, Oct. 2010, pp. 1-4.

[20] K. S. Chin and J. H. Yeh, "Dual-wideband bandpass filter using short-circuited stepped-impedance resonators," *IEEE Microw. Wireless Compon. Lett.*, vol. 19, no. 3, pp. 155-157, Mar. 2009.

[21] F. Medina and F. Mesa, "Design of a Dual Band-Pass Filter Using Modified Folded Stepped-Impedance Resonators" in *IEEE MTT-S Int. Microw. Symp. Dig.*, Boston, June 2009, pp. 857–860.

[22] Y. C. Chang, C. H. Kao, M. H. Weng, and R. Y. Yang, "Design of the compact dual-band bandpass filter with high isolation for GPS/WLAN applications," *IEEE Microw. Wireless Compon. Lett.*, vol. 19, no. 12, pp. 780-782, Dec. 2009.

[23] R. G. Garcia, J. M. Ferreras, and M. S. Renedo, "Signal-interference stepped-impedance-line microstrip filters and application to duplexers," *IEEE Microw. Wireless Compon. Lett.*, vol. 21, no. 8, pp. 421-423, Aug. 2011.

[24] R. G. Garcia and M. S. Renedo, "Application of generalized bagley-polygon four-port power dividers to designing microwave dual-band bandpass planar filters," in *IEEE MTT-S Int. Microw. Symp. Dig.*, Anaheim, California, May 2010, pp. 580–583.

[25] R. G. Garcia, M. S. Renedo, B. Jarry, J. Lintignat, and B. Barelaud, "A class of microwave transversal signal-interference dual-passband planar filters," *IEEE Microw. Wireless Compon. Lett.*, vol. 19, no. 3, pp. 158-160, Mar. 2009.

[26] M. D. Sindreu, G. Siso, J. Bonache, and F. Martin, "Planar multi-band microwave components based on the generalized composite right/left handed transmission line

concept," *IEEE Trans. Microw. Theory Tech.*, vol. 58, no. 12, pp. 3882–3891, Dec. 2010.

[27] S. Kahng, G. Jang, and J. Anguera, "Metamaterial dual-band bandpass filters using CRLH zero-order-resonators and improving its intermediate stopband," in *4th European Conference on Antennas and Propagation*, Barcelona, Spain, Apr. 2010, pp. 1–3.

[28] M. D. Sindreu, J. Bonache, and F. Martin, "Compact CPW dual-band bandpass filters based on semi-lumped elements and metamaterial concepts," in *Proc. Asia-Pacific Microw. Conf.*, Yokohama, Japan, Dec. 2010, pp. 670-673.

[29] P. Kapitanova, D. Kholodnyak, S. Humbla, R. Perrone, J. Mueller, M. A. Hein, and I. B. Vendik, "Multi-band and tunable multi-band microwave resonators and filters based on cascaded left/right-handed transmission line sections," in *IEEE Eurocon*, Saint-Petersburg, Russia, May 2009, pp. 39-45.

[30] Y. C. Li, H. Wong, and Q. Xue, "Dual-mode dual-band bandpass filter based on a stub-loaded patch resonator," *IEEE Microw. Wireless Compon. Lett.*, vol. 21, no. 10, pp. 525-527, Oct. 2011.

[31] M. Doan and W. Che, "Dual-band bandpass filter using quarter-wavelength resonator with controllable bandwidths and good selectivity," in *International Conference on Advanced Technologies for Communication*, Danang, Vietnam, Aug. 2011, pp. 199-202.

[32] P. H. Deng, H. H. Tung, "Design of microstrip dual-passband filter based on branch-line resonators," *IEEE Microw. Wireless Compon. Lett.*, vol. 21, no. 4, pp. 200-202, Apr. 2011.

[33] C. W. Tang and P. H. Wu, "Design of a planar dual-band bandpass filter," *IEEE Microw. Wireless Compon. Lett.*, vol. 21, no. 7, pp. 362-364, July 2011.

[34] Z. Zhang, Y. C. Jiao, X. M. Wang, and S. F. Cao, "Design of a compact dual-band bandpass filter using opposite hook-shaped resonator," *IEEE Microw. Wireless Compon. Lett.*, vol. 21, no. 7, pp. 359-361, July 2011.

[35] K. S. K. Yeo and M. J. Lancaster, "8 pole high temperature superconductor microstrip dual band bandpass filter design," in *IEEE MTT-S Int. Microw. Symp. Dig.*, Baltimore, June 2011.

[36] X. Liu, L. P. B. Katehi, and D. Peroulis, "Novel dual-band microwave filter using dual-capacitively-loaded cavity resonators," *IEEE Microw. Wireless Compon. Lett.*, vol. 20, no. 11, pp. 610-612, Nov. 2010.

[37] Y. Sung, "Dual-mode dual-band filter with band notch structures," *IEEE Microw. Wireless Compon. Lett.*, vol. 20, no. 2, pp. 73-75, Feb. 2010.

[38] H. W. Liu, L. Shen, Z. C. Zhang, J. S. Lim, D. Ahn, "Dual-mode dual-band bandpass filter using defected ground waveguide" *Electron. Lett.*, vol. 46, no. 13, pp. 895-397, Jun. 2010.

[39] G. L. Dai, Y. X. Guo, and M. Y. Xia, "Dual-band bandpass filter using parallel short-ended feed scheme," *IEEE Microw. Wireless Compon. Lett.*, vol. 20, no. 6, pp. 325-327, June 2010.

[40] C. W. Tang, Y. K. Hsu, and J. W. Wu, "Design of wide dual-passband microstrip bandpass filters with comb-loaded resonators," in *IEEE MTT-S Int. Microw. Symp. Dig.*, Anaheim, California, May 2010, pp. 1700–1703.

[41] X. Luo, H. Qian, J. G. Ma, K. Ma, and K. S. Yeo, "Compact dual-band bandpass filters using novel embedded spiral resonator (ESR)," *IEEE Microw. Wireless Compon. Lett.*, vol. 20, no. 8, pp. 435-437, June 2010.

[42] X. Guan, S. Jiang, L. Shen, H. Liu, G. Li, and D. Xu, "A microstrip dual-band bandpass filter based on a novel admittance inverter," in *International Conference on Microwave and Millimeter Wave Technology*, Chengdu, China, May 2010, pp. 577–580.

[43] Y. H. Cho, H. I. Baek, H. S. Lee, and S. W. Yun, "A dual-band combline bandpass filter loaded by lumped series resonators," *IEEE Microw. Wireless Compon. Lett.*, vol. 19, no. 10, pp. 626-628, Oct. 2009.

[44] M. J. Almalkawi and W. M. Fathelbab, "Novel implementations of dual- and triple-Band filters on double-sided substrates," in *IEEE Radio and Wireless Symposium*, San Diego, CA, Jan. 2009, pp. 79-82.

[45] F. Huang, "Dual-band superconducting spiral filters including narrow bandstop notches," *IEEE Trans. Microw. Theory Tech.*, vol. 57, no. 5, pp. 1188–1195, May 2009.

[46] M. Memarian and R. R. Mansour, "Dual-band half-cut dielectric resonator filters," in *Proc. 39th Eur. Microw. Conf.*, Rome, Italy, Sep. 2009, pp. 555-558.

[47] M. A. S. Soriano, E. Bronchalo, and G. T. Penalva, "Dual band bandpass filters based on strong coupling directional couplers," in *Proc. 39th Eur. Microw. Conf.*, Rome, Italy, Sep. 2009, pp. 1401-1404.

[48] C. W. Tang, W. T. Liu, M. G. Chen, and Y. C. Lin, "Design of dual-band bandpass filters with short-end coupled lines," in *Proc. 39th Eur. Microw. Conf.*, Rome, Italy, Sep. 2009, pp. 1385-1388.

[49] C. W. Hsue, J. W. Hsu, C. H. Lu, and S. T. Peng, "Design and implementation of microwave multi-band multi-level filters using equal-length transmission lines and Yule–Walker scheme," *IET Microw. Antenna. P.*, vol. 3, no. 5, pp. 826–833, Aug. 2009.

[50] Z. H. Chang, M. Chen, W. Wen, "A novel dual-band bandpass filter based on DBR," in *Proc. Asia-Pacific Microw. Conf.*, Singapore, Dec. 2009, pp. 1383-1386.

[51] H. Wang and Q. X. Chu, "A Compact dual-band filter with adjustable transmission zeros," in *Proc. 39th Eur. Microw. Conf.*, Rome, Italy, Sep. 2009, pp. 117-120.

[52] P. H. Deng and J. H. Jheng, "A switched reconfigurable high-isolation dual-band

bandpass filter," *IEEE Microw. Wireless Compon. Lett.*, vol. 21, no. 2, pp. 71-73, Feb. 2011.

[53] C. H. Kim and K. Chang, "Independently controllable dual-band bandpass filters using asymmetric stepped-impedance resonators," accepted by *IEEE Trans. Microw. Theory Tech.*, Oct. 2011.

[54] G. Chaudhary, H. Choi, Y. Jeong, J. Lim, D. Kim, and J. C. Kim, "Design of dual-band bandpass filter using DGS with controllable second passband," *IEEE Microw. Wireless Compon. Lett.*, vol. 21, no. 11, pp. 589-591, Nov. 2011.

[55] W. H. Tu, "Design of switchable dual-band bandpass filters with four states," *IET Microw. Antenna. P.*, vol. 4, no. 12, pp. 2234–2239, Dec. 2010.

[56] A. I. Abunjaileh and I. C. Hunter, "Combline filter with tunable bandwidth and centre frequency," in *IEEE MTT-S Int. Microw. Symp. Dig.*, Anaheim, California, May 2010, pp. 1476–1479.

[57] E. E. Djpoumessi, M Chaker, and K. Wu, "Tunable dual-band filters based on capacitiveloaded stepped-impedance resonators," *IET Microw. Antenna. P.*, vol. 3, no. 1, pp. 117-124, Feb. 2009.

[58] D. Girbau, A. Kazaro, A. Perez, E. Martinez, L. Pradell, and R. Villarino, "Tunable dual-band filters based on capacitive-loaded stepped-impedance resonators," in *Proc. 39th Eur. Microw. Conf.*, Rome, Italy, Sep. 2009, pp. 113-116.

[59] G. S. Huang and C. H. Chen, "Dual-band balun bandpass filter with hybrid structure," *IEEE Microw. Wireless Compon. Lett.*, vol. 21, no. 7, pp. 356-358, Nov. 2011.

[60] J. H. Chang, Y. S. Lin, C. H. Lee, and C. G. Hsu, "Balanced dual-band BPF design using ring resonators," in *IEEE International Workshop on Electromagnetics, App;ications and Student Innovatopn*, Taipei, Taiwan, Aug. 2011, pp. 94-98.

[61] J. E. Lim, M. H. Nam, H. O. Choi, J. H. Lee, "Two-port balanced dual-band bandpass filter based on stepped impedance resonators," in *Proc. Asia-Pacific Microw. Conf.*, Yokohama, Japan, Dec. 2010, pp. 1114-1117.

[62] J. Shi and Q. Xue, "Novel balanced dual-band bandpass filter using coupled stepped-impedance resonators," *IEEE Microw. Wireless Compon. Lett.*, vol. 20, no. 1, pp. 19-21, Nov. 2010.

[63] J. Shi and Q. Xue, "Dual-band and wide-stopband single-band balanced bandpass filters with high selectivity and common-mode suppression," *IEEE Trans. Microw. Theory Tech.*, vol. 58, no. 8, pp. 2204–2212, Aug. 2010.

[64] C. H. Lee, C. G. Hsu, and C. C. Hsu, "Balanced dual-band BPF with stub-loaded SIRs for common-mode suppression," *IEEE Microw. Wireless Compon. Lett.*, vol. 20, no. 2, pp. 70-72, Nov. 2010.

[65] J. Shi and Q. Xue, "Balanced bandpass filters using center-loaded half-wavelength resonators," *IEEE Trans. Microw. Theory Tech.*, vol. 58, no. 4, pp. 970–977, Apr. 2010.

[66] S. Oshima, K. Wada, R. Murata, and Y. Shimakata, "Multilayer Dual-Band Bandpass Filter in Low-Temperature Co-Fired Ceramic Substrate for Ultra-Wideband Applications," *IEEE Trans. Microw. Theory Tech.*, vol. 58, no. 3, pp. 614–623, Mar. 2010.

[67] R. G. Garcia, M. S. Renedo, B. Jarry, J. Lintignat, and B. Barelaud, "Microwave multi-path dual-passband filters for wide-band applications," in *Proc. 39th Eur. Microw. Conf.*, Rome, Italy, Sep. 2009, pp. 109-112.

[68] Z. C. Hao and J. S. Hong, "Dual-band UWB filter using multilayer liquid crystal polymer technology," *Electron. Lett.*, vol. 46, no. 3, pp. 265-266, Feb. 2010.

[69] D. Yuandan and T. Itoh, "Miniaturized dual-band substrate integrated waveguide filters using complementary split-ring resonators," in *IEEE MTT-S Int. Microw. Symp. Dig.*, Baltimore, June 2011.

[70] V. Sekar and K. Entesari, "A novel compact dual-band half-mode substrate integrated waveguide bandpass filter," in *IEEE MTT-S Int. Microw. Symp. Dig.*, Baltimore, June 2011.

[71] J. Chen, B. Wu, L. W. Jiang, C. H. Liang, "Design of dual-band substrate integrated waveguide filter using frequency transformation method," in *International Conference on Microwave and Millimeter Wave Technology*, Chengdu, China, May 2010, pp. 1286–1289.

[72] B. J. Chen, T. M. Shen, and R. B. Wu, "Dual-band vertically stacked laminated waveguide filter design in LTCC technology," *IEEE Trans. Microw. Theory Tech.*, vol. 57, no. 6, pp. 1554–1562, June 2009.

[73] K. W. Qian and X. H. Tang, "Compact dual-band semi-lumped bandpass filter with LTCC technology," *Electron. Lett.*, vol. 47, no. 13, pp. 755-757, Jun. 2011.

[74] W. Shen, W. Y. Yin, and X. W. Sun, "Miniaturized dual-band substrate integrated waveguide filter with controllable bandwidths," *IEEE Microw. Wireless Compon. Lett.*, vol. 21, no. 8, pp. 418-420, Aug. 2011.

[75] S. K. Hashemi, "Dual-band bandpass filters based on multilayer ring resonators," in *Mediterranean Microwave Symposium*, Yasmine Hammamet, Tunisia, Sep. 2011, pp. 34-37.

[76] V. Turgaliev, D. Kholodnyak, I. Vendik, D. Stopel, S. Humbla, J. Muller, and M. A. Hein, "LTCC highly loaded cavities for the design of single- and dual-band low-loss miniature filters," in *Proc. 40th Eur. Microw. Conf.*, Paris, France, Sep. 2010, pp. 180-183.

[77] Y. C. Chiou, C. Y. Wu, and J. T. Kuo, "New miniaturized dual-mode dual-band ring resonator bandpass filter with microwave C-sections," *IEEE Microw. Wireless Compon. Lett.*, vol. 20, no. 2, pp. 67-69, Feb., 2010. [原本的34]

[78] S. Luo, L. Zhu, and S. Sun, "A dual-band ring-resonator bandpass filter based on two pairs of degenerate modes," *IEEE Trans. Microw. Theory Tech.*, vol. 58, no. 12, pp.

3427–3432, Dec. 2010.

[79] B. Choi, W. Lee, H. Kim, and H. Choi, "A dual-band bandpass filter using a dual-mode ring resonator with two short-circuited stubs," in *Mediterranean Microwave Symposium*, Guzelyurt, Northern Cyprus, Aug. 2010, pp. 152-155.

[80] S. Sun, "A dual-band bandpass filter using a single dual-mode ring resonator," *IEEE Microw. Wireless Compon. Lett.*, vol. 21, no. 6, pp. 298-300, June 2011.

[81] J. T. Kuo and T. W. Lin, "Dual-mode dual-band ring resonator bandpass filter with transmission zeros," in *Proc. Asia-Pacific Microw. Conf.*, Yokohama, Japan, Dec. 2010, pp. 1865-1870.

[82] M. S. Renedo and R. G. Garcia, "Multi-coupled-resonator dual-band bandpass microstrip filters with NRN," in *IEEE MTT-S Int. Microw. Symp. Dig.*, Baltimore, June 2011.

[83] S. C. Lin, "Microstrip dual/quad-band filters with coupled lines and quasi-lumped impedance inverters based on parallel-path transmission," *IEEE Trans. Microw. Theory Tech.*, vol. 59, no. 8, pp. 1937–1946, Aug. 2011.

[84] E. Corrales, O. Menendez, P. de Paco, M. Ramirez, and J. Verdu, "Microstrip dual-band bandpass filter based on the cul-de-sac topology," in *Proc. 40th Eur. Microw. Conf.*, Paris, France, Sep. 2010, pp. 549-552.

[85] M. M. Fahmi, J. A. Ruiz-Cruz, R. R. Mansour, and K. A. Zaki, "Compact wide-band ridge waveguide dual-band filters," in *IEEE MTT-S Int. Microw. Symp. Dig.*, Anaheim, California, May 2010, pp. 888–891.

[86] O. Glubokov and D. Budimir, "Compact E-plane doublet structures for modular filter design," in *Proc. 40th Eur. Microw. Conf.*, Paris, France, Sep. 2010, pp. 1253-1256.

[87] D. C. Rebenaque, M. M. Mendoza, J. P. Garcia, J. S. G. Diaz, and A. A. Melcon, "Novel implementations for microstrip resonator filters in transversal topology," in *Proc. 39th Eur. Microw. Conf.*, Rome, Italy, Sep. 2009, pp. 775-778.

[88] M. S. Renedo and R. G. Garcia, "Microwave dual-band bandpass planar filter using double-coupled resonating feeding sections," in *Proc. 39th Eur. Microw. Conf.*, Rome, Italy, Sep. 2009, pp. 101-104.

[89] M. Zhou, X. Tang, and F. Xiao, "Compact dual band transversal bandpass filter with multiple transmission zeros and controllable bandwidths," *IEEE Microw. Wireless Compon. Lett.*, vol. 19, no. 6, pp. 347-349, June 2009.

[90] R. J. Cameron, "General coupling matrix synthesis methods for Chebyshev filtering functions," *IEEE Trans. Microw. Theory Tech.*, vol. 47, no. 4, pp. 433–442, Apr. 1999.

[91] R. J. Cameron, A. R. Harish, and C. J. Radcliffe, "Synthesis of advanced microwave filters without diagonal cross-couplings," *IEEE Trans. Microw. Theory Tech.*, vol. 50, no. 12, pp. 2862–2872, Dec. 2002.

[92] R. J. Cameron, "Advanced coupling matrix synthesis techniques for microwave

filters," *IEEE Trans. Microw. Theory Tech.*, vol. 51, no. 1, pp. 1–10, Jan. 2003.

[93] R. J. Cameron, C. M.Kudsia, and R. R. Mansour, *Microwave Filters for Communication Systems: Fundamentals, Design, and Applications*. Hoboken, NJ: Wiley, 2007.

[94] P. Kozakowski, A. Lamecki, P. Sypek, and M. Mrozowski, "Eigenvalue approach to synthesis of prototype filters with source/load coupling," *IEEE Microw.Wireless Compon. Lett.*, vol. 15, no. 2, pp. 98–100, Feb. 2005.

[95] S. Amari, "Synthesis of cross-coupled resonator filters using an analytical gradient-based optimization technique," *IEEE Trans. Microw. Theory Tech.*, vol. 48, no. 9, pp. 1559–1564, Sep. 2000.

[96] A. G. Lamperez, "Analytical synthesis algorithm of dual-band filters with asymmetric pass bands and generalized topology," in *IEEE MTT-S Int. Microw. Symp. Dig.*, Honolulu, HI, Jun. 2007, pp. 909–912.

[97] G. Macchiarella and S. Tamiazzo, "Design techniques for dual-passband filters," *IEEE Trans. Microw. Theory Tech.*, vol. 53, no. 11, pp. 3265–3271, Nov. 2005.

[98] R. J. Cameron, M. Yu, and Y.Wang, "Direct-coupled microwave filters with single and dual stopbands," *IEEE Trans. Microw. Theory Tech.*, vol. 53, no. 11, pp. 3288–3297, Nov. 2005.

[99] S. Sun and L. Zhu, "Coupling dispersion of parallel-coupled microstrip lines for dual-band filters with controllable fractional pass bandwidths," in *IEEE MTT-S Int. Microw. Symp. Dig.*, Long Beach, CA, Jun. 2005, pp. 2195–2198.

[100] P. Lenoir, S. Bila, F. Seyfert, D. Baillargeat, and S. Verdeyme, "Synthesis and design of asymmetrical dual-band bandpass filters based on equivalent network simplification," *IEEE Trans. Microw. Theory Tech.*, vol. 54, no. 7, pp. 3090–3097, Jul. 2006.

[101] M. S. Wu, Y. Z. Chueh, J. C. Yeh, and S. G. Mao, "Synthesis of triple-band and quad-band bandpass filters using lumped-element coplanar waveguide resonators," *Prog. Electromagn. Res. B*, vol. 13, pp. 433–451, Jul. 2009.

[102] Y. Zhang, K. A. Zaki, J. A. Ruiz-Cruz, and A. E. Atia, "Analytical synthesis of generalized multi-band microwave filters," in *IEEE MTT-S Int. Microw. Symp. Dig.*, Honolulu, HI, 2007, pp. 1273–1276.

[103] M. Mokhtaari, J. Bornemann, K. Rambabu, and S. Amari, "Coupling matrix design of dual and triple passband filters," *IEEE Trans. Microw. Theory Tech.*, vol. 54, no. 11, pp. 3940–3946, Nov. 2006.

[104] V. Lunot, F. Seyfert, S. Bila, and A. Nasser, "Certified computation of optimal multiband filtering functions," *IEEE Trans. Microw. Theory Tech.*, vol. 56, no. 1, pp. 105–112, Jan. 2008.

[105] G. Macchiarella and S. Tamiazzo, "Dual-band filters for base station multi-band combiners," in *IEEE MTT-S Int. Microw. Symp. Dig.*, Honolulu, HI, 2007, pp.

1289–1292.

[106]   G. Macchiarella, "Accurate synthesis of inline prototype filters using cascaded triplet and quadruplet sections," *IEEE Trans. Microw. Theory Tech.*, vol. 50, no. 7, pp. 1779-1783, July 2002.

[107]   X. W. Dai, C. H. Liang, G. Li, and Z. X. Chen, "Novel dual-mode dual-band bandpass filter using microstrip meander-loop resonators," *J. of Electromagn. Waves and Appl.,* vol. 22, pp. 573-580, 2008.

[108]   X. Y. Zhang, J. Shi, J. X. Chen, and Q. Xue, "Dual-band bandpass filter design using a novel feed scheme," *IEEE Microw. Wireless Compon. Lett.*, vol. 19, no. 6, pp. 350-352, Nov. 2005.

[109]   S. Amari and M. Bekheit "A new class of dual-mode dual-band waveguide filters," *IEEE Trans. Microw. Theory Tech.*, vol. 56, no. 8, pp. 1938-1944, Aug., 2008.

[110]   X. Y. Zhang and Q. Xue, "Novel dual-mode dual-band filters using coplanar-waveguide-fed ring resonators," *IEEE Trans. Microw. Theory Tech.*, vol. 55, no. 10, pp. 2183-2190, Oct., 2007.

[111]   J. X. Chen, T. Y. Yum, J. L. Li, and Q. Xue, "Dual-mode dual-bandbandpass filter using stacked-loop structure," *IEEE Microw. Wireless Compon. Lett.*, vol. 16, no. 9, pp. 502-504, Sep., 2006.

[112]   C. Karpuz and A. Görür, "Dual-mode dual-band microstrip filters," in *Proc. 39th Eur. Microw. Conf.*, Rome, Italy, Sep. 2009, pp. 105-108.

[113]   C. Karpuz, A. Görür, E. Güntürkün, and A. Görür, "Asymmetric response dual-mode dual-band bandstop filters having simple and understandable topology," in *Proc. Asia-Pacific Microw. Conf.*, Singapore, 2009, pp. 925-928.

[114]   K. Kim, H. Pyo, J. An, and Y. Lim, "Dual-band filter using half wavelength resonators and dual-mode resonator," in *Electrical Engineering/Electronics, Computer, Telecommunications and Information Technology International Conference(ECTI-CON 2009)*, Pattaya, Chonburi, 2009, pp. 928-931.

[115]   P. Mondal and M. K. Mandal, "Design of dual-band bandpass filters using stub-loaded open-loop resonators," *IEEE Trans. Microw. Theory Tech.*, vol. 56, no. 1, pp. 150-155, Jan., 2008.

[116]   X. Y. Zhang, J. X. Chen, Q. Xue, and S. M. Li, "Dual-band bandpass filters using stub-loaded resonators," *IEEE Microw. Wireless Compon. Lett.*, vol. 17, no. 8, pp. 583-585, Aug., 2007.

[117]   J. S. Hong and W. Tang, "Dual-band filter based on non-degenerate dualmode slow-wave open-loop resonators," in *IEEE MTT-S Int. Microw. Symp. Dig.*, Boston, MA, 2009, pp. 861-864.

[118]   T. W. Lin, U. H. Lok, and J. T. Kuo, "New dual-mode dual-band bandpass filter with quasi-elliptic function passbands and controllable bandwidths," in *IEEE MTT-S*

Int. Microw. Symp. Dig., Anaheim, CA, 2010, pp. 576-579.

[119]   S. Luo and L. Zhu, "A novel dual-mode dual-band bandpass filter based on a single ring resonator," *IEEE Microw. Wireless Compon. Lett.*, vol. 19, no. 8, pp. 497-499, Aug., 2009.

[120]   M. Avida, A. Balalem, A. Safwat, H. El-Hennawy, and A. Omar, "Combined low-pass and bandpass filter response using microstrip dual-mode resonators," in *IEEE MTT-S Int. Microw. Symp. Dig.*, San Francisco, CA, 2006, pp. 701-704.

[121]   T. H. Huang, H. J. Chen, C. S. Chang, L. S. Chen, Y. H. Wang, and M. P. Houng, "A novel compact ring dual-mode filter with adjustable second-passband for dual-band applications," *IEEE Microw. Wireless Compon. Lett.*, vol. 16, no. 6, pp. 360-362, June, 2006.

[122]   S. Saxena, S. Porwal, K. Soni, P. Chhawchharia, and S. K. Koul, "Analysis and design of bandstop filter using E-shaped dual mode resonator," in *Microwave, Communications, Antennas and Electronics Systems(COMCAS 2009)*, Tel Aviv, 2009, pp. 1-6.

[123]   J. R. Lee, J. H. Cho, and S. W. Yun, "New compact bandpass filter using microstrip $\lambda/4$ resonator with open stub inverter," *IEEE Microw. Guided Wave Lett.*, vol. 12, no. 12, pp. 526-527, Dec., 2000.

[124]   C. K. Liao, P. L. Chi, and C. Y. Chang, "Microstrip realization of generalized Chebyshev filters with box-like coupling schemes," *IEEE Trans. Microw. Theory Tech.*, vol. 55, no. 1, pp. 147-153, Jan., 2007.

[125]   W. He, Z. Ma, C. Chen, T. Anada, and Y. Kobayashi, "A novel dual band bandpass filter using microstrip stub-loaded two-mode resonators with source and load coupling," in *Proc. Asia-Pacific Microw. Conf.*, Macau, 2008, pp. 1-4.

[126]   R. Rezaiesarlak, E. Mehrshahi, and M. Salehi, "A dual behavior-resonator structure for designing multi-band bandpass waveguide filters," in *Proc. Asia-Pacific Microwave Conf.,* Yokohama, Japan, Dec. 2010, pp.1110-1113.

[127]   J. C. Liu, J. W. Wang, B. H. Zeng, and D. C. Chang, "CPW-fed dual-mode double-square-ring resonators for quad-band filters," *IEEE Microw. Wireless Compon. Lett.*, vol. 20, no. 3, pp. 142–144, Mar. 2010.

[128]   X. Y. Zhang, Q. Xue, and B. J. Hu, "Planar tri-band bandpass filter with compact size," *IEEE Microw. Wireless Compon. Lett.*, vol. 20, no. 5, pp. 262–264, May 2010.

[129]   H. W. Wu and R. Y. Yang, "A new quad-band bandpass filter using asymmetric stepped impedance resonators," *IEEE Microw. Wireless Compon. Lett.*, vol. 21, no. 4, pp. 203–205, Apr. 2011.

[130]   J. Y. Wu and W. H. Tu, "Design of quad-band bandpass filter with multiple transmission zeros," *Electron. Lett.*, vol. 47, no. 8, pp. 502–503, Apr. 2011.

[131]   R. Gómez-García, J. Muñoz-Ferreras, and M. Sánchez-Renedo, "Microwave transversal six-band bandpass planar filter for multi-standard wireless applications,"

in *Radio and Wireless Symposium*, pp. 166–169, Apr. 2011.

[132]   C. L. Hsu and J. T. Kuo, "Design of microstrip dual-band filters using a double-diplexing configuration," in *Proc. Asia-Pacific Microwave Conf.*, Yokohama, Japan, Dec. 2006, pp. 1241-1244.

[133]   *"Advanced Design System (ADS),"* Agilent Technol., Santa Rosa, CA, 2003, ver. 2003C.

[134]   *"EM User's Manual,"* Sonnet Softw. Inc., Liverpool, NY, 2004.

[135]   A. Garia-Lamperez, S. Llorente-Romano, M. Salazar-Palma, M. J. Padilla-Cruz, and I. H. Carpintero, "Synthesis of cross-coupled lossy resonator filters with multiple input/output couplings by gradient optimization," in *IEEE AP-S Int. Symp.*, vol. 2, Jun. 2003, pp. 52–55.

[136]   S. Amari and J. Bornemann, "Maximum number of finite transmission zeros of coupled resonator filters with source/load-multiresonator coupling and a given topology," in *Proc. Asia-Pacific Microwave Conf.*, Sydney, Australia, Dec. 2000, pp. 1175-1177.

[137]   G. L. Matthaei, L. Young, and E. M. T. Jones, *Microwave Filters, Impedance-Matching Networks, and Coupling Structures*. Norwood, MA: Artech House, 1980.

[138]   M. Makimoto and S. Yamashita, "Bandpass filters using parallel coupled stripline stepped impedance resonators," *IEEE Trans. Microw. Theory Tech.*, vol. MTT-28, no. 12, pp. 1413-1417, Dec., 1980.

[139]   J. C. Lu, C. K. Liao, and C. Y. Chang, "Microstrip parallel-coupled filters with cascade trisection and quadruplet responses," *IEEE Trans. Microw. Theory Tech.*, vol. 56, no. 9, pp. 2101–2110, Sep. 2008.

[140]   M. Matsuo, H. Yabuki, and M. Makimoto, "The design of a half-wavelength resonator BPF with attenuation poles at desired frequencies," in *IEEE MTT-S Int. Microwave Symp. Dig.*, Boston, MA, June 2000, pp. 1181-1184.

[141]   G. I. Zysman and A. K. Johnson, "Coupled transmission line networks in an inhomogeneous dielectric medium," *IEEE Trans. Microw. Theory Tech.*, vol. MTT-17, no. 10, pp. 753-759, Oct. 1969.

[142]   G. D. Alley, "Interdigital capacitors and their application to lumped element microwave integrated circuits," *IEEE Trans. Microw. Theory Tech.*, vol. MTT-18, no. 12, pp. 1028-1033, Dec., 1970.

[143]   C. K. Liao, C. Y. Chang, and J. Lin, "A vector-fitting formulation for parameter extraction of lossy microwave filters," *IEEE Microw. Wireless Compon. Lett.*, vol. 17, no. 4, pp. 277–279, Apr. 2007.

簡歷

姓　　名　：郭益廷

性　　別　：男

出生年月日 ： 民國 70 年 3 月 13 日

籍　　貫　： 台灣省台南市

學　　歷　： 成功大學電機工程學系學士班畢業

經　　歷　： 高中畢業於高雄中學，大學畢業於成功大學電機工程
　　　　　　學系。入學考進入交通大學電信所電波組研讀，經系
　　　　　　上認可於碩一學期結束後逕讀電信所博士班。個人在
　　　　　　博士班期間研究主題為微波被動元件之設計與製作。

論文題目　：

多頻濾波器耦合矩陣之合成及其
實現於微帶線平行耦合濾波器結構之研究

Synthesis of Multi-band Coupling Matrix and Its Implementation of
Microstrip Parallel Coupled Filter Structures

Publication List

I. Journals

[1] **Y. T. Kuo**, J. C. Lu, C. K. Liao, and C. Y. Chang, "New multiband coupling matrix synthesis technique and its microstrip implementation," in *IEEE Trans. Microw. Theory Tech.*, vol. 58, no. 7, pp. 1840-1850, July, 2010.

[2] **Y. T. Kuo** and C. Y. Chang, "Analytical design of two-mode dual-band filters using E-shaped resonators," accepted by *IEEE Trans. Microw. Theory Tech.*

II. Conferences

[1] **Y. T. Kuo**, J. C. Lu, C. K. Liao, and C. Y. Chang, "Dual-band filters with frequency-separated dual-path coupling scheme," in *Proc. 40th Eur. Microwave Conf.*, 2010, pp. 553-556.

[2] **Y. T. Kuo**, J. Y. Li, S. Y. Cheng, and C. Y. Chang, "Tri-band and quad-band filter design using E-shaped resonators," accepted to be presented at the *Asia-Pacific Microwave Conf.*, Melbourne, Australian, Dec. 2011.